

# Electrical doping of charge carrier injection and extraction layers for solution processed organic optoelectronic devices

Zur Erlangung des akademischen Grades eines  
DOKTORS DER NATURWISSENSCHAFTEN  
(Dr. rer. nat.)

von der KIT-Fakultät für Chemie und Biowissenschaften  
des Karlsruher Instituts für Technologie (KIT)

genehmigte  
DISSERTATION

von

**Tanja Schneider**

aus Pirmasens, Deutschland

KIT-Dekan:	Prof. Willem M. Klopper
Referent:	Prof. Christopher Barner-Kowollik
Koreferent:	Prof. Uli Lemmer
Tag der Mündlichen Prüfung:	22.07.2016





Die vorliegende Arbeit wurde von August 2013 bis Juli 2016 unter Anleitung von Prof. Dr. Christopher Barner-Kowollik am Karlsruher Institut für Technologie (KIT) angefertigt.



It's the end of the world as we know it  
and I feel fine.  
REM



# Abstract

In organic optoelectronic devices electrically doped charge transport layers are often used to optimize the charge carrier injection (in organic light emitting diodes, OLEDs) or extraction (in organic solar cells, OSC). The resulting ohmic contacts due to the doping generate a better band alignment between active layer and electrodes and thus minimize voltage losses. Doped transport layers are generally used in common vacuum processed devices. To use cheaper printing processes, like roll-to-roll printing, for large area devices doping from solution is crucial. Furthermore, common organic optoelectronic devices are multilayer devices. Thus another important issue to allow large scale production from solution is the deposition of a layer without dissolving and damaging the layer underneath. One option is to use materials, which can be crosslinked after deposition and thus become insoluble. Therefore, in this work different charge transport materials are p- and n-doped by different doping reactions, processed from solution. The doping and its efficiency is characterized by different methods. Additionally crosslinkable polymers are p-doped and compared with their corresponding non-crosslinkable polymeric and low-molecular counterpart.

This thesis is divided in two parts, the solution processing of p-doped and n-doped layers. For the p-doping, low-molecular weight molecules are compared to their corresponding crosslinkable and non-crosslinkable side-chain polymers, processed from solution. The doping itself, the influence of the polymerization, the crosslinking group and the crosslinking conditions is investigated by different methods. By photo electron yield spectroscopy in air (PESA) the depletion of the electron-density on the hole transport molecules and the resulting shift of the ionization potential is verified. The charge transport between the hole transporting matrix and the dopant is visible in additional absorption bands in UV-vis-NIR spectra and is quantified by electron paramagnetic spin resonance spectroscopy (EPR). By the latter it is verified that in the analyzed systems the doping mechanism is an integer charge transfer and no formation of hybrid orbitals is found. An increased conductivity and for one analyzed system also an increased mobility is studied by two different methods: Space-charge limited current (SCLC) measured in monopolar devices and charge extraction by linear increasing voltage (CELIV). The results of both measurements are in good agreement to each other and show increased conductivity and mobility upon increasing doping concentrations. The undoped and doped layers are implemented

in OLEDs and the formation of ohmic contacts is verified. Neither the polymerization nor the usage of the crosslinking group has any negative effects on the doping processed from solution. But the crosslinking temperature is too high to keep a stable doping. Therefore, in the last part of the chapter the temperature stability of the doping in the used matrix:dopant combinations is analyzed. However, the undoped crosslinked layers are stable even after annealing if implemented in OLEDs show a similar performance compared to non-annealed layers.

The second part addresses the solution processing of n-doped charge transport layers. n-Doping is much more complex due to the high reactivity and sensitivity against oxidation of the used dopants. In this thesis a process is introduced to dope an organic semiconductor with metallic sodium in a common organic solvent. The charge transfer between the dopant and the electron transporting material is measured in solution by UV-vis-spectroscopy and quantified in thin films by EPR. When implemented in organic solar cells the doped layers show an improved performance due to the formation of ohmic contacts. This leads to comparable efficiency as in the commonly used reference zinc oxide (ZnO).

As another option, n-doping of different fullerenes with the cationic dye rhodamine B is analyzed processed from solution. Due to the necessity of the transformation of cationic dyes in their leuco-form by thermal activation or activation with light, thus they can act as dopants, the charge transfer between fullerenes and dopant is investigated under white-light illumination. The doping efficiencies are quantified by EPR as before. When implemented in organic solar cells as electron extraction layers (EEL) enhanced efficiencies upon using doped layers are observed similar to the efficiencies of the reference OSCs using commonly used ZnO as EEL.

All procedures presented in this thesis represent an important step on the way to completely process organic optoelectronic devices from solution.

# Zusammenfassung der Doktorarbeit

In organischen optoelektronischen Bauteilen werden elektrisch dotierte Ladungstransportschichten oft zur Optimierung der Ladungsträgerinjektion (in organischen Leuchtdioden, OLEDs) bzw. -extraktion (in organischen Solarzellen, OSC) genutzt. Die durch die Dotierung erzeugten Ohmschen Kontakte verbessern die Bandanpassung zwischen der aktiven Schicht der Bauteile und den Elektroden, was Spannungsverluste minimiert. In vakuumprozessierten Bauteilen werden dotierte Transportschichten bereits standardmäßig verwendet. Um günstigere Druckverfahren, wie Rolle-zu-Rolle-Verfahren, verwenden und auch großflächige Anwendungen einfach und günstig umsetzen zu können, ist es wichtig den Dotierprozess auch in Lösung nutzen zu können. Desweiteren sind organische optoelektronische Bauteile üblicherweise Mehrschichtsysteme. Daher besteht eine weitere Herausforderung der großflächigen Prozessierung aus der Flüssigphase darin, Schichten abzuscheiden ohne darunterliegende Schichten wieder anzulösen und somit zu beschädigen. Eine Möglichkeit ist die Verwendung von Materialien, die nach Abscheidung als Schicht vernetzt werden können und somit unlöslich werden. Daher wurden in dieser Arbeit verschiedene Ladungstransportschichten mittels verschiedener Dotierreaktionen in der Flüssigphase p- und n-dotiert. Die Dotierung und ihre Effizienz wurde mit verschiedenen Analysemethoden charakterisiert. Zusätzlich wurden auch vernetzbare Polymere p-dotiert und mit ihren entsprechenden unnetzbaren polymeren und niedermolekularen Gegenstücken verglichen.

Die vorliegende Arbeit ist in zwei Teile unterteilt, wobei sich ersterer mit der Flüssigprozessierung p-dotierter und zweiterer mit der Flüssigprozessierung n-dotierter Schichten befasst. Im ersten Teil wird die flüssigprozessierte p-Dotierung von niedermolekularen Materialien mit der ihrer entsprechenden vernetzbaren und nicht-vernetzbaaren Seitenkettenpolymere verglichen. Die Dotierung, der Einfluss der Polymerisation, der Vernetzerguppe und der Vernetzungsbedingungen wird mit verschiedenen Methoden untersucht. Mittels Photoelektronenausbeutespektroskopie an Luft (engl. photoelectron yield spectroscopy in air, PESA) wird die Verarmung der Elektronendichte der Lochleiter und die dadurch resultierende Verschiebung der Ionisationsenergie nachgewiesen. Der Ladungstransfer zwischen Lochleiter und Dotand ist im UV-Vis-NIR-Spektrum anhand zusätzlicher Absorptionsbanden zu sehen und wird mit Hilfe von Elektronenspinresonanzspektroskopie (EPR) quantifiziert. Mit letzterem wird verifiziert, dass der Dotier-

mechanismus der untersuchten systeme über einen Ladungstransfer und nicht über die Bildung von Hybridorbitalen verläuft. Eine erhöhte Leitfähigkeit und teilweise auch eine erhöhte Mobilität wird zum Vergleich mit zwei unterschiedlichen Messmethoden untersucht: Raumladungsbegrenzte Ströme in monopolen Bauteilen (engl. space charge limited current, SCLC) und Ladungsträgerextraktion durch linear ansteigende Spannung (engl. charge extraction by linear increasing voltage, CELIV). Die Ergebnisse beider Messungen stimmen sehr gut überein und weisen erhöhte Leitfähigkeiten und Mobilitäten bei erhöhten Dotierkonzentrationen auf. Daraufhin wurden die dotierten Schichten in OLEDs eingebaut und die Entstehung von Ohmschen Kontakten nachgewiesen. Die Polymerisation und die Verwendung der Vernetzerguppe hat keinen sichtbaren negativen Einfluss auf die Dotierung aus der Flüssigphase. Die Vernetzungstemperatur ist allerdings so hoch, dass die Stabilität der Dotierung nicht mehr gegeben ist. Daher wird im letzten Teil des Kapitels die Temperaturabhängigkeit der Dotierung untersucht. Die undotierten vernetzten Schichten sind allerdings sehr stabil und zeigen in OLEDs ähnliche Leistungen wie die unvernetzte Schichten.

Der zweite Teil der Arbeit befasst sich mit der Flüssigprozessierung n-dotierter Ladungstransportschichten. Diese ist deutlich komplexer als die p-Dotierung, da die verwendeten Dotanden meist sehr reaktiv und oxidationsempfindlich sind. In dieser Arbeit wird ein Verfahren vorgestellt, dass die Flüssigprozessierung eines organischen Halbleiters mit metallischem Natrium in einem gebräuchlichen organischen Lösungsmittel ermöglicht. Der Ladungstransfer zwischen Dotand und Elektronenleiter wird mittels UV-Vis-Spektroskopie in Lösung gemessen und mit Hilfe der EPR Spektroskopie am Film quantifiziert. Beim Einbau in organische Solarzellen ergibt sich eine erhöhte Leistung der dotierten Schichten durch Bildung Ohmscher Kontakte, was in vergleichbaren Effizienzen wie bei Verwendung des Referenzmaterials Zinkoxid resultiert.

Als weitere Möglichkeit wird die n-Dotierung von verschiedenen Fullerenen mit dem kationischen Farbstoff Rhodamin B aus der Flüssigphase untersucht. Da kationische Farbstoffe erst durch thermischer Aktivierung oder Aktivierung durch Licht in ihre Leucoform umgewandelt werden müssen um als Dotanden dienen zu können, wurde der Ladungstransfer zwischen Dotand und Fulleren unter Beleuchtung mit Weißlicht untersucht. Mittels EPR konnten dadurch die Dotiereffizienzen ermittelt werden. Beim Einbau als Elektronenextraktionschichten (engl. electron extraction layers, EEL) in organischen Solarzellen zeigte sich eine deutlich erhöhte Effizienz bei Verwendung dotierter Schichten ähnlich zur Effizienz der Referenzsolarzellen mit üblicherweise verwendetem ZnO als EEL.

Alle in dieser Arbeit vorgestellten Verfahren stellen einen wichtigen Schritt zur Herstellung vollkommen flüssigprozessierter organischer optoelektronischer Bauteile dar.



# Contents

<b>Abstract</b>	<b>i</b>
<b>Zusammenfassung</b>	<b>iii</b>
<b>1. Introduction</b>	<b>1</b>
<b>2. State of the art and Motivation</b>	<b>5</b>
<b>3. Organic semiconductors</b>	<b>9</b>
3.1. Charge carrier transport . . . . .	10
3.2. Low-molecular weight materials versus polymers . . . . .	12
3.3. Organic solar cells . . . . .	17
3.4. Organic light emitting diodes . . . . .	21
3.5. Electrical doping of organic semiconductors . . . . .	23
<b>4. Optoelectronic material and device characterization</b>	<b>29</b>
4.1. Sample preparation . . . . .	29
4.2. Characterization methods . . . . .	29
<b>5. p-Doping by employing strong organic acceptors, processed from solution</b>	<b>39</b>
5.1. Selection of hole transport materials and suitable dopants . . . . .	39
5.2. Comparison of p-doping of polymers and low-molecular weight molecules .	46
5.3. Crosslinkable polymer matrices . . . . .	68
5.4. Temperature stability of p-doping . . . . .	77
5.5. Sample preparation . . . . .	81
<b>6. n-Doped thin-films, processed from solution</b>	<b>85</b>
6.1. Selection of electron transport materials and suitable dopants . . . . .	86
6.2. n-Doping by employing alkali metals . . . . .	87
6.3. n-Doping by employing cationic dyes . . . . .	97
<b>7. Concluding remarks and outlook</b>	<b>105</b>
<b>Bibliography</b>	<b>109</b>
<b>A. Appendix</b>	<b>117</b>
A.1. IUPAC-notation and chemical structure of used optoelectronic materials .	117
A.2. Materials, suppliers and purities . . . . .	120
A.3. Solvent resistance of undoped and doped fullerene layers against Ethanol	121
A.4. Measurements of the organic solar cells directly after fabrication . . . . .	122

<b>Abbreviations</b>	<b>125</b>
<b>List of Figures</b>	<b>129</b>
<b>List of Tables</b>	<b>132</b>
<b>List of Publications and Conference Contributions</b>	<b>135</b>
<b>Acknowledgements</b>	<b>137</b>
<b>Declaration</b>	<b>139</b>

# 1 | Introduction

The awareness of the public to global warming has been increasing recently. Nationally, the German Federal Governments has taken mitigation actions to reduce its share of CO<sub>2</sub> production. One of the actions is to promote the use of the CO<sub>2</sub>-free energies. Another option is to decrease the energy consumption by increasing the efficiency of devices.

In the first case, with regard to the nuclear phase-out, renewable energies have reached public focus. Their share of the gross energy consumption in Germany in 2015 increased from 5% to 32.6%.<sup>[1]</sup> Renewable energies cover a wide range of different types, such as biomass, geothermics, wind, water and solar power. The latter is a promising approach, because the solar energy that reaches the earth every minute, is more than enough to cover the whole energy consumption of the human kind of one year.<sup>[2]</sup>

The actual solar cell technologies can be classified in three generations. The first generation are solar cells made of mono- or polycrystalline silicon wafers. They exhibit efficiencies of 21.3% (polycrystalline) and 25.6% (monocrystalline),<sup>[3]</sup> however, there has not been any significant advancement in the last 20 years.<sup>[4]</sup> Another disadvantage is their expensive manufacturing process due to the high temperatures required to acquire high purity silicon.

Second generation photovoltaics is composed by different thin-film technologies such as copper indium gallium selenide (CIGS), CdTe or amorphous silicon. Due to the thin film characteristic, the production of these type of cells requires less material. CdTe and CIGS exhibit also high efficiencies of 18.7 - 21%.<sup>[3]</sup> However, they have the disadvantage of the usage of harmful substances (cadmium) or scarce elements (indium and tellurium). A better alternative are amorphous silicon solar cells, but their efficiencies are much lower at around 10%.<sup>[3]</sup>

The third generation are so called emerging photovoltaics. These include new concepts, such as tandem- or concentrator-cells, that are potentially able to reach a higher efficiency than the Shockley-Queisser-limit for single band gap solar cells, which is 31%. And also new solar cell technologies such as dye-sensitized solar cells, quantum dot solar cells, perovskite solar cells and organic solar cells belong to this generation.<sup>[5]</sup>

The advantages of organic solar cells (OSCs) are among others that they can be semi-transparent, which makes them suitable for architectonic integration in windows. Due to their low processing temperature they can be deposited on flexible substrates, e.g., for implementation in textiles. With a total thickness of some hundred nanometers, OSC are light-weight and offer the possibility of low cost manufacturing by the use of roll-to-roll processes. Due to the broad variety of photoactive materials tailor-made solar cells can be designed for different applications.[6] A challenge here is their water and oxygen sensitivity and, therefore, short lifetime of the devices.

In case of more efficient devices to reduce CO<sub>2</sub> emission, light emitting diodes (LEDs) reach a broad interest in the field of lighting. Compared to other light sources, LEDs exhibit longer lifetimes, lower energy consumption, faster switching times and a smaller size. The first LED made from GaAsP that emitted visible light, was invented by Holonyak et al. in 1961.[7] In the following years, more efficient LEDs with different colors were developed and with beginning of the mass production they also became affordable. With realization of the first high-brightness blue LED by Nakamura, Akasaki and Amano et al., the generation of efficient white light is possible. In 2014 they were awarded with the Noble prize for their discovery.[8] Nowadays LEDs are commercially available in a broad color spectrum and bright enough to be used in common lighting.

For the use in displays, the organic counterparts, organic light emitting diodes (OLEDs), are an interesting alternative to commonly used liquid-crystal displays (LCDs). The most interesting fact about OLEDs for display technologies is that they are self-emitting. Thus no backlight is needed as in liquid-crystal displays (LCDs). Therefore, every pixel can be switched on or off independent of all other pixels. This results in a higher contrast, faster response times, a better color rendering independent of the viewing angle and a better energy efficiency compared to common LCDs. OLEDs also benefit from a wide range of different emitting molecules, which allow to built devices in a broad color range. This is interesting for lighting as well. Especially their properties as panel radiators and the possibility to built them semitransparent makes them suitable for window integration. They are constructed very similar to organic solar cells and meet similar opportunities and challenges. In contrast to OSCs, OLEDs are already used in commercial available applications such as displays in mobile phones. In 2013 Samsung released one of the first smartphones using a curved OLED display.[9] Also LG plans to develop a flexible Ultra HD panel until 2017.[10]

Due to the architecture of OLEDs and OSCs, which are constructed in different thin layers, that are applied on top of each other, they are processed mainly by vacuum techniques at the moment. These evaporation steps are usually processed in vacuum chambers, which limits the size of the devices. Another problem are the used shadow

masks to structure the different deposited layers. For displays the pixels become smaller, while the area of the display becomes larger. Therefore, the masks have to be very thin, but very stable thus it has to be placed as near as possible to the substrate to prevent shading effects. It is also important to guarantee a uniform deposition rate.

Other deposition techniques are printing processes. Due to their good solubility in common solvents most organic molecules can be processed by inexpensive printing on large areas. Especially, when depositing on flexible substrates, low-cost roll-to-roll printing can be used.[11] A challenge here is to ensure that the solvent to deposit the next layer does not dissolve the layers underneath. To prevent that, e.g. crosslinkable materials are used.

The architecture of OSCs and OLEDs is very similar. Both contain an active layer, either an absorber (OSC) or an emitter (OLED), embedded between two electrodes. To prevent voltage losses, an ohmic contact between the electrodes and the active layer is necessary. Therefore, in vacuum processed devices typically doped charge transport layers are used to enhance the efficiency of the devices.[12] This thesis links the doping of organic semiconductors, which is mainly known from vacuum processed devices, to the commonly used undoped crosslinkable materials to solution processed doping of charge transport layers for organic electronic devices.



## 2 | State of the art and Motivation

Organic optoelectronic devices such as organic solar cells or OLEDs typically exhibit an active layer sandwiched between two electrodes. In this multilayer thin film architecture, layer interfaces often have huge impact on the device properties. If the energy level of the electrodes do not fit the energy levels of the active layer, voltage losses occur due to barriers that hamper the charge carrier extraction (OSC) or injection (OLED). To prevent such voltage losses different strategies can be followed. Interface dipoles such as alkali metal salts (e.g. LiF, NaCl)[13–15], polyelectrolytes (e.g. PFN, PEI, PEIE).[16–21] or n-doped organic semiconductors are used to establish ohmic contacts to the cathode. To enhance the contact to the second electrode, metal oxides with high work functions[22, 23] or p-doped organic semiconductors are used. This thesis focuses on the electrical p- and n-doping of organic interlayers between the active layer and both electrodes implemented in common devices.

To date, electrical doping has been extensively studied in vacuum processed devices.[24, 25] Upon p-doping strong acceptor molecules such as 2,3,5,6-tetrafluoro-7,7,8,8-tetracyanoquinodimethane ( $F_4$ TCNQ) or 1,4,5,8,9,12-hexaazatriphenylene ( $HATCN_6$ ) are employed to accept electrons from the highest occupied molecular orbital (HOMO) of the matrix molecules and thus create an excess of holes on the matrix.[26] Well investigated material systems for efficient hole injection in OLEDs are  $F_4$ TCNQ doped 4,4',4''-tris[phenyl(*m*-tolyl)amino]triphenylamine (MTDATA)[27, 28] or *N,N'*-bis(3-methylphenyl)-*N,N'*-diphenylbenzidine (TPD).[29, 30] The co-evaporated system TPD doped with  $HATCN_6$  was also successfully used as hole extraction layer in organic solar cells.[31]

For n-doping, electrons are transferred from a dopant into the lowest unoccupied molecular orbital (LUMO) of the matrix where they create an electron excess. Suitable n-dopants are cationic dyes,[32–34] which are activated thermally or by illumination. Alternative n-dopants are organometallic complexes[35] or alkali metals with low work functions.[36–38] By doping organic semiconductors with alkali metals, Kido et al. proved the formation of radicals due to doping for co-evaporated aluminiumtris(8-hydroxychinolin) ( $Alq_3$ ) and Lithium.[37] Moses et al. exposed polyacetylene (PA) films to alkali vapor and found an increased conductivity.[39] The major drawback of alkali metals with low atomic numbers, such as lithium, is their high reactivity and their tendency to diffuse within the device. This may lead to quenching of excited states in the active layers of OSCs and OLEDs.[40] This can be avoided by larger dopants like Cs or cationic dyes.[38]

In the latter case leuco crystal violet (LCV),[41] acridine orange base (AOB),[33] pyronine B (PyB),[34] and rhodamine B (RhB)[42] are well investigated dopants for electron extraction layers in organic solar cells. Upon activation by light or thermal energy, the dye is transferred into its leuco form, which can then act as an electron donor.[41] For doping of  $C_{60}$  with LCV the doping mechanism has been analyzed in detail. Here an electron is transferred from the HOMO of LCV to the LUMO of  $C_{60}$ , creating a radical cation on the dye ( $LCV + C_{60} \rightarrow LCV^{\cdot+} + C_{60}^{\cdot-}$ ). This is then stabilized by a transfer of a hydrogen radical to another fullerene and by oxidation from the leuco form to crystal violet (CV) ( $2LCV + 3C_{60} \rightarrow 2CV^+ + 2C_{60}^{\cdot-} + C_{60}H_2$ ).[41] A similar reaction was observed for the doping of  $C_{60}$  with AOB.[33]

With future low-cost large-area printing processes such as roll-to-roll printing of organic electronic devices on flexible substrates in mind, a strong need for solution processable materials exists.[43] A commonly used solution processed hole injection or extraction material is p-doped poly(3,4-ethylenedioxythiophene):polystyrene sulfonate (PEDOT:PSS). Due to its very acidic and also hygroscopic nature, it may reduce the lifetime of devices, e.g., by etching the commonly used indium doped tin oxide (ITO) electrode underneath and thus creating ions that can diffuse in the device.[44] Many organic semiconductors that are established in vacuum processes, can also be deposited from solution. In earlier reports, TPD was doped with camphorsulfonic acid, processed from solution,[45] but this does not solve the problem of acidity. Another solution processable dopant used in literature is a  $F_4$ TCNQ derivative 2-(3-(adamantan-1-yl)propyl)-3,5,6-trifluorotetracyanoquinodimethane ( $F_3$ TCNQ-Adl). These promising results were reported for doping MTDATA and TPD in solution,[46, 47] but its synthesis is challenging including ten steps with an overall yield below 1%.[48] The synthesis of the commercial available dopants HATCN<sub>6</sub> and  $F_4$ TCNQ consists of only one or two steps and therefore much better overall yields of about 80% or 60%.[49, 50]

A commonly used electron extraction/injection layer in organic optoelectronic devices is ZnO[51]. Due to its oxidic character, it is brittle causing problems if processed on flexible substrates. Organic semiconductors do not face such problems, but the solution processing of n-doped organic semiconductors is much more challenging than for p-doping. Alkali metals are not soluble in common solvents. They are only soluble in ammonia at  $-78^\circ\text{C}$ , which are non-suitable process conditions for industrial applications. n-Doping with 1,3-dimethyl-2-phenyl-2,3-dihydro-1*H*-benzimidazole can be processed from solution, but here doping has to be activated by annealing at  $80^\circ\text{C}$  overnight.[52] Li et al. investigated solution processed n-doping of fullerenes with fulleropyrrolidinium ions.[53]

Usually, low-molecular weight materials are used in common vacuum processed organic devices. If those materials are processed from solution, their major drawback is their



tendency of aggregate formation and crystallization, which can affect the optoelectronic properties and the morphology, and may form bad contacts to the ITO electrode.[54] Crystallization can easily be prohibited if amorphous polymeric materials are used. Even if low molecular weight materials can be obtained in higher purity than polymers, the latter usually exhibit higher viscosities, which is often beneficial for printing processes.[54, 55] Here, two different types exist: backbone polymers with a conjugated backbone or side-chain polymers with a non-conjugated backbone and conjugated functional groups. Both have already been successfully used in organic light emitting devices as solution processed hole transport layers without any doping.[54, 56, 57] The extended conjugated backbone may change the optoelectronic properties compared to the low-molecular weight materials.[58, 59] In contrast, the optoelectronic properties of side-chain polymers with pending conjugated functional groups are typically close to the respective molecular counterparts, while exhibiting all advantages of the polymers as well.[54, 55]

One challenge in solution processing is the prevention of the dissolving all previously deposited layers if the next one is applied. One way is to use orthogonal solvents, meaning the deposition of a solution on top of a layer that is insoluble in this solvent.[60, 61] Therefore, materials, which are soluble in water or alcohol are needed, but many organic materials are soluble in similar solvents. An alternative is to make an applied layer insoluble after deposition.[62–64] *In-situ* polymerization of solution processed monomers[65–67] or crosslinking of polymers[68, 69] are well investigated for application in organic devices. When polymerizing monomers the density increases.[70] This can be a huge problem especially in thin-films due to the formation of cracks, which may lead to short circuits. The second possibility, the crosslinking of polymers, can be realized by photocrosslinking or thermal crosslinking. The first may be a problem in optoelectronic devices, because the necessary wavelengths often are in the UV-region[67] which may reduce the lifetime of the device, or, in an area where the active layer absorbs, which may hamper the crosslinking. In case of thermal crosslinking, often very high temperatures far above 200°C are necessary,[68] which may destroy the device.

To evaluate the suitability of a set of matrix materials as well as p- and n-dopants in solution processing applications, in this work, two different matrices were successfully p-doped with two commercial available dopants, processed from solution. The doping and the doping efficiencies are characterized by different methods. At first side-chain polymers were compared to low-molecular weight matrices to investigate the influence of the polymerization on the doping. Afterwards, the doping of the corresponding thermally crosslinkable side-chain polymers was investigated before and after crosslinking to gain insight into the influence of the additional crosslinkable group and the crosslinking conditions. The crosslinkable polymers were designed to allow crosslinking temperatures below

200°C. The applicability was exemplified by implementing the doped layers in organic light emitting diodes.

Furthermore two different n-doping reactions, the doping with alkali metals and the doping with cationic dyes, were successfully performed on different matrices, processed from solution for the first time. The doping was characterized by different measurement methods. Implemented in organic solar cells, the doped films showed superior performance compared to non-doped ones similar to the performance of cells, where commonly used ZnO is employed. The relevant fundamental principles will be explained in the following chapter.

### 3 | Organic semiconductors

In 1954, the first reported conductive organic materials were perylen-halogen-complexes.[71] In the year 1974, Shirakawa synthesized the first conductive polymer *trans*-polyacetylen,[72] which earned him, together with MacDiarmid and Heeger, the Nobel prize in 2000. They were able to increase its conductivity by doping the polymer with halogens especially iodine and achieving metallic conductivity.[73] Some of the first conductive polymers are shown in figure 3.1. After the discovery of conductivity in organic molecules, a world-wide search for other conductive organic materials started and in the 1980th with the development of the first organic solar cells[74] and OLEDs[75] the research field of plastic electronics gained attention.

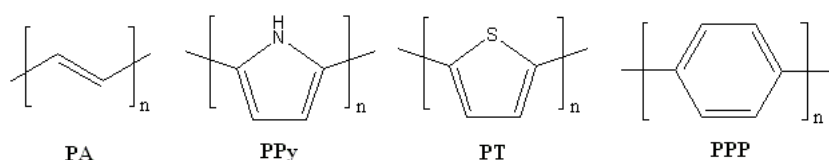


**Figure 3.1.** Some examples of the first conductive polymers: *trans*-polyacetylen (PA), polypyridine (PPy), polythiophene (PT), poly-*para*-phenylene (PPP).

By definition "organic" implies hydrocarbons,[76] but usually they contain also other elements such as, e.g., oxygen, nitrogen, sulfur and/or halogens. The most important characteristic of organic semiconductors is a large conjugated  $\pi$ -system, where the  $p_z$ -orbitals which are orthogonal to the molecular bond ( $\sigma$ -bond), overlap and form one large  $\pi$ -orbital. Thus the electrons of these orbitals are delocalized over the whole molecule (see figure 3.2).[77]

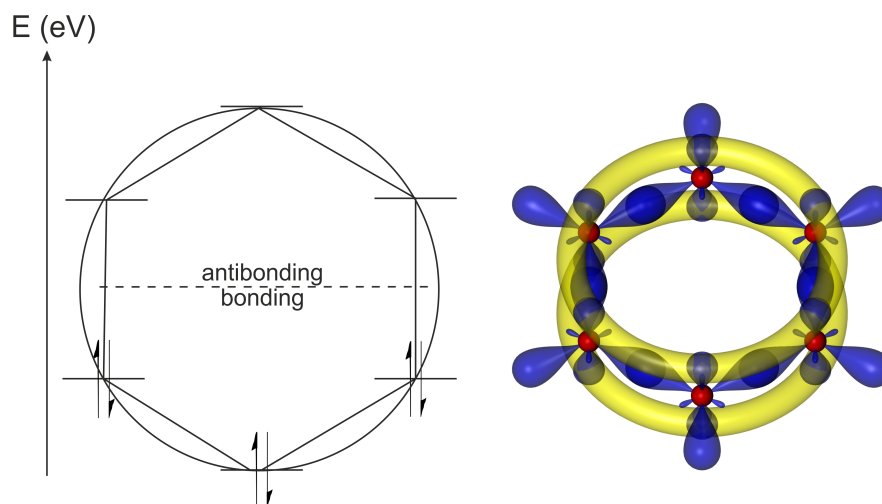


**Figure 3.2.** Frost-Musulin-diagram to estimate relative energies of the orbitals and overlapping  $p_z$ -orbitals in benzol.

To ensure efficient overlapping of the  $p_z$ -orbitals, the molecules should be flat and exhibit alternating double bonds. For conjugated chains, it is also important that the double bonds are *trans*-standing because, in *cis*-double bonds, the orbitals turn out of plane and cannot overlap efficiently anymore. Therefore, Hückel-aromatics are used very often, because, in ring-systems, the conformation is fixed and so less defects accrue than e.g. in polyacetylen. Hückel showed that ring-systems with  $4n+2$   $\pi$ -electrons are energetically favored to build a flat, conjugated  $\pi$ -system.[76, 77] To estimate the relative energies of the orbitals, a Frost-Musulin-diagram can be used as depicted in figure 3.2. A circle with radius  $2\beta$  is drawn with the center at zero energy.  $\beta$  is the exchange integral and describes the coulomb interaction of the electrons. Then the molecular  $n$ -cycle is drawn into this circle with one edge pointing to the lowest point. From the points of contact of the  $n$ -cycle with the circle the energies can be calculated.[78]

### 3.1. Charge carrier transport

Organic semiconductors are characterized by the electronic band gap ( $E_g$ ) between HOMO and LUMO, usually between 1.5 and 3 eV, resulting in semiconducting properties.[79] HOMO and LUMO are the analogy to the valence and conduction band in inorganic semiconductors. Even so this is an approximation because there are no real band-structures in organics, many models and key parameters can be transferred to organic semiconductors due to the splitting of the energy level into many states, rendering them energetically similar to a band structure (see figure 3.3).[80]

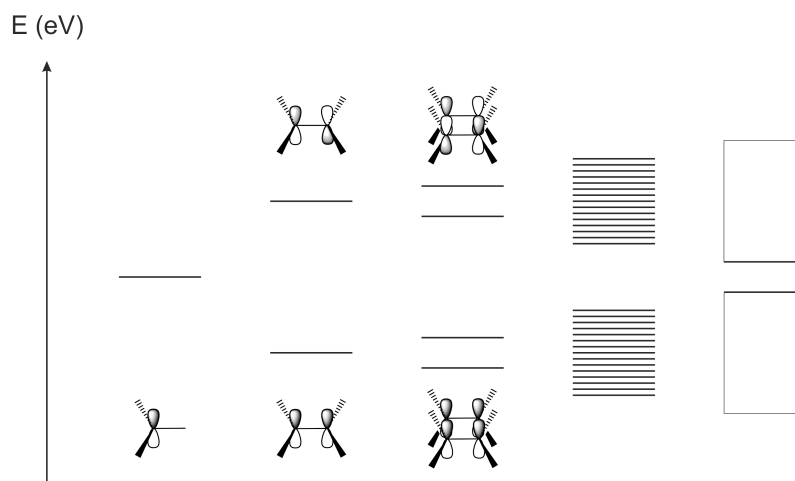


**Figure 3.3.** Splitting into orbitals with higher and lower energy, caused by interaction between molecular orbitals. In organic semiconductors, the difference between the individual orbitals is small enough to treat them as continuous band.

However, the microscopic charge carrier transport in inorganic and organic semiconductors is completely different. Inorganic semiconductors are crystalline and thereby bands are formed and so charges can move in the material.[81] However, organic semiconductors often form amorphous structures. Thus intra- and intermolecular charge carrier transport occurs. For the intramolecular transport, charge carriers can be stabilized by the conjugated bonds and move loss-free in the delocalized  $\pi$ -system (see figure 3.4 a). This leads to mobilities up to  $10 \text{ cm}^2/\text{Vs}$  over short distances.[82] In conjugated polymers, the optimum of a defect-free conjugated chain is impossible to reach because of the mostly amorphous structure. The chain is not completely flat over the whole distance. Kinks can occur, created by quinoid structures in aromatics (see figure 3.4 b) or *cis*- instead of *trans*-double bonds which turn the  $p_z$ -orbitals out of plane.[83]

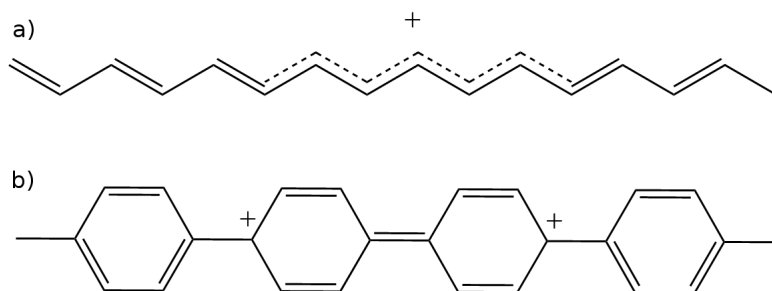


**Figure 3.4.** a) Stabilization of charges in a conjugated system. b) Formation of quinoid structures in conjugated aromatics which interrupt the delocalized system.

Due to the defects, it is not possible for charges to move along the whole length of the chain. Therefore, an important parameter is the effective conjugated chain length which is the average length between two defects in a polymer, typically around 10 monomer

units.[84, 85] To overcome the defects, the so called "hopping" processes take place, e.g., charge carriers tunnel from one  $\pi$ -system to another.[79] Following the same mechanism, charge carriers are transferred between molecules. The tunneling is temperature dependent, thus charge carrier transport of organic semiconductors increases with higher temperature. Nevertheless, the hopping-process still limits the transport and typical mobilities are between  $10^{-6}$  and  $10^{-2}$   $\text{cm}^2/\text{Vs}$ .[86–88] In comparison, inorganic silicon shows a mobility of  $1450 \text{ cm}^2/\text{Vs}$ .[89] Therefore, layers in organic devices have to be much thinner than in inorganic devices and, usually yielding thicknesses of a few hundred nanometers only.

## 3.2. Low-molecular weight materials versus polymers

In organic electronics two different classes of materials are distinguished: low-molecular weight materials and polymers. Most of them consist of conjugated aromatic ring systems.

### 3.2.1. Low-molecular weight materials

Low-molecular weight materials have a distinctly lower molecular weight than polymers and are thermally stable which enables their thermal evaporation. Evaporation yields very pure materials due to sublimation. By processing organic devices using evaporating techniques, it is easier to control the layer thickness. When processing low-molecular weight materials from solution, they often tend to crystallize, this is especially the case for very stiff molecules without any side-chains such as anthracene. This can be a big issue in organic electronics where the devices are at maximum a few hundred nanometers thick, so that crystals could lead to short cuts. Because of the smaller conjugated system, the conductivity of low-molecular weight materials is usually lower than in polymers. Some typical representatives are shown in figure 3.5:

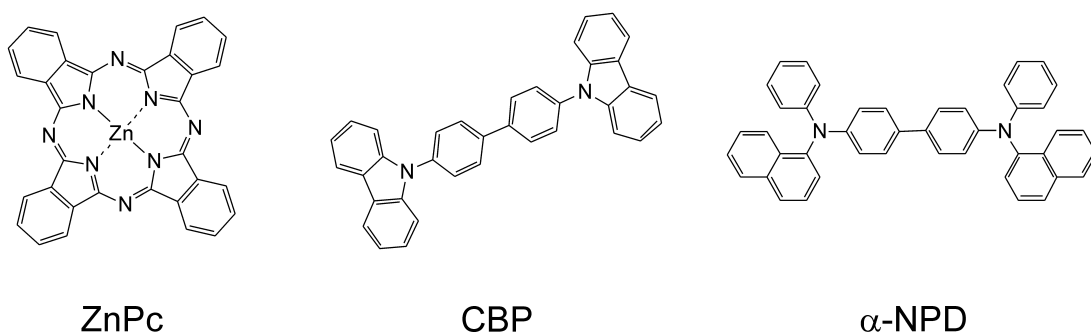


**Figure 3.5.** Typical low-molecular weight materials for organic electronics. Zinc phthalocyanine (ZnPc), 4,4'-bis(*N*-carbazolyl)-1,1'-biphenyl (CBP), *N,N'*-di(1-naphthyl)-*N,N'*-diphenyl-(1,1'-biphenyl)-4,4'-diamine ( $\alpha$ -NPD).

### 3.2.2. Polymers and general synthesis routes

Polymers usually consist of a chain made of several hundreds to thousand monomers. They do not have a uniform chain length, rather than a polydispersity with molecules of different molecular weights. There are lots of different polymers available, but for organic electronics a large conjugated  $\pi$ -system is crucial. Therefore, polymers containing conjugated ring systems are typically used. In comparison to low-molecular weight materials, it is more complicated to purify polymers. Because of their high molecular weight it is very challenging to evaporate polymers without destroying them. Therefore, they usually are synthesized with side-groups to enhance their solubility and are processed from solution. Due to their higher viscosity in solution compared to low-molecular weight materials with the same concentration, they are more suitable for printing processes. Additionally, polymers mostly form amorphous films. Generally two kinds of polymers are used: polymers with a conjugated backbone [90–92] and non-conjugated polymers with functional groups attached to side-chains.[55, 58, 59] Some typical polymers are shown in figure 3.6.

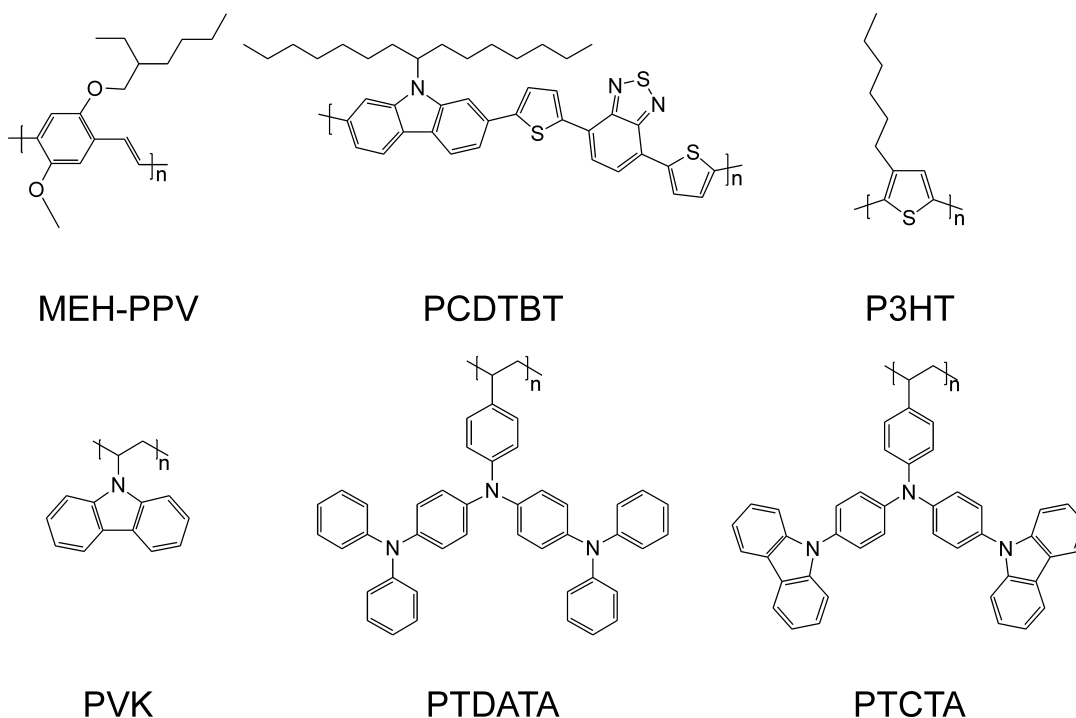


**Figure 3.6.** Typical polymers for organic electronics: Poly[2-methoxy-5-(2-ethylhexyloxy)-1,4-phenylenevinylene] (MEH-PPV), poly[*N*-9'-heptadecanyl-2,7-carbazole-alt-5,5-(4',7'-di-2-thienyl-2',1',3'-benzothiadiazole)] (PCDTBT), poly-3-hexylthiophene (P3HT), poly(9-vinylcarbazole) (PVK), poly-[4-*N,N*-bis[4-(*N,N*-diphenylamino)phenyl]aminovinylphenyl (PTDATA), poly-[*N,N*-bis[4-(carbazolyl)phenyl]-4-vinylaniline (PTCTA).

There are two different classes of polymerization: step growth and chain growth reactions. In step growth reactions, at first, two monomers react to dimers, then these react stepwise to oligomers then to polymers. Hence, high polymerization degrees ( $X_n$ ) are only reached at high fractional monomer conversion ( $P$ ) (see figure 3.7 green line) and the reaction is rather slow. For the chain growth reaction, few active monomers are formed with a starter (e.g. azobisisobutyronitrile (AIBN) for radical polymerization), where monomers are added during the polymerization. Hereby high  $X_n$  are reached at rather low  $P$  (see figure 3.7 black line) and the reaction is very fast.[70] The blue curve shows the living polymerization which is a chain growth reaction, that is not terminated. The chain growth reactions differ in radical, anionic, cationic and coordinative (e.g. Ziegler-Natta) polymerization depending on the active center of the monomers. Radical polymerization was used by the group of Dr. Krüger to synthesize the polymers used in this thesis, thus it will be in the focus of the following section.

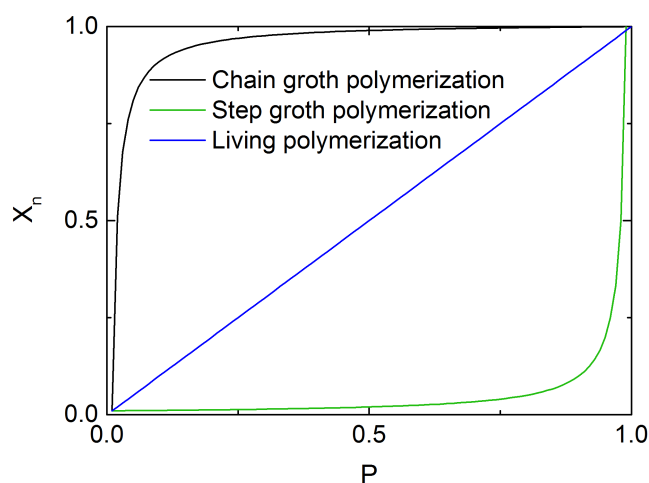


**Figure 3.7.** Polymerization degree against fractional monomer conversion for different polymerization techniques.

### 3.2.2.1. Radical polymerization

Chain growth reactions involve three different steps: starting reaction, growth reaction and termination. For better illustration the reactions will be explained on the example of the radical polymerization of styrene because the used polymers contain a polystyrene backbone. The starting reaction is usually the activation of the initiator by heat (e.g. AIBN) or light (e.g. dibenzoylperoxide)(see figure 3.8).



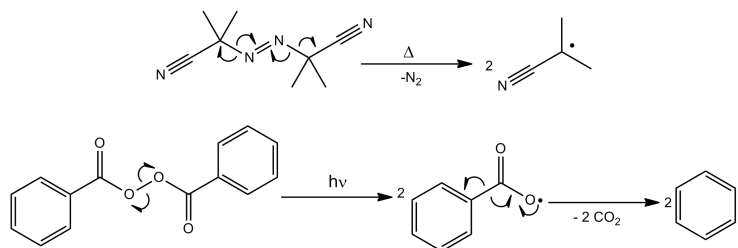


**Figure 3.8.** Thermally and light induced activation of initiators.

In the growth step further monomers are added to the chain (see figure 3.9). The speed of the reaction depends on the stability of the radical. If the radical is resonance stabilized, the reaction is slower than with an unstabilized reactive radical.

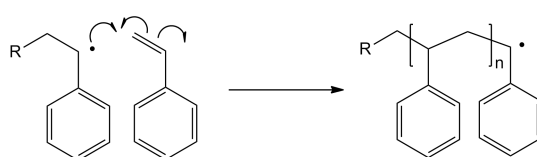


**Figure 3.9.** Chain growth of polystyrene by radical polymerization.

Another possible reaction during the chain growth is the chain transfer reaction (see figure 3.10). Here, one atom (mostly hydrogens or halogens) is transferred from a molecule to the chain and thus a radical is created in the molecule. Using this reaction, it is possible to get branches on the polymer backbone.

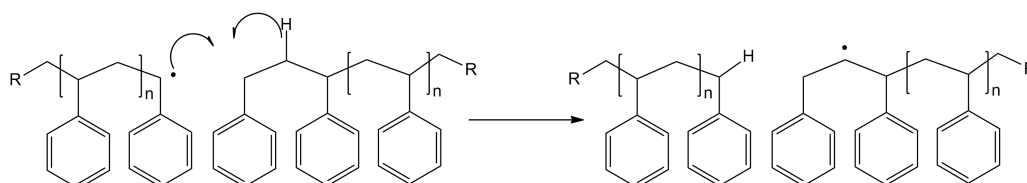


**Figure 3.10.** Chain transfer reaction between two polymers.

If two containing radical chain ends meet, they will react with each other. Two termination reactions are possible. One option is disproportionation (see figure 3.11).

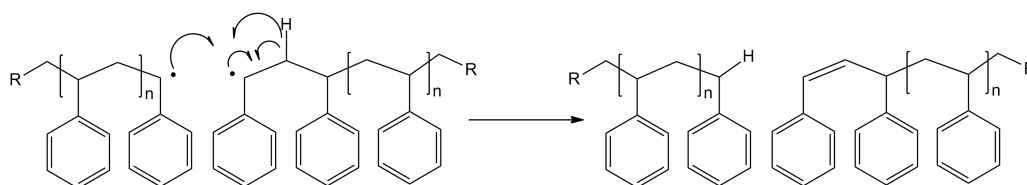


**Figure 3.11.** Termination by disproportionation reaction of two radicals.

Another option is combination (see figure 3.12).

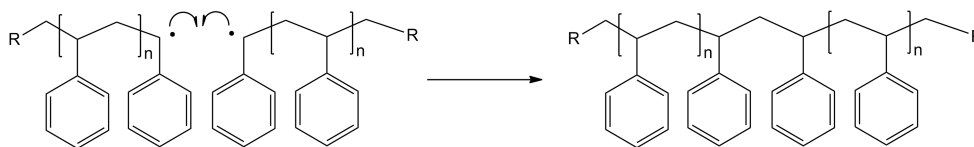


**Figure 3.12.** Termination by combination reaction of two radicals

In the first case, the degree of polymerization remains the same, in the second case it is doubled. Specifically to stop a reaction, retarders or inhibitors can be added. Both will react with the radicals, but the retarder only slows down the reaction while the inhibitor completely stops it. One example are stabilized radicals like 2,2,6,6-tetramethylpiperidin-*N*-oxyl (TEMPO).

The polymerization reaction is temperature dependent, thus it becomes faster if the temperature is increased. Due to the exothermic reaction of most radical polymerizations and the increasing viscosity with increasing degree of polymerization, termination reactions and the transportation of heat are hindered and the reaction will accelerate itself which is called Trommsdorff effect. In the worst case pressure builds up in the reactor due to the exothermic reaction which may destroy the reactor. This effect is isothermal and thus to prevent self-acceleration of the reaction efficient cooling of the reaction mixture is essential. Additionally controlled radical polymerization such as Atom Transfer Radical Polymerization (ATRP) or Reversible Addition-Fragmentation Chain Transfer Polymerization (RAFT) can be used to have better influence on the reaction conditions.[70]

### 3.2.2.2. Copolymerization

If a polymer consists of just one sort of monomers, it is called a homo-polymer. With two or more types of monomers there are different options to arrange the monomers in specific orders. These so called copolymers can be divided into statistic, alternating and block-copolymers. In case of two monomers (A and B), the result is a statistic polymer (AABBABBBBAABA) if the reactivity of the formed radicals is the same for the reaction with A and B. If A prefers the reaction with B and B the reaction with A alternating copolymers are formed (ABABABABABAB). Block-copolymers are built in case every monomer type favors the reaction with itself (AAAAAABBBBBB). Copolymers usually exhibit a mixture of the properties of their homo-polymers and their melting points and glass temperatures are lower.[70] The used crosslinkable polymers used in this thesis are statistic co-polymers of a hole transporting and a crosslinkable monomer.

### 3.2.2.3. Crosslinkable Polymers

In organic electronic devices, multiple layers are applied on top of each other. This can easily be achieved using evaporation techniques. However, polymer layers have to be processed from solution. In this case, already processed layers can be dissolved in the polymer solution for the next layer. To prevent this, two concepts are commonly employed. Orthogonal solvents can be used which is not easy because many organic materials are soluble in the same or at least similar solvents.[60, 61] Another option is to ensure insolubility of the applied layer, e.g., by crosslinkable materials. Their advantage is, that they are soluble before crosslinking and can be applied on a substrate and afterwards crosslinked and become insoluble.[62, 63, 93]

## 3.3. Organic solar cells

### 3.3.1. Charge carrier generation

In inorganic semiconductors, all photons with energies higher than their energy gap will be absorbed. In contrast, organic semiconductors can only absorb in a defined wavelength regime, due to narrow absorption bands, mostly in the visible light. Nevertheless, they exhibit a high absorption coefficient of around  $10^5 \text{ cm}^{-1}$ . Therefore, a significant part of sun light can be absorbed using thin layers.[91]

If a photon has enough energy to excite an electron from the HOMO of the organic semiconductor to its LUMO, it can be absorbed. Hereby an exciton, a coulombically bound electron-hole pair is created. In inorganic semiconductors, excitons generally dissociate at room temperature due to low exciton binding energies of these materials.[80] Contrary, organic semiconductors exhibit binding energies of 0.4-1.4 eV[94] which is too large to separate the excitons at room temperature. A common way to dissociate electron-hole pairs in organic solar cells is the use of an absorbing layer containing a donor and an acceptor material. If the difference between the LUMOs of the donor and acceptor material is larger than the exciton binding energy, electron-hole pairs on the donor dissociate at the donor-acceptor interface. The average diffusion length of an exciton is typically around 10 nm before it recombines.[95] Hence bi-continuous structures of donor and acceptor are used as absorbers. Therefore, donor and acceptor materials are mixed before applying atop the electrode. Those OSCs are called bulk-heterojunction solar cells.

### 3.3.2. Organic solar cell architectures

An OSC contains, at minimum, an absorbing layer which converts light into charge carriers, and two electrodes, at least one of them being transparent. Additionally, charge carrier transport layers can be used to decrease voltage losses by generating ohmic contacts to the electrodes and blocking layers with suitable energy levels to hinder charges to pass through and recombine at the electrodes. The architecture of a typical example of an OSC is shown in Fig. 3.13.

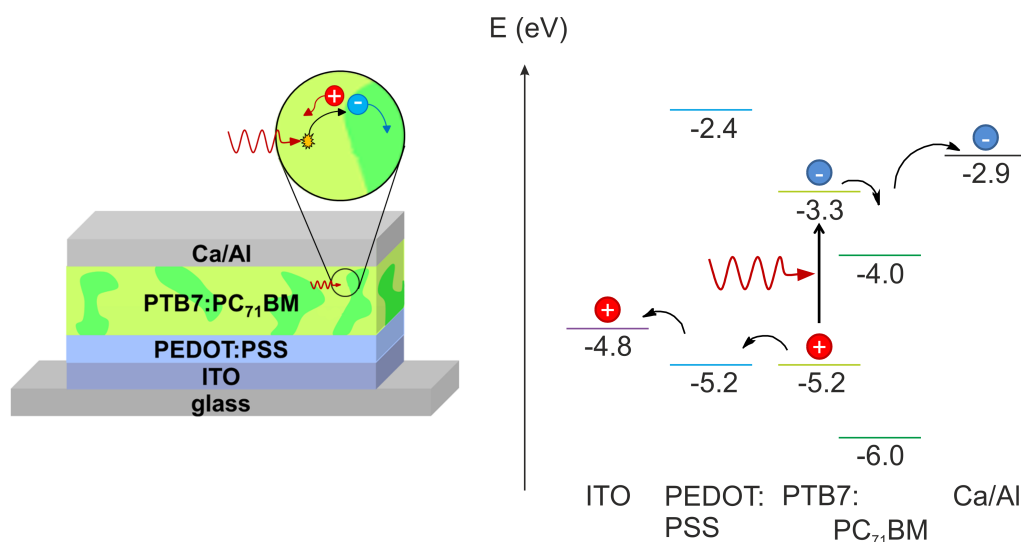


**Figure 3.13.** Device architecture and energy diagram of a typical organic solar cell. The energy levels were taken from the literature.[23, 96, 97] If a photon is absorbed in the donor of the absorber, an exciton is created. This can be separated at the donor-acceptor interface into a hole and an electron which will be transported to the electrodes.

Generally, an absorber for organic solar cells is a mixture of an electron donor and an electron acceptor material. Poly[[4,8-di(5-ethylhexyloxy)benzo[1,2-b;4,5-b]dithiophene][3-fluoro-2[(2-ethylhexyl)carbonyl]thieno[3,4-b]thiophenediyl]] (PTB7) mixed with [6,6]-phenyl  $C_{71}$ -butyric acid methyl ester ( $PC_{71}BM$ ) is a typical representative.[96] To enhance the contact to the electrode, PEDOT:PSS is used as a hole extraction layer (HEL). Underneath, as a transparent electrode, ITO is used as anode. The cathode is usually made of a metal with a low work function such as calcium (Ca) which is covered by aluminum (Al) to avoid oxidation. A possibility to avoid reactive metals is to use an inverted architecture.[51] Here, ITO works as cathode and the anode is made from silver (Ag). To enhance contact to the electrode, zinc oxide (ZnO) is used as electron extraction layer (EEL) between the absorber layer and the ITO as well as molybdenum oxide ( $MoO_x$ ) between absorber and silver electrode. The choice of electrode materials is crucial for the performance of the solar cell, because the difference of their work functions limits the device's photo voltage.

### 3.3.3. Key performance parameters

As a simplification, an organic solar cell can be described as a diode. For characterization, current density-voltage curves (J-V) are measured. To compare solar cells with different sizes, the current is normalized by dividing through the active area of the cell. The J-V curve of an illuminated ideal solar cell is about equivalent to the non-illuminated dark curve, shifted by the photo-current (see figure 3.14). The intersection of the curve with the current density axis is commonly referred to as short-circuit current density ( $J_{SC}$ ) and equals the current density in the case of short-circuiting the contacts and hence a voltage of 0 V. It depends on the amount of absorbed light which is controlled among others by the position and width of the absorption band and the thickness of the absorber layer. The maximum photon flux of the sun is in the regime of 600-800 nm, therefore, usually materials with absorption bands are used in OSC.[92]

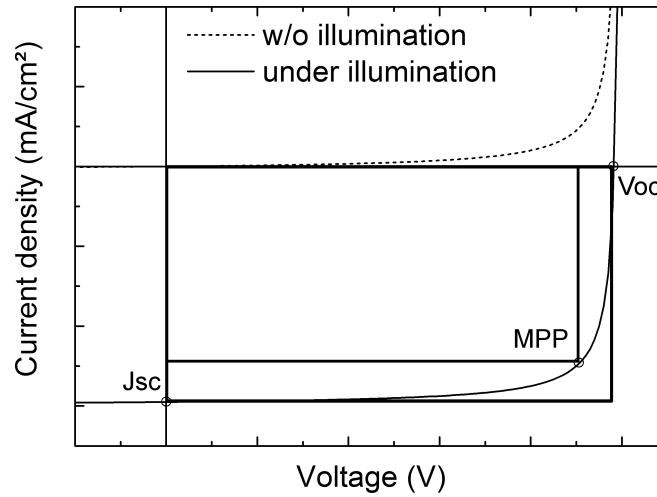


**Figure 3.14.** Characteristic J-V curve of a solar cell measured without (dashed line) or under illumination (solid line) including all characteristic key performance parameters.

The open-circuit voltage ( $V_{OC}$ ) is the intersection at the voltage axis and shows the voltage if no load is connected and hence no current is flowing. In bulk-heterojunction solar cells, it is determined by the difference of the HOMO of donor and LUMO of acceptor.[98–101] Therefore, the work function of the electrodes must be aligned to them so that no voltage losses occur.[102] Another important parameter is the fill factor (FF). It can be calculated by the following equation:

$$FF = \frac{V_{MPP} \cdot J_{MPP}}{V_{OC} \cdot J_{SC}} \quad (3.1)$$

The FF is the ratio of the maximum power of the solar cell, measured at the so called maximum power point (MPP), and the product of open-circuit voltage and short-circuit current density. The FF is limited by the parallel and serial resistances. Short cuts enhance the parallel resistance ( $R_P$ ) which is a measure of the reverse characteristic of the OSC. Voltage losses, such as ohmic losses at the electrodes, have an effect on the serial resistant ( $R_S$ ). In an ideal solar cell the  $R_P$  should be maximal and the  $R_S$  minimal.[101, 103] Thus low recombination rates and ohmic contacts at the electrodes lead to higher fill factors. Keys are the layer thickness of the absorber, its morphology and the used transport layers.[104]

The maximum solar cell power divided by the power of the incoming light ( $P_{in}$ ) yields the power conversion efficiency (PCE) (see equation 3.2).

$$PCE = \frac{P_{out}}{P_{in}} = \frac{V_{OC} \cdot I_{SC} \cdot FF}{P_{in}} \quad (3.2)$$

The power of the incoming light is set by standardized conditions. The American Society for Testing and Materials Standards (ASTM) set the irradiation intensity at about 1000 W/m<sup>2</sup> and the spectrum of the sun as the spectrum that reaches the earth's surface at illumination under an angle of 37° which corresponds to a transition through 1.5 atmospheres (AM1.5). It is measured at 25°C.[105, 106] The spectrum is shown in figure 3.15.

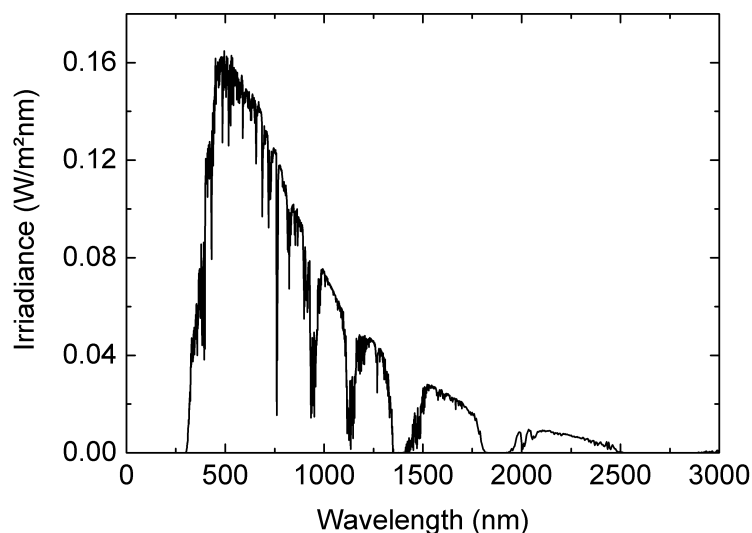


**Figure 3.15.** AM1.5 reference spectrum of solar irradiation under an angle of 37°.[107]

## 3.4. Organic light emitting diodes

### 3.4.1. Working principle

Electrons and holes are injected from the electrodes by applying an external electrical field.[108] They are transferred into the emitter via hopping processes. If an electron and a hole meet, an exciton is created which will eventually recombine. Only if recombination takes place in the emitting material it can be a radiative recombination, commonly described as electroluminescence. Therefore, blocking layers ensure that charges are confined on the emitter. Injection layers are introduced to lower the injection barrier at the electrodes and hence to ensure lower driving voltages. Dipoles like alkali salts can be used to improve band alignment at the electrodes.[13, 14]

Generally 25% of the created excitons are singlet excitons which recombine under fluorescence. The remaining 75% are triplet excitons which recombine under phosphorescence. Hence in singlet emitters, three fourth of the excitons are lost to non-radiative recombination.[109] Therefore, in efficient OLEDs, phosphorescent emitters such as iridium complexes are used to exploit the singlet and triplet excitons and reach higher luminance.

Parts of the generated light escapes through the transparent electrode, while most of it is partly absorbed in the other layers or backscattered at the metal electrode.

### 3.4.2. Architecture of organic light emitting diodes

The architecture of OLEDs contains two electrodes, at least one of them being transparent, and an emission layer inbetween. Charge carrier injection layers improve the contact to the electrodes and lower the driving voltage. Blocking layers prohibit recombination of charges at the electrodes. For illustration a representative architecture is shown in figure 3.16:

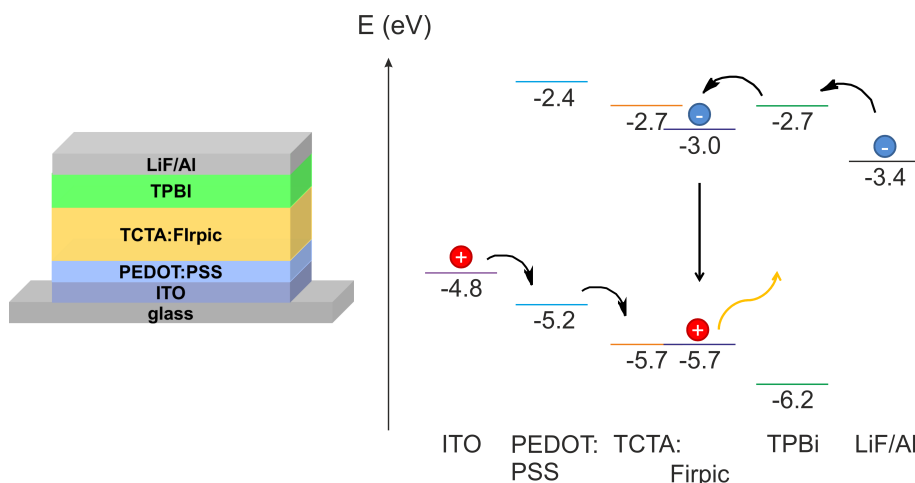


**Figure 3.16.** Device architecture and energy diagram of a typical organic light emitting diode. Energy levels were taken from the literature.[23] Electrons and holes are injected from the electrodes. When they meet in the emission layer, they recombine, creating a photon.

In a typical organic light emitting diode, ITO is used as a transparent anode with a high work function of 4.8 eV.[110] Atop, PEDOT:PSS is used as a hole injection layer (HIL). As an efficient emitter, often phosphorescent iridium complexes embedded in a host are used. 4,4',4''-Tris(carbazol-9-yl)-triphenylamine:iridium(III)bis[(4,6-fluorophenyl)-pyridinato-*N,C*<sup>2</sup>]picolate (TCTA:FIrpic) is a common representative of this class of materials. 1,3,5-tris(1-phenyl-1*H*-benzimidazol-2-yl)benzene (TPBi) is usually applied as hole blocking layer while an ultra-thin layer of a dipolar salt such as lithium fluoride (LiF), covered with Al, serves as cathode.[23]

### 3.4.3. Key performance parameters

An OLED can also be described as a diode. Similar to OSCs, current density-voltage curves are measured to provide electrical information. However, for organic light emitting diodes, additional optical characterization is required.

The sensitivity of the human eye is different for different wavelengths. E.g., at the same physical intensity, green appears brighter than blue or red. Therefore, photometrical characteristics are weighted with the sensitivity of the human eye ( $V(\lambda)$ ). The luminous flux is the photometrical equivalent to the radiometrical radiant flux and describes the perceived power of the light weighted by the sensitivity. It can be calculated as follows:

$$\Phi = K_m \int_{380nm}^{780nm} \Phi_e(\lambda) \cdot V(\lambda) d\lambda \quad (3.3)$$

$K_m = 683 \text{ lm/W}$  is a conversion factor and  $\Phi_e(\lambda)$  is the radiation power. The luminance ( $L$ ) is a measure for the brightness perceived by an observer. It is the derivative of luminous intensity divided by the area, corrected by the angle between observer and the surface normal. OLEDs can be considered as lambertian sources, e.g., the light is emitted uniformly in all directions. Thus the luminance can be calculated by equation 3.4.

$$L = \frac{\Phi}{A \cdot \pi} \quad (3.4)$$

The current efficiency  $\eta_c$  is a measure of conversion of electrons into photons. It is a quantum efficiency weighted with  $V(\lambda)$ , neglecting voltage losses, and can be calculated by dividing the light intensity  $I_L$  by the current intensity  $I_C$ .

$$\eta_c = \frac{I_L}{I_C} \quad (3.5)$$



The ratio of the luminous flux and the electrical power  $P$  provides the power efficiency of the OLED which is the common measure for the efficiency of the device.

$$\eta_p = \frac{\Phi}{P} \quad (3.6)$$

In table 3.1 a summary of all parameters including units can be found.

**Table 3.1.** Key performance parameters of OLEDs.

	Symbol	Unit
Luminous flux	$\Phi$	lm
Luminance	L	cd/m <sup>2</sup>
Current efficiency	$\eta_c$	cd/A
Power efficiency	$\eta_p$	lm/W

### 3.5. Electrical doping of organic semiconductors

The first conductive polymer polyacetylen has a very low conductivity, caused by a Peierls distortion of the C-C-bonds. Because alternating single and double bonds are energetically more favorable than a completely delocalized backbone, in PA, a bond-length alternation exists. In polymers including aromatic ring systems, the conductivity decreases due to the torsion of the rings as a result of the steric hindrance and an optimal overlap of the  $\pi$ -orbitals is no longer possible. In addition, aromaticity has to be abandoned if free charges are created which is not favorable. A solution for this problem was found by oxidizing (p-doping) or reducing (n-doping) of the conjugated molecules. Due to redox reactions, positive and negative charges are formed which can be stabilized in the conjugated system and increase the charge carrier density.[83] Hence the doping in organic semiconductors works quite different to their inorganic counterparts, where doping is achieved by introducing impurities with more or less valence electrons than the semiconductor.

#### 3.5.1. Effect of electrically doped layers in organic electronic devices

Electrically doped semiconductors are commonly used as transport layers, in the active material and even in the electrodes (e.g. highly conductive PEDOT:PSS as transparent electrode).[43] In this work doped charge extraction/injection materials have been investigated. Therefore, the following description will focus on these materials.

In both, OSC and OLED, charge carriers are transported between the electrodes and the active material. Thus it is important to reduce losses due to barriers between them. Doping is a very suitable way to guarantee loss-free charge carrier transport in optoelectronic devices. In figure 3.17 the Fermi-level alignment is illustrated on p-doping.

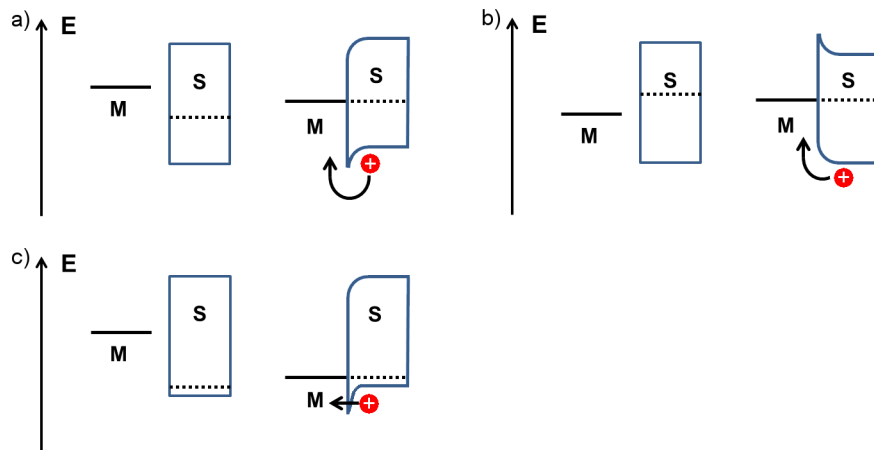


**Figure 3.17.** Alignment of the work function of a metal with the Fermi-level of a semiconductor. a) Formation of a barrier for holes when the work function is higher than the Fermi energy of the semiconductors. b) The Fermi-level is higher than the work function of the metal and no barrier exists. In the last picture the Fermi-level is shifted close to the HOMO of the semiconductor, and after alignment the created barrier is narrow enough to allow the holes to tunnel the barrier.

If a metal and a semiconductor with different work functions or Fermi energies, respectively, are in contact to each other, a charge equalization occurs, their Fermi-levels align and an internal electrical field results.[111] In an optoelectronic device with a lot of different layers, a voltage drop over the whole device occurs.[112] Due to this Fermi-level alignment, barriers of the height of the energetical difference between the work function and the Fermi-level can be formed if the Fermi-level of the semiconductor is energetically lower than the work function of the electrode (see figure 3.17 a). In this case, high voltages are needed to overcome these barriers. Only if the materials are chosen so that the Fermi-level of the semiconductor is energetically higher than the work function of the metal, no barriers are created (see figure 3.17 b). Therefore, it is crucial to use doped semiconductors where the Fermi-level is shifted to the HOMO and therefore the created barriers are narrow enough to allow charges to tunnel the barrier (see figure 3.17 c). Hereby an ohmic contact is created which reduces ohmic losses at the interfaces and enhances charge carrier injection. A different possibility to achieve this effect is to use metal oxides with high work functions or strong dipoles.[23] Another advantage of doping

is the creation of free charges. In this process the charge carrier density and hence the conductivity increases. [25]

n-Doping follows the identical mechanism, but the work function of the electrode aligns with the Fermi-level of the electron transport material which is located near the LUMO instead of the HOMO.

### 3.5.2. Doping mechanisms

#### 3.5.2.1. p-Doping using organic acceptors

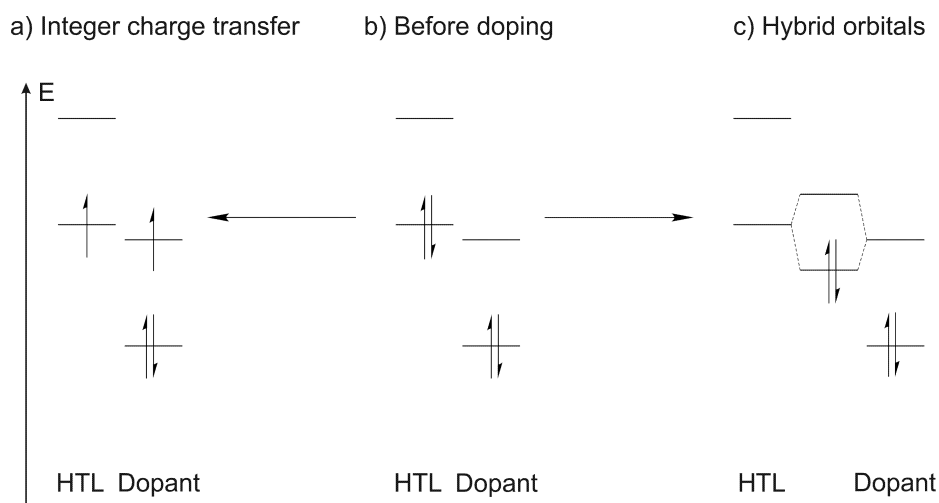


**Figure 3.18.** Different doping mechanisms: In the middle the energy level and distribution of spins on these energy levels before doping is shown. The left side depicts the doping mechanism of an integer charge carrier transfer between HTL and dopant and the right side the formation of hybrid orbitals.

Two doping mechanisms are discussed controversially. Both are depicted in figure 3.18 for p-doping exemplary. Gao et al. published a mechanism describing p-doping by a transfer of an electron from the HOMO of the matrix material to the energetically lower LUMO of the dopant molecule (see left part of figure 3.18). Hereby the Fermi-level of the matrix is shifted to the HOMO.[26] In contradiction Salzmann et al. found a formation of hybrid orbitals from the HOMO of the matrix and the LUMO of the dopant (see right side of figure 3.18).[113] In general, the mechanism that takes place depends on the characteristics of the system.

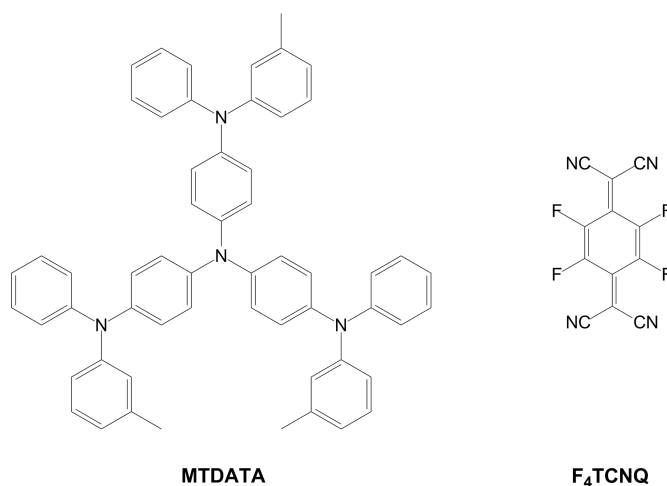


**Figure 3.19.** Hole transport material 4,4',4''-tris[phenyl(*m*-tolyl)amino]triphenylamine (MTDATA) and organic acceptor 2,3,5,6-tetrafluoro-7,7,8,8-tetracyanoquinodimethane (F<sub>4</sub>TCNQ).

MTDATA is a hole transport material with a HOMO level of -5.1 eV (versus vacuum).[114] In case of p-doping, strong acceptors with a lower LUMO such as F<sub>4</sub>TCNQ ( $E_{\text{LUMO}} = -5.4$  eV) are required.[115] These molecules have been proven to be a suitable matrix-dopant combination used for hole injection in vacuum processed OLEDs.[27, 28]

### 3.5.2.2. n-Doping using alkali metals

In case of n-doping an electron is transferred from the HOMO of the dopant to the lower LUMO of the matrix material or hybrid orbitals from the HOMO of the dopant and the LUMO of the matrix are created. Hereby the Fermi-level of the matrix is shifted to LUMO level.

There are different options for n-doping of organic semiconductors in vacuum processed organic devices. One option is the doping with alkali metals due to their low work function.

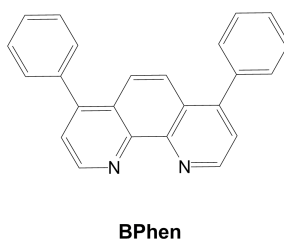


**Figure 3.20.** Electron transport material 4,7-diphenyl-1,10-phenanthroline (BPhen.)

As electron transporter, usually materials with high LUMO levels are used, e.g., BPhen (-3.0 eV).[116] To dope these, materials with a very low work function are required. Known materials which comply with this requirement are alkali metals. They are very reactive and require only very little energy to remove the valence electron from their s-orbital. As such, BPhen:Li has proven itself a suitable combination in OLEDs.[27, 117]

### 3.5.2.3. n-Doping using cationic dyes

Another option to n-dope organic semiconductors is the doping with cationic dyes. Here the active form of the dopant is generated *in-situ* by thermal stimulus or light excitation.

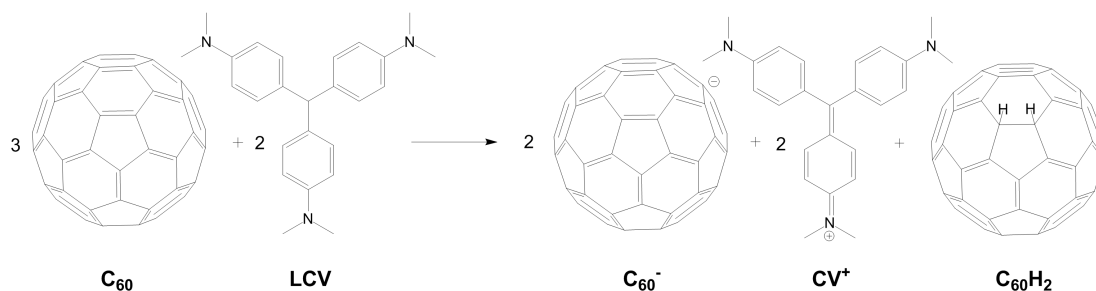


**Figure 3.21.** Doping reaction of  $\text{C}_{60}$  with leuco crystal violet (LCV). An electron is transferred from LCV to a fullerene and the resulting radical cation is stabilized by transfer of a hydrogen radical to another fullerene. Thereby the dye is oxidized into crystal violet and the fullerene is hydrogenated.

In this case, the dye is reduced into its leuco base. In its leuco form, an electron is transferred to the LUMO of the electron transport material, generating a radical cation. This radical cation is stabilized by oxidation of the dye and hence by hydrogenation of another fullerene by a transfer of a hydrogen radical. In this case, the reaction is no longer reversible.[32, 118]  $\text{C}_{60}$  doped with cationic dyes is a well investigated system for vacuum processed OSC.[32–34, 119]



## 4 | Optoelectronic material and device characterization

### 4.1. Sample preparation

All solutions were processed by spincoating. Hereby some  $\mu\text{l}$  of the solution were pipetted on a substrate which was rotated with velocities over 500 rpm afterwards. Because of the centrifugal forces the solution is spread over the whole substrate and most of it is tossed away. Only a thin homogeneous film remains. The thickness of this film mostly depends on the concentration of the solution and the velocity of the rotation.

Layers such as the metal electrodes were evaporated in a vacuum chamber (Spectros) from Kurt J. Lesker at around  $10^{-6}$  mbar through a shadow mask to ensure that only specific parts of the samples were covered. This evaporation chamber contains six thermal evaporators, two for metals and inorganic salts and four for organic materials. For coevaporation it is possible to use two organic sources at the same time. For this purpose they are separated by a separating plate. The thickness of the film is controlled *in situ* by quartz crystals.

### 4.2. Characterization methods

#### 4.2.1. Structural insights in chemical reactions of sodium doped TPBi by NMR

Sodium is known as an initiator in anionic polymerization processes, thus undoped and sodium doped TPBi was measured with nuclear magnetic resonance spectroscopy to evaluate if polymerization occurs. In Nuclear magnetic resonance (NMR) coupling of neighboring hydrogen atoms and interaction with heavier atoms can be detected and informations about the chemical structure can be obtained.

## 4.2.2. Layer thicknesses and current measurements

### 4.2.2.1. Tactile stylus surface profiler

In general, organic layers are very thin (typically below 500 nm). The film thicknesses were measured with a tactile stylus surface profiler (Dektak XT, Bruker) under ambient conditions. First, some material is removed by scratching the layer with a needle. Then the scratch is scanned at a defined force by a diamond needle with a very small tip. On the basis of the deflection of the needle the height profile is calculated and the layer thicknesses can be obtained.

### 4.2.2.2. Atomic force microscopy

Atomic force microscopy (AFM) measurements are performed in a similar way to tactile stylus surface profile measurements. The surface is scanned with a tip and profile information are derived by detection of the deflection of the tip. In contrast, AFM is usually used to get an three-dimensional picture of the sample surface (e.g. to get information about the roughness). It also has a higher resolution up to few nanometers, because the tip is attached to a cantilever connected to a piezo-element which detects very small deflections. This is important because the deflection of the tip is caused by interactions of the tip with the surface which can be very weak (e.g. van der Waals forces). To detect the deflection, a laser is reflected from the top surface of the cantilever to an array of photodiodes.

From the surface profiles, the root-mean-square roughness ( $R_q$ ) of the sample can be calculated as an average of the difference between the mean of all measuring points ( $z_0$ ) and the value of the single measuring point ( $z_i$ ) over the total amount of points ( $N$ ).

$$R_q = \sqrt{\frac{1}{N} \sum_{i=1}^N (z_0 - z_i)^2} \quad (4.1)$$

There are different measurement modi to characterize the surface. The easiest way is to bring the tip in contact with the surface and scan it. If the surface is too soft, it is easily destroyed by scratching over it. This may corrupt the results. An alternative way is the tapping mode. Hereby the oscillating cantilever is induced close to its resonance frequency. When approaching the sample, the resonance frequency is changed due to additional forces between tip and surface which can be detected and converted to a height profile. Another tapping mode is the peak-force-tapping mode. Hereby the piezo is excited in a sine wave, touching the surface at the lowest point of the oscillation at a defined deflection. Near the surface, the tip is attracted due to adhesive forces which results in a detectable change in the oscillation.



Space-resolved currents can be measured by peak-force-TUNA-AFM (PF-TUNA-AFM). In this case, the samples have to be prepared on a conductive substrate. A voltage is applied between the substrate and the tip and the resulting current and its direction can be measured. When measuring currents in peak-force-tapping mode (PF-TUNA), three different currents can be detected: The peak-current is the current flowing on the lowest point of the tip. The contact current is the current over the whole time when the tip touches the surface. The TUNA-current is the average over the whole period including the non-contacting time.

### 4.2.3. Characterization of the electron transfer

Upon doping, an electron is transferred either from the matrix to the dopant (p-doping) or from the dopant to the matrix (n-doping). This electron transfer can be investigated by different methods.

#### 4.2.3.1. UV-vis-NIR spectrometry

Molecules (especially with  $\pi$ -electrons) absorb light, exciting electrons to higher molecular orbitals (MOs). The wavelength of the absorbed light corresponds to the energy difference between the original MO of the electron and the MO it is excited to. In case of doped materials, the necessary absorption to excite the transferred electrons can be measured.

In an ultraviolet-visible-near-infrared (UV-vis-NIR) spectrometer, the probe light is compared to the light after passing through the sample. The wavelengths are selected by a monochromator and alternately directed through the sample and a reference sample (e.g. pure solvent or empty substrate). By comparing the intensities of the two beams, detected by a photodiode, the transmission is calculated. In this work absorbance is used instead of absorption, due to the weak absorption of the materials under study. It can be calculated by equation 4.2:

$$A = -\log_{10} T \quad (4.2)$$

#### 4.2.3.2. Electron paramagnetic spin resonance spectroscopy

Another possibility to prove the electron transfer due to the doping is the detection of unpaired spins by EPR spectroscopy. Hereby all unpaired spins are aligned along an external magnetic field and the spins are arranged in two energetic states with different spin quantum number ( $m_s = \pm\frac{1}{2}$ ). Transitions between the two energy levels can be induced by resonant microwave absorption and can be detected afterwards.

Room temperature continuous wave electron paramagnetic resonance (cwEPR) spectra were recorded using a home-built X-band EPR spectrometer. Therefore, 50  $\mu\text{l}$  of the studied solutions were filled in EPR tubes, the solvent was removed under vacuum, the tubes were filled with inert gas and sealed using a blowtorch. The magnetic field was regulated by a field controller (Bruker BH15) and a microwave bridge (Bruker ER 048 R) was used for microwave generation and detection. Magnetic-field modulation in combination with lock-in detection was employed using a lock-in amplifier (Stanford Research SR810) and a modulation amplifier (Wangine WPA-120). The described setup was used to measure derivative spectra. In case of the measurement of the doped and undoped fullerenes the samples were placed in a Bruker ER 4122 SHQ microwave resonator and illuminated with white light (Streppel hololux 110HI) through a window. The quality factor Q of the resonator loaded with the sample was determined from the mode picture before each EPR measurement was started.

The measured derivative spectra were background-corrected and double integration was performed to obtain the integrated EPR signal amplitude. This intensity was compared to the double integrated intensity of a reference sample with a known number of spins (4-hydroxy-TEMPO dissolved in toluene). Taking Q into account, as measured for the respective sample and all experimental parameters that influence the signal intensity, this comparison yields the absolute number of spins.[120] The uncertainty with respect to the absolute number of unpaired spins is less than 20% which is estimated based on the uncertainty of the sample volume when filling the tubes.

#### 4.2.4. Determination of energy levels

p-Doping leads to electron depletion of the HOMOs of the hole transport materials. Thus a shift of the ionization potential  $E_I$  to lower energies is expected. Due to the sensibility to oxygen of n-doped materials it is not possible to measure them under ambient conditions. Therefore, the p-doped layers were studied by photoelectron yield spectroscopy in air, while the n-doped layers were measured by Kelvin probe force microscopy in a glovebox under inert atmosphere. The ionization potential and electron affinities of neat and mixed (20 mol% dopant) were computed by DFT.

#### 4.2.4.1. Photoelectron yield spectroscopy in air

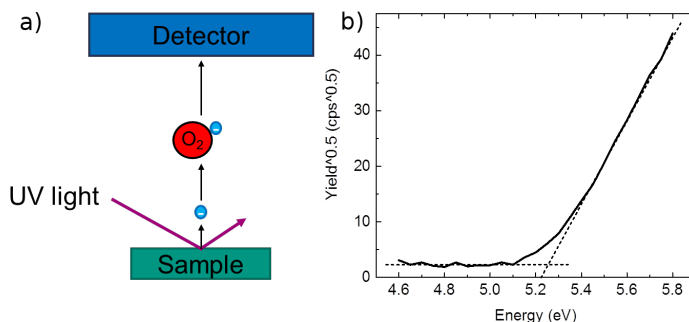


**Figure 4.1.** a) Working principle of photoelectron yield spectroscopy in air. Electrons are ejected from the sample surface by UV-light excitation and ionize the ambient oxygen. These ionized oxygen molecules can be detected and the number of ejected electrons can be calculated. b) The resulting work function can be derived from the spectrum at the intersection of the ground level and the slope of the curve.

The measurement principle of photoelectron yield spectroscopy in air is similar to ultraviolet photoelectron spectroscopy (UPS). Electrons are ejected from the sample surface by irradiation with UV-light and transported to an anode, where they are detected (see figure 4.1 a). In contrast to UPS, in PESA measurements not the kinetic energy but the total amount of the electrons dependent on the energy of the UV-light is measured. This way the work function, in case of metals, or the HOMO-level, in case of organic material, can be determined. An advantage of PESA is that no high vacuum is needed, because the ionized oxygen is measured instead of the free electrons. Thus organic materials can be measured under ambient conditions which is much closer to normal working conditions of organic electronic. The work function was obtained at the intersection of the tangents of the ground level and the slope of the resulting curve (see figure 4.1 b).

#### 4.2.4.2. Kelvin probe force microscopy

Kelvin probe force microscopy (KPFM) is used to measure the potential difference between a sample and the KPFM tip. To gain information about the contact potential, the data have to be compared with the measured data of a reference of known contact potential. To perform such a measurement, the sample is electrically bonded to the AFM. If the tip approaches the sample it is eventually near enough to induce electrons from the material with the lower work function to the material with the higher work function. Thereby the Fermi-level of the tip and the sample align. An additional force on the cantilever is generated by the charged surface which is minimized by applying an external voltage. Therefore, a DC voltage is applied between the tip of the cantilever and the sam-

ple. Two measurement modi are employed: The additional force on the cantilever can be detected by modulation of the amplitude (AM-KPFM), or the gradient of the force can be detected by modulation of the frequency (FM-KPFM).[121] In this work, FM-KPFM was used. Hereby the cantilever is set into vibration with the resonance frequency. When applying an AC voltage, the resonance frequency is shifted. The oscillation of the tip with the frequency of the AC voltage can be detected. From this shift, the force gradient can be calculated.

#### 4.2.4.3. Simulation of energy levels

Molecular conformations were obtained by simulations employing DFT based geometry optimizations as implemented in Turbomole using a B3-LYP functional and a def2-SV(P) basis-set.[122–124] Partial charges were taken from DFT calculations. Potentials for the soft inner-molecular degrees of freedom (dihedral angles) were obtained using the semi-empirical PM6 method as implemented in MOPAC2012.[125, 126] Atomistic morphologies containing about 1000 molecules per system were generated using the Monte Carlo (MC) based simulated annealing protocol SIMONA/DEPOSIT,[127] simulating 10 annealing cycles (SA) with 150.000 MC steps per molecule. The temperature was reduced from 4000 K to 300 K during each SA cycle. The ionization potentials and electron affinities of MTDATA, F<sub>4</sub>TCNQ, HATCN<sub>6</sub> in mixed (20 mol% doping concentration) and pristine systems were calculated using the Quantum Patch method.[128, 129]

#### 4.2.5. Electrical sample characterization

For building optoelectronic devices, the material conductivity is important. The common measurement with monopolar devices is discussed controversially. Therefore, after evidencing doping with measurements described above, in this work, the conductivities were measured by monopolar devices and additionally by charge extraction by linear increasing voltage, and the results were compared.

##### 4.2.5.1. Monopolar Devices

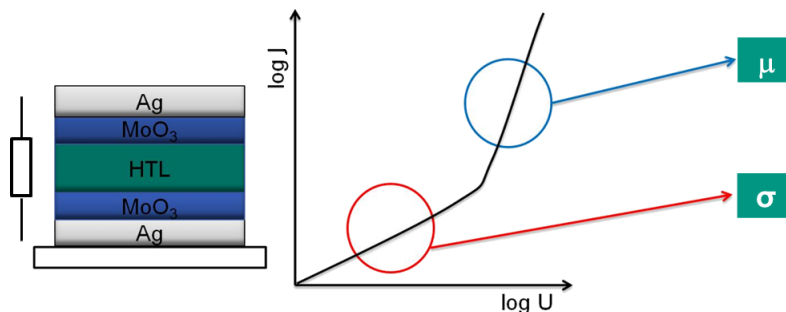


**Figure 4.2.** Device architecture and typical J-V curve of a monopolar device. The hole transport layer (HTL) is sandwiched between two high-work function electrodes. The ohmic limit at low voltages allows the calculation of the conductivity  $\sigma$ . At higher voltages, space charges are formed in an organic semiconductor. This allows the calculation of the mobility  $\mu$ .

Monopolar devices commonly feature ohmic contacts for one type of charges (in this case holes), at the same time blocking opposite charge carriers. If a voltage is applied, holes will be injected into the device. If the same amount of holes are injected than removed at the other electrode, the current can be described by ohmic law:

$$J = \frac{V \cdot \sigma}{d \cdot A} \quad (4.3)$$

From the applied voltage (V), the layer thickness (d) and the measured current density (J) the conductivity ( $\sigma$ ) can be calculated. When applying higher voltages, the charges can not be removed as fast as they are injected. Then space charges are formed, building an additional electrical field. In this area, the mobility  $\mu$  can be calculated according to equation 4.4.

$$J = \frac{9}{8} \epsilon \cdot \mu \frac{V^2}{d^3} \quad (4.4)$$

$\epsilon$  is the dielectric constant of the organic semiconductor and d the film thickness. The mobility  $\mu$  of organic semiconductors depends on the applied electric field. If considering the mobility as given in equation 4.5,[130]

$$J = \frac{9}{8} \epsilon \cdot \mu_0 \frac{V^2}{d^3} \exp(0.89\gamma \sqrt{\frac{U}{d}}) \quad (4.5)$$

$\mu_0$  is the mobility without any electrical field and  $\gamma$  is a field coefficient which can be estimated from the measured curve. The field dependent mobility can be calculated by[131]

$$\mu_E = \mu_0 \exp(\gamma \sqrt{E}) \quad (4.6)$$

#### 4.2.5.2. Charge extraction by linear increasing voltage

In CELIV devices, hole transport layers (HTLs) are incorporated in a diode-like setup where the current only flows in one direction. If a linear increasing voltage is applied in reverse-bias, this diode works like a capacitor which is charged. If additional charges exist in the characterized material, e.g. due to doping, an additional curve on top of the usual rectangular response of the capacitor can be measured. The resulting curve is shown in figure 4.3. If no additional charges are present, as in the undoped materials, charges can be injected by applying an offset voltage in forward direction which can be extracted afterwards.

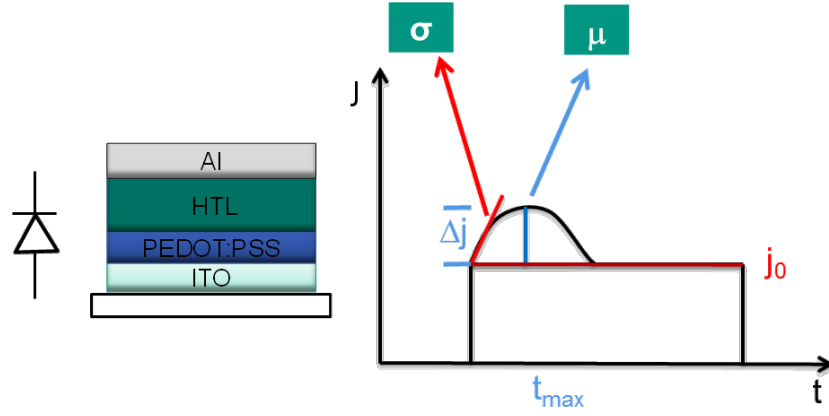


**Figure 4.3.** Device architecture and typical J-t curve of a CELIV device. The initial slope allows the calculation of the conductivity. The time of the maximum current density allows for calculating the mobility.

The initial slope of the curve onto the rectangular curve of the displacement current allows the calculation of the conductivity according to equation 4.7.

$$\sigma = \int_{t=0}^t \epsilon \frac{d \frac{j(t)}{j_0}}{dt} \quad (4.7)$$

Here,  $\epsilon$  is the dielectric constant of the material and  $j_0$  is the displacement current. If the conductivity of the material is high enough, so that the maximum of the additional curve can be measured, also the mobility can be calculated.[132]

$$\mu = \frac{2d^2}{3t_{max}^2 \cdot V' (1 + 0.36 \frac{\Delta j}{j_0})} \quad (4.8)$$

Where  $d$  is the layer thickness,  $t_{max}$  is the time when the maximum current is reached,  $V'$  is the slope of the voltage ramp and  $\Delta j$  is the difference between the maximum current and the displacement current.

#### 4.2.6. Layer integrity

To gain insight if the applied layers get intermixed during the processing, time-of-flight secondary ion mass spectroscopy (ToF-SIMS) measurements have been implemented. Diffusion of dopants has been analyzed by impedance spectroscopy.

##### 4.2.6.1. Time-of-flight secondary ion mass spectroscopy

A beam of highly energetically ions is used to eject secondary ions from the sample surface. These are separated in positive and negative ions by a massfilter and detected by a time of flight mass spectrometer. Light-weight ions are faster than heavy ions, and their mass can be calculated from their transit time to the detector.

#### 4.2.6.2. Impedance spectroscopy

In impedance spectroscopy, the current response of the sample to an alternating voltage at different frequencies ( $f = \frac{\omega}{2\pi}$ ) is measured. As in Ohms law, the impedance  $Z$  relates the applied voltage  $V$  to the measured current  $I$ . The following theoretical models are only valid in the regime of linear relation between  $V$  and  $I$ . To account for time dependent behavior of  $V$ ,  $I$  and  $Z$  all values are commonly represented in the frequency regime (Laplace transformation of the measured data).

If samples comprise single dielectric layers between two electrodes, the following simplified model applies. Here,  $\omega$  is the circular frequency,  $R$  the resistance and  $C$  the capacity of the dielectric layer between the electrodes.

$$Z = \frac{R}{1 + i \cdot \omega \cdot R \cdot C} \quad (4.9)$$

The real part which is equivalent to the ratio of the amplitudes of the voltage and the current signal, provides information about energy losses in the measured medium due to the reorientation of charged or polarized moieties in the induced electric field. The imaginary part results from the phase shift of voltage and current due to the storage of energy by loading the capacitance.

Due to a simplified relation between impedance and dielectric constant (see equation 4.10), it is possible to measure dielectric losses due to the polarizing of molecules.[133]

$$\epsilon = \frac{1}{j \cdot \omega \cdot C_0 \cdot Z} = \frac{C}{C_0} \cdot \frac{-j}{\omega \cdot C_0 \cdot R} \cdot \omega \cdot R \cdot C \quad (4.10)$$

$C_0$  is the capacitance of the sample except the investigated dielectric layer ( $\epsilon = 1$  assumed). If absolute comparison is necessary, it can be determined by Maxwell Simulation software.  $C_0$  is just a constant factor and does not influence the shape of frequency dependent impedance features. In relative comparisons it can be ignored and  $C$  can be derived in units of  $C_0$ .

At high frequencies (100 GHz - 100 PHz), ionic and electronic processes take place, whereas at lower frequencies (1 kHz - 1 GHz), molecules and dipoles orient themselves in the electric field. At frequencies below 1 kHz interface and space charge processes can be observed (see figure 4.4).

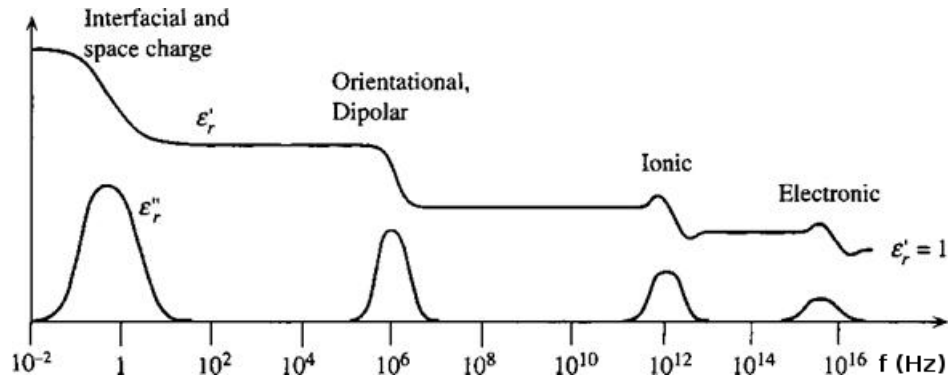


**Figure 4.4.** Real and imaginary part of the dielectric constant plotted against frequency. In different frequency regimes different electronic processes can be observed.[134]

Due to the applied alternating voltage, the electric field in the sample changes permanently with different frequencies of the voltage. Dipoles in the material, e.g. ionized molecules created by doping, respond to the electric field until the changes are too fast to follow. The reorientation consumes energy which is called dielectric loss.



# 5 | p-Doping by employing strong organic acceptors, processed from solution

Organic optoelectronic devices generally comprise an active layer between two electrodes.\* Voltage losses can be prevented by implementing charge carrier extraction in (OSC) or injection in (OLED) layers. To ensure ohmic contacts between active layer and electrodes, typically, electrically doped interlayers are introduced. Additionally, in multilayer devices it is crucial that the applied layers are not dissolved upon deposition of the next layer.

In this chapter, p-doping of different matrices processed from solution is investigated. Therefore, different matrices (low-molecular weight materials, polymers with pending functional groups and crosslinkable polymers with pending functional groups) are p-doped by two commercially available dopants. In the first part, the influence of the polymerization on the doping is studied. In the second part, the influence of the additional crosslinkable group and the crosslinking conditions is investigated.

## 5.1. Selection of hole transport materials and suitable dopants

As described above the details of the doping process are discussed controversially. However, in both suggested models, dopants with a LUMO energetically lower than the HOMO of the hole transport materials are required. This is taken into account when choosing materials.

---

\*Parts of the following section are reprinted (and adapted) from T. Schneider, F. Limberg, K. Yao, A. Armin, N. Jürgensen, J. Czolk, P. Friederich, W. Wenzel, J. Behrends, H. Krüger, A. Colsmann, submitted to *J. Mater. Chem. A* **2016** with permission of the Royal Society of Chemistry. T. Schneider designed and conducted all experiments unless otherwise stated and wrote the manuscript. F. Limberg synthesized the analyzed polymers, K. Yao remeasured the EPR measurements, N. Jürgensen measured parts of the MIS-CELIV samples. A. Armin helped with the discussions regarding charge transport and transfer. J. Czolk made pre-tests for MIS-CELIV measurements of the doped films and helped with discussions. P. Friederich and W. Wenzel developed the simulation code and did simulations on the energy level of MTDATA and the dopants. J. Behrends helped with discussions regarding EPR. H. Krüger helped to develop suitable polymers. A. Colsmann motivated and supervised the project and contributed to scientific discussions.

### 5.1.1. Hole transport materials

MTDATA and TPD are chosen as hole transport materials, due to their numerous applications in organic light emitting diodes as doped hole injection layers. [27, 28, 30] The group of Dr. Krüger from the Fraunhofer Institute for Applied Polymer Research (IAP) synthesized side-chain polymers based on a polystyrene backbone and MTDATA or TPD moieties as side-chains with and without 1-alkynyl ether as a pending thermally crosslinkable group.[55, 135] The structures of the investigated matrices are shown in figure 5.1. Thermal crosslinking is the method of choice in this work, because photo-crosslinking is difficult to handle, e.g. in organic solar cells due to the broad absorption spectrum of the absorber materials. Either the absorber absorbs light in the crosslinking wavelength regime or the crosslinking energy lies in the UV and thus can damage the organic layers.

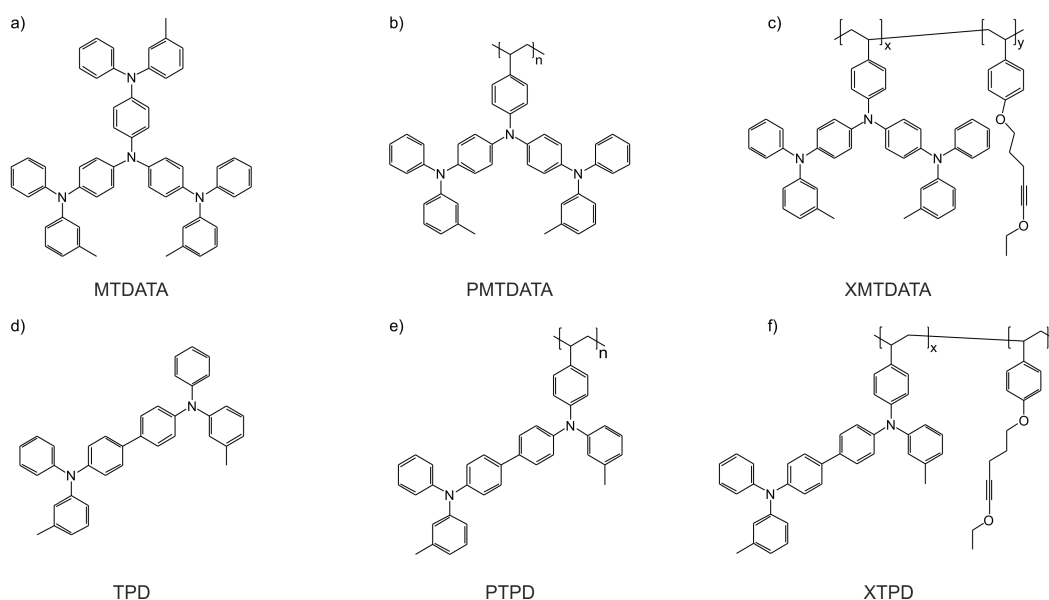


**Figure 5.1.** Chemical structures of the investigated hole transport materials. a) 4,4',4''-tris[phenyl(*m*-tolyl)amino]triphenylamine (MTDATA), b) poly-[4-*N,N*-bis[4-(*N,N*-phenyl(*m*-tolyl)amino]phenylamino)vinylphenyl] (PMTDATA), c) poly-[4-*N,N*-bis[4-(*N,N*-phenyl(*m*-tolyl)amino]phenylamino)vinylphenyl]-stat-1-((5-ethoxypent-4-yn-1-yl)oxy)-4-vinylbenzene (XMTDATA), d) *N,N*-bis(3-methylphenyl)-*N,N*-diphenylbenzidine (TPD), e) poly-[*N*-phenyl-*N,N'*-di(*m*-tolyl-*N'*-(4-vinylphenyl)biphenyl-4,4'-diamine)] (PTPD), f) poly-[*N*-phenyl-*N,N'*-di(*m*-tolyl-*N'*-(4-vinylphenyl)biphenyl-4,4'-diamine)-stat-1-((5-ethoxypent-4-yn-1-yl)oxy)-4-vinylbenzene (XTPD).

Two batches of PMTDATA are used which only slightly differ in their physical properties. The molecular weights are  $M_{w1} = 33.2$  kDa,  $M_{n1} = 18.9$  kDa and  $M_{w2} = 37.7$  kDa,  $M_{n2} = 23.4$  kDa resulting in a  $\bar{D}_M$  of 1.76 and 2.26 respectively. In contrast to conjugated backbone polymers, the electrical and chemical properties of side-chain polymers do not depend on the chain length.[55] Therefore, the small difference in the molecular weight does not influence the optoelectronic properties. The glass transition temperatures ( $T_g$ ) are similar, too, with 141°C and 151°C, respectively. These are much higher than the  $T_g$  of MTDATA (75°C).[136] This is a result of the connection of MTDATA moieties to the polymer. The HOMO levels are measured by PESA yielding between -5.20 eV and -5.22 eV. Thus the HOMO is shifted by around 0.1 eV compared to the low-molecular weight material. The origin of this shift might be caused by structural differences of the polymer. To attach the MTDATA to the polystyrene backbone, one of the tris[phenyl(*m*-tolyl)amino]-groups is substituted by a styrene moiety. The LUMO of -2.2 eV is calculated from the optical band gap by the Krüger-group. The corresponding crosslinkable version poly-[4-*N,N*-bis[4-(*N,N*-phenyl(*m*-tolyl)amino]phenylamino)vinylphenyl]-stat-1-((5-ethoxypent-4-yn-1-yl)oxy)-4-vinylbenzene (XMTDATA) contains 1-alkynyl ethers as thermal crosslinking groups. The ratio of MTDATA moieties to the crosslinker is approximately 4:1. The molecular weight ( $M_w = 33.5$  kDa,  $M_n = 18.9$  kDa,  $\bar{D}_M = 1.77$ ) is almost exactly the same as the first batch of PMTDATA. Because of the  $T_g = 160^\circ\text{C}$  after the crosslinking, a crosslinking is realized at 160°C after 30 min. The HOMO (-5.19 to -5.20 eV) and the LUMO (-2.2 eV) of the crosslinkable polymer is in accordance with the HOMO of the non-crosslinkable polymer.

PTPD shows a molecular weight of  $M_w = 34.7$  kDa,  $M_n = 12.1$  kDa ( $\bar{D}_M = 2.87$ ). The glass transition temperature is 162°C, much higher than the  $T_g$  of TPD (60°C) due to similar reasons as for PMTDATA.[137] The PESA measurements provide a HOMO energy of -5.42 to -5.44 eV, lying in a similar range as TPD (-5.40 to -5.44 eV) and matching ionization potentials measured for side-chain PTPD in the literature.[54] The LUMO of -2.3 eV is calculated from the optical bandgap. The TPD moieties are also copolymerized with the same 1-alkynyl ether crosslinking group to a crosslinkable side-chain-polymer poly-[*N*-phenyl-*N,N'*-Di(*m*-tolyl-*N'*-(4-vinylphenyl)bi-phenyl-4,4'-diamine)-stat-1-((5-ethoxypent-4-yn-1-yl)oxy)-4-vinylbenzene (XTPD) with a molecular weight of  $M_w = 28.0$  kDa,  $M_n = 14.7$  kDa ( $\bar{D}_M = 1.90$ ) which matches the molecular weight of PTPD. Due to the higher  $T_g$  (176°C) crosslinking requires 10 min annealing at 180°C. The HOMO energy of XTPD is -5.42 eV and the LUMO energy -2.3 eV, being in accordance with PTPD and TPD.

### 5.1.2. Suitable dopants for selected matrices

The HOMO levels of all chosen hole transport materials are located between -5.1 and -5.4 eV. Thus, suitable dopants must exhibit lower LUMO levels. Commercially available dopants that comply with this requirement, are F<sub>4</sub>TCNQ (LUMO: -5.4 eV)[115] and the stronger dopant HATCN<sub>6</sub> (LUMO: -6.0 eV).[138] Both are commonly applied in efficient vacuum processed OLEDs.[27, 29, 31] The chemical structures of the dopants and the energy levels of all used materials are shown in figure 5.2.

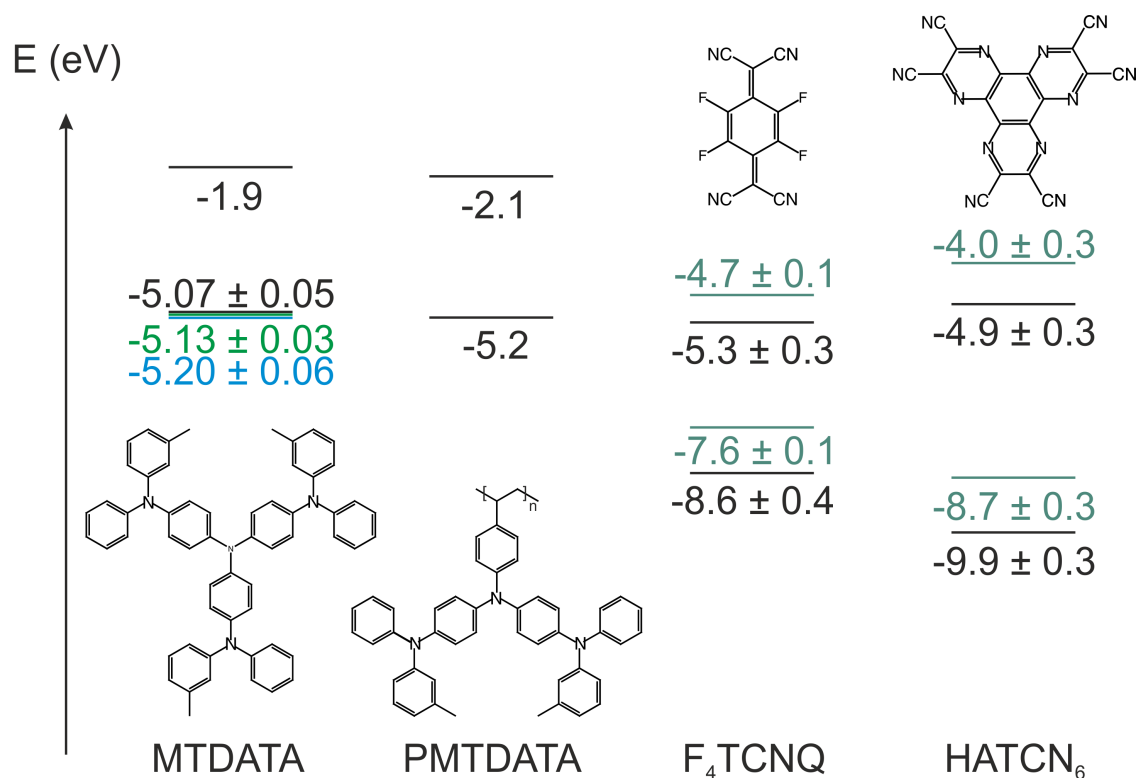


**Figure 5.2.** Energy levels of the used matrices and dopants. The LUMO levels of the dopants are energetically lower than or similar to the HOMO levels of the matrices. Chemical structures of the used dopants 2,3,5,6-tetrafluoro-7,7,8,8-tetracyanoquinodimethane (F<sub>4</sub>TCNQ) and 1,4,5,8,9,12-hexaazatriphenylene (HATCN<sub>6</sub>). The ionization potentials and electron affinities of MTDATA, F<sub>4</sub>TCNQ and HATCN<sub>6</sub> in pristine material (black) and mixed (matrix:dopant, 80:20, n:n) are computed by DFT. In the mixture (dopant mixed with MTDATA: cyan, MTDATA mixed with F<sub>4</sub>TCNQ: green, MTDATA mixed with HATCN<sub>6</sub>: blue) the energy levels of the dopants are shifted to higher energies and of MTDATA are shifted to lower energies.

In cooperation with the group of professor Wolfgang Wenzel DFT-calculations of the ionization energies and electron affinities of MTDATA, F<sub>4</sub>TCNQ and HATCN<sub>6</sub> were done by Pascal Friederich. These are calculated in case of pure materials and for a mixture of 80 mol% matrix and 20 mol% dopant considering only polarization effects and neglecting electron transfers.

The ionization potential of MTDATA is shifted to lower energies if surrounded by some dopant molecules due to their higher electronegativity. The  $E_I$  of MTDATA in a mixture comprising  $F_4TCNQ$  is shifted from 5.07 eV to 5.13 eV, whereas, in a mixture comprising  $HATCN_6$  it is shifted to 5.20 eV. Corresponding to that both the ionization energies and the electron affinities of the dopants are shifted to higher energies if surrounded by matrix molecules with a lower electronegativity. Due to this calculations  $F_4TCNQ$  is the stronger dopant compared to  $HATCN_6$ .

Li et al. recently pointed out that specifically  $F_4TCNQ$  may diffuse in the device at elevated temperatures due to its low vapor pressure.[139] In contrast  $HATCN_6$  molecules are larger hampering their mobility. Dielectric loss measurements are performed on thin-films of undoped or doped (10 mol%) MTDATA and the corresponding polymer with both dopants. The doping concentration is chosen based on the results of the conductivity measurements which will be introduced in chapter 5.2.3. Hereby the real and the imaginary part of the dielectric constant ( $\epsilon$ ) are measured versus frequency.

To gain information about the behavior of the dipoles created by doping, dielectric loss measurements of MTDATA and the corresponding polymer, undoped and doped with  $F_4TCNQ$  and  $HATCN_6$ , are performed between 100 Hz and 100 kHz. The resulting spectra are shown in figure 5.3.

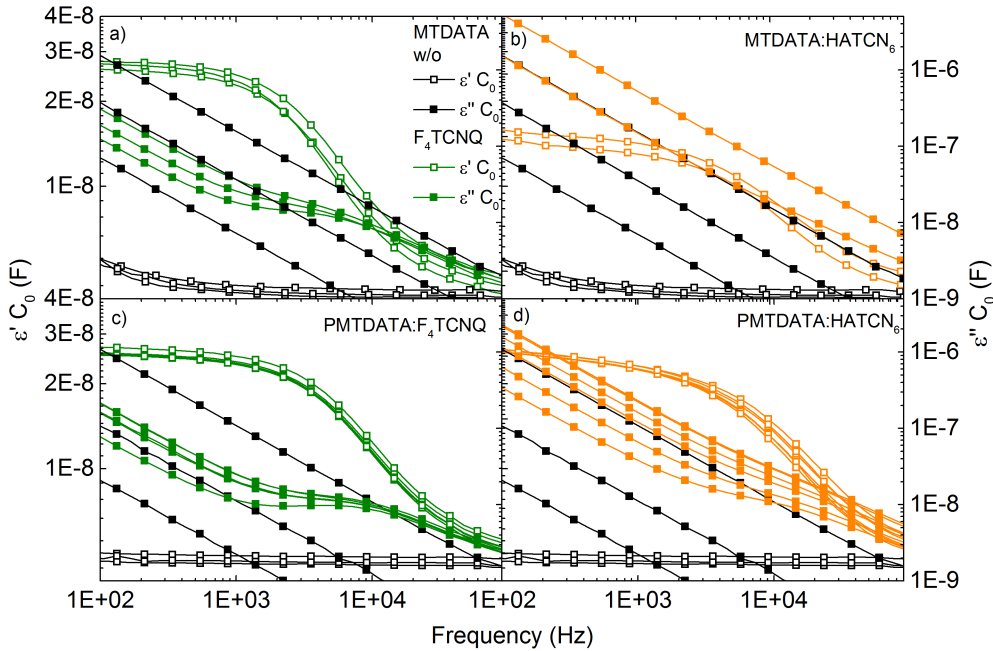


**Figure 5.3.** Dielectric loss measurements of undoped and doped (10 mol%) MTDATA and PMTDATA. Open symbols:  $\epsilon'$ , closed symbols:  $\epsilon''$  of (a) MTDATA undoped (black) and doped with  $F_4TCNQ$  (green), (b) MTDATA undoped and doped with  $HATCN_6$ , (c) PMTDATA undoped and doped with  $F_4TCNQ$ , (d) PMTDATA undoped and doped with  $HATCN_6$ . The real ( $\epsilon'$ ) and imaginary part ( $\epsilon''$ ) of the dielectric constant are scaled by  $C_0$  which is the capacitance of the devices for  $\epsilon = 1$ .

In all cases, the undoped matrices do not show any signal in this frequency regime in the real part of the dielectric constant. The curves of the imaginary part are straight lines. Their slope correlates to the conductivity of the dielectric layer between the electrodes. The shift between the different curves on the frequency axis originates from the slightly different conductivities of the materials due to small variations of the layer thickness. Upon doping, an increased  $\epsilon'$  for frequencies below 10 kHz is observed in all matrix-dopant combinations. In the imaginary part, a deviation from the original straight line is observed. Both indicate energy dissipation by orientation of dipoles in the electric field. Thus, dipoles are created upon doping. These dipoles orient in the electric field. Upon doping with  $F_4$ TCNQ (see figure 5.3 a and c), the deviations in the imaginary part are larger which indicates a stronger interaction between the dipoles and the applied electric field. This may be caused by the different sizes of the dopant molecules. A slight shift to higher frequencies is observed for PMTDATA (see figure 5.3 c and d) in comparison to MTDATA (see figure 5.3 a and b). This indicates a slightly different interaction between the oriented dipoles and the matrix materials.

Due to the measured effects in impedance spectroscopy upon doping, the effect of doping on the matrix materials was investigated by different methods. The electron transfer from the HOMO level of the matrix molecules to the LUMO of the dopant becomes visible in UV-vis-NIR spectrometry and photoelectron yield spectroscopy in air (PESA). More specifically, in UV-vis-NIR spectrometry, the transfer of the electrons from the new polaronic states back to the HOMO of the matrix molecules can be observed. PESA on the other hand allows measurements of the shift of the HOMO level due to electron depletion. The determination of the energy levels in air should not lead to unintentional oxidation of the molecules by ambient oxygen and subsequent changes of the energy levels due to the deep HOMOs of the matrices.

### 5.1.3. Optimization of doping concentration for characterization

As known from the literature, in comparison to vacuum processing, solution processed films may need a higher doping concentration before any effect is visible.[46] At first both methods are evaluated with a known matrix-dopant combination exhibiting different doping concentrations. MTDATA: $F_4$ TCNQ is a well known matrix-dopant combination, extensively studied in the literature.[24, 140]  $F_4$ TCNQ, as the weaker dopant, is chosen to optimize the doping concentration. Therefore, MTDATA films doped with 0, 5, 10, 15 and 20 mol% of  $F_4$ TCNQ are processed from solution.

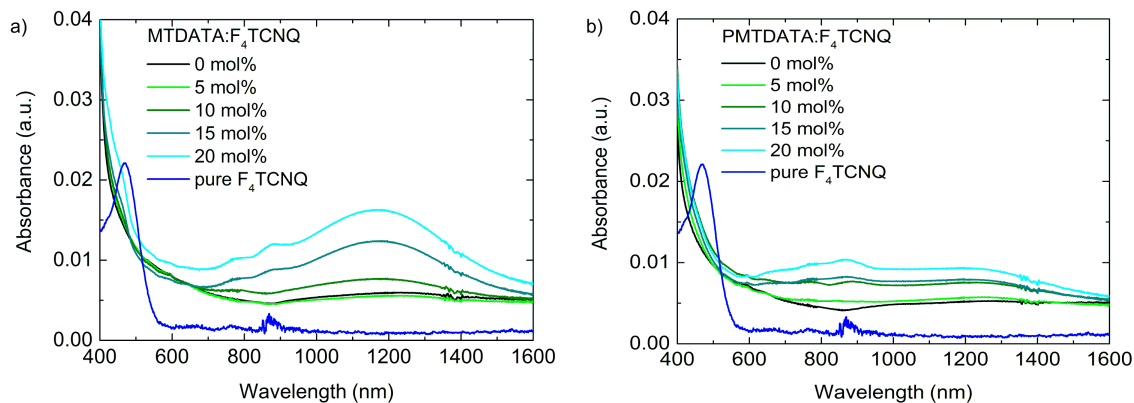


**Figure 5.4.** UV-vis-NIR-spectra of MTDATA and PMTDATA doped with different amount of  $F_4TCNQ$ . An additional absorption band between 600 and 1600 nm appears, increasing with increasing doping concentration.

The excitation of electrons back into the HOMO of the matrix can be observed in figure 5.4 if the doping concentrations exceeds 5 mol%. At these concentrations an additional absorption band appears between 600 and 800 nm which cannot be observed in the spectra of the neat materials. Towards higher concentration this absorption band becomes more pronounced. At doping concentrations of 5 mol% no significant difference to the curve of the undoped matrices can be observed.

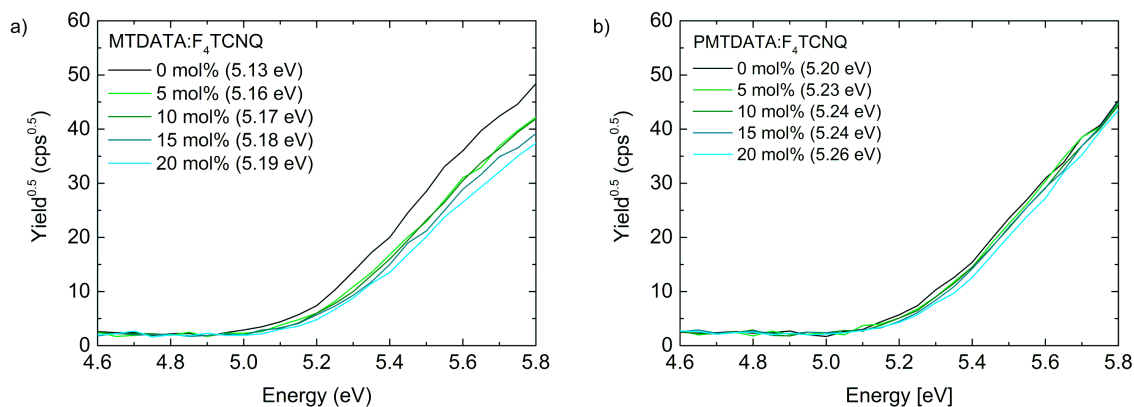


**Figure 5.5.** PESA measurements of MTDATA and PMTDATA doped with different amounts of  $F_4TCNQ$ . A small shift to lower yield and a decrease of the ionization potential towards increasing doping concentrations can be observed.

Using PESA the ionization potential of materials can be determined. In case of organic compounds, the ionization potential corresponds to the HOMO level. Therefore, the HOMO levels are measured by PESA at the same doping concentrations. In figure 5.5, MTDATA and its corresponding side-chain polymer show a small shift to lower yields at increasing  $F_4TCNQ$  concentrations. Due to the electron transfer from the HOMO the hole transport materials are positively charged. Therefore, more energy is required to eject electrons from the positive matrix. The shift of the ionization potential can be explained by this depletion of the HOMO level upon doping.

Both shifts are rather small especially in case of the spectra of the polymer. To facilitate all further experiments, the highest dopant concentration (20 mol%) is chosen.

## 5.2. Comparison of *p*-doping of polymers and low-molecular weight molecules

After choosing suitable materials for *p*-doped hole injection layers, the influence of the polymerization on the doping is investigated. Therefore, both the low-molecular weight materials and the corresponding side-chain polymers are doped with F<sub>4</sub>TCNQ and HATCN<sub>6</sub>, respectively. There is no single method to prove doping. Only the combination of different methods enables to verify doping. Therefore, the doping process and doping efficiencies are characterized with different methods and the results are compared.

The depletion of the HOMO level of the matrices due to the electron transfer from the matrix to the dopant, is analyzed by PESA. UV-vis-NIR spectrometry is used to investigate the transfer of electrons back to the matrices. Further investigation of the doping mechanism and its efficiency are carried out by EPR measurements. Before the implementation in OLEDs the electrical properties are characterized by hole-only devices and MIS-CELIV measurements. Furthermore, the surface structure of the films is studied by AFM.

### 5.2.1. Shift of the Homo energy due to *p*-doping

As *p*-doping leads to electron depletion of the HOMOs of the matrices, the ionization potential  $E_I$  is shifted to lower energies. Therefore, PESA measurements are carried out on doped and undoped thin-films of MTDATA and the corresponding polymer. The respective measurement results are depicted in figure 5.6.

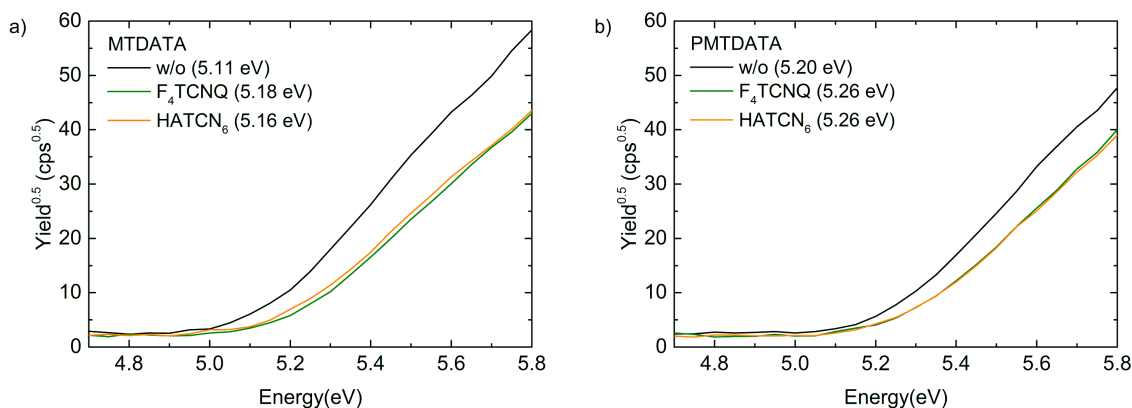


**Figure 5.6.** Photoelectron yield of undoped and doped (20 mol%) MTDATA and PMTDATA, measured by PESA. The shift of the ionization potential to lower energies by approximately  $0.07 \pm 0.02$  eV indicates an electron deficiency on the matrices.

In case of undoped MTDATA and PMTDATA, an  $E_I$  of 5.11 eV and 5.20 eV is found. A small shift of the ionization potential of the doped matrices in comparison to the undoped materials towards higher energies,  $\Delta E_I = (0.07 \pm 0.02)$  eV for MTDATA and



$\Delta E_I = (0.06 \pm 0.02)$  eV for PMTDATA is observed. This can be attributed to the electron depletion of the HOMO of the host. At the same time, a small decrease of the photo electron yield is observed which may also reflect the depletion of the HOMO due to charge carrier transfer to the dopant, being also in accordance with the DFT calculations and earlier studies.[141] Similar results are found for both matrices which indicates no significant difference between the molecular MTDATA and the polymer PMTDATA.

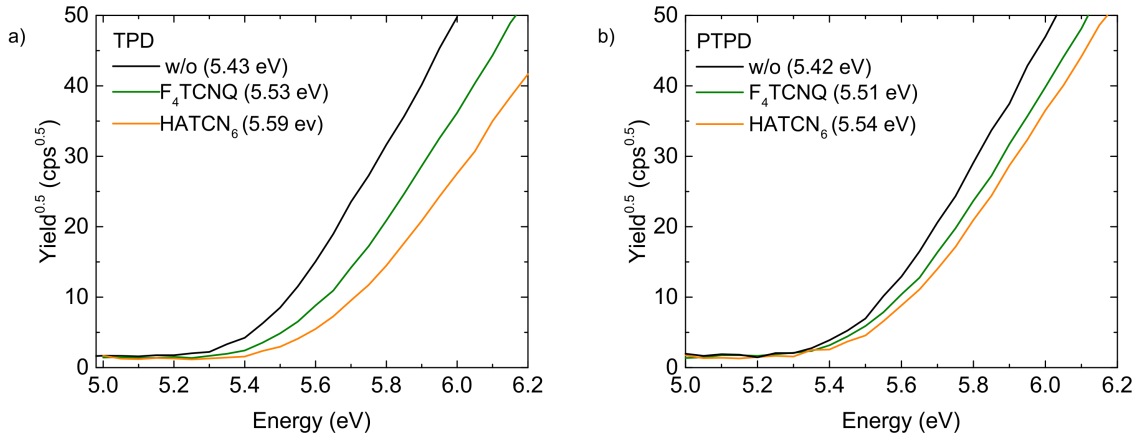


**Figure 5.7.** Photoelectron yield of undoped and doped (20 mol%) TPD and PTPD, measured by PESA. The shift of the ionization potential to lower energies indicates an electron deficiency on the matrices.

The ionization potentials of TPD ( $E_I = 5.43$  eV) and its corresponding side-chain polymer ( $E_I = 5.42$  eV) shown in figure 5.7 are slightly higher than the ionization potentials of MTDATA ( $E_I = 5.11$  eV) and PMTDATA ( $E_I = 5.20$  eV). In this system, doping also results in a shift towards higher energies. Doping with  $F_4TCNQ$  leads to a shift of  $\Delta E_I = (0.10 \pm 0.02)$  eV (TPD) and  $\Delta E_I = (0.09 \pm 0.02)$  eV (PTPD). When using  $HATCN_6$  instead, the shift is even larger ( $\Delta E_I = (0.16 \pm 0.02)$  eV for TPD and  $\Delta E_I = (0.12 \pm 0.02)$  for PTPD). The increasing ionization energy due to doping is in accordance to the increase of the work function of TPD doped with different amounts of  $HATCN_6$  measured by Sims et al. using KPFM.[31] Similar to the measurements of MTDATA and PMTDATA (figure 5.6) in doped TPD and PTPD a decrease of the slope of the photo electron yield is observed.

For all studied matrix-dopant systems, a shift to higher ionization potentials and a decrease in the slope of the curves upon doping is observed. The similarity of the results of the low-molecular weight and the polymer matrices indicates no detrimental effects on the doping when using polymers.

## 5.2.2. Electronic states and doping efficiencies

### 5.2.2.1. Characterization of the electron transfer by UV-vis-NIR spectrometry

The transitions between the polaronic states which are visible in the absorbance spectra of the spin coated films on glass, are depicted in figure 5.8. The measurements are performed on the same doped and undoped thin-films that are used for PESA measurements before.

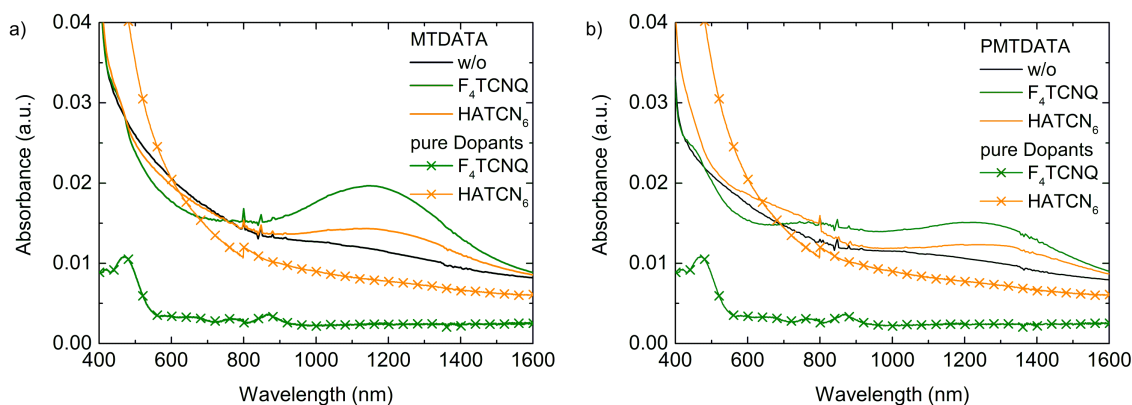


**Figure 5.8.** UV-vis-NIR absorption spectra of the undoped and doped (20 mol%) matrices MTDATA and PMTDATA. Absorption bands between 800 and 1600 nm indicate the formation of new polaronic states upon doping.

The additional absorption bands in the near infrared (800 - 1600 nm) emerge upon *p*-doping of the low-molecular weight material and the corresponding side-chain polymer. Reference samples of undoped matrices or neat dopants do not show any absorption features in this wavelength regime. The emerging absorption band is most pronounced for MTDATA:F<sub>4</sub>TCNQ and decreases somewhat when using the host PMTDATA or the dopant HATCN<sub>6</sub> instead. This matches also the DFT calculations showing that HATCN<sub>6</sub> is the weaker dopant.

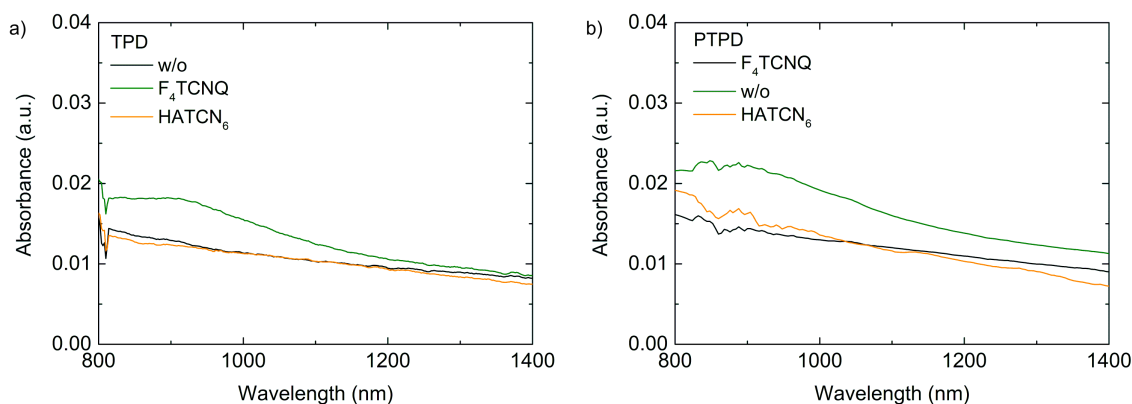


**Figure 5.9.** Near-infrared (NIR) absorption spectra of the undoped and doped (20 mol%) matrices TPD and PTPD. Only for the doping with F<sub>4</sub>TCNQ an additional absorption band between 800 and 950 nm indicates the formation of new polaronic states upon doping. Due to the change of the detector at 800 nm the curves had to be smoothed.

As shown in figure 5.9 using TPD and PTPD instead of MTDATA and PMTDATA the  $F_4$ TCNQ doped films show additional absorption bands which cannot be observed in the spectra of the pure matrices and pure dopants in this regime. These bands are narrower and show a lower intensity than the doped MTDATA and PMTDATA samples. Doping with HATCN<sub>6</sub> does not lead to visible additional absorption bands.

### 5.2.2.2. Measurement of the number of unpaired spins by EPR spectroscopy and calculation of doping efficiencies

Considering the trend in the PESA measurements and the additional absorption in NIR due to doping, a deeper insight in the charge carrier transfer in the doped systems is needed. Therefore, the number of unpaired electrons, that form upon charge carrier transfer, is determined in the different matrix-dopant systems by EPR. Hereby, a more quantitative insight into the doping mechanism is gained.

Spins of unpaired electrons align along an external magnetic field and the energetic states split into two states with different magnetic spin quantum number ( $m_s = \pm\frac{1}{2}$ ). Transitions between the two energy levels can be induced by resonant microwave absorption. In a typical cwEPR experiment, field modulation in combination with lock-in detection is used which leads to the typical derivative EPR line shape shown in figure 5.10.

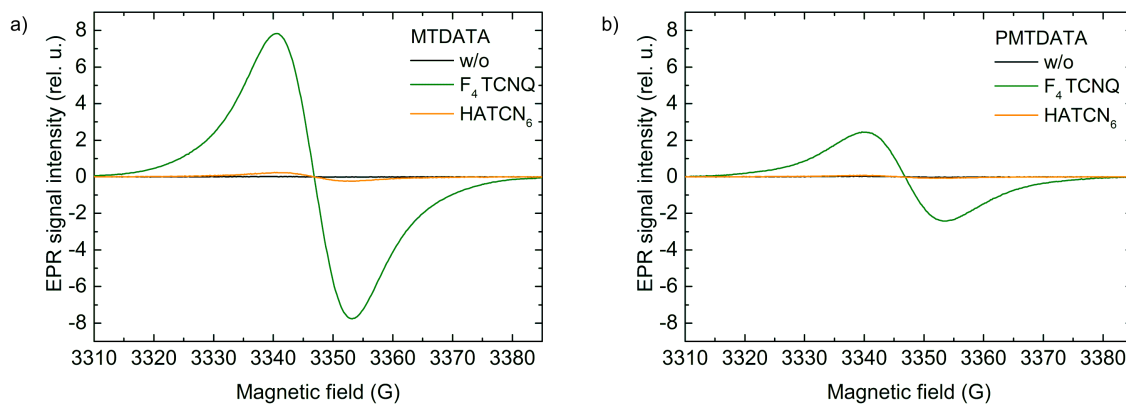


**Figure 5.10.** EPR spectra obtained from undoped and doped (20 mol%) MTDATA and PMTDATA. For undoped matrices (black line) almost no EPR signals are observed. Upon p-doping of MTDATA or PMTDATA with  $F_4$ TCNQ (green line), a strong EPR signal can be detected, indicating integer electron transfer to the dopant. Upon doping with HATCN<sub>6</sub> (orange line) an increased signal is observed, but significantly smaller than the signal of the  $F_4$ TCNQ doped matrices.

As shown in figure 5.10, the undoped molecular MTDATA and the polymer PMTDATA exhibit almost no signatures of unpaired electrons. Upon doping with  $F_4$ TCNQ, the EPR experiments yield a strong signature of unpaired spins and hence electrical doping. This

signal indicates an integer charge transfer from the matrix to the dopant. A similar signature is also visible if employing the dopant HATCN<sub>6</sub>. However, the latter signal is significantly reduced which is in accordance to the calculated higher electron affinities by DFT.

To gain quantitative information of the electron transfer yield, the absolute number of spins in the samples is calculated by double-integration of the EPR signal and comparison to a 4-hydroxy-TEMPO-reference sample with a known number of spins. All measured data and the derived electrical material properties are summarized in Table 5.1.

**Table 5.1.** Number of spins per volume and doping efficiency of the matrix-dopant (20 mol%) combinations as calculated from the EPR measurements. The doping efficiency is calculated based on the formation of polarons.

	Total amount of spins	Spin concentration (cm <sup>-3</sup> )	Doping efficiency (%)
MTDATA	$9 \times 10^{11}$	$4 \times 10^{15}$	0
MTDATA:F <sub>4</sub> TCNQ	$2 \times 10^{15}$	$7 \times 10^{18}$	7
MTDATA:HATCN <sub>6</sub>	$9 \times 10^{13}$	$4 \times 10^{17}$	0.3
PMTDATA	$2 \times 10^{12}$	$7 \times 10^{15}$	0
PMTDATA:F <sub>4</sub> TCNQ	$8 \times 10^{14}$	$3 \times 10^{18}$	2
PMTDATA:HATCN <sub>6</sub>	$1 \times 10^{14}$	$5 \times 10^{17}$	0.3

Spin concentrations are calculated by dividing the total amount of measured spins by the sample volume. From the spin concentration and the density of the matrix, the doping efficiency (e.g., the fraction of p-doped matrix molecules) is determined, further taking into account the paired formation of spins upon charge carrier transfer from the matrix to the dopant.

Upon p-doping of MTDATA and PMTDATA with F<sub>4</sub>TCNQ, a substantial increase of three orders of magnitude in the spin concentrations is found from  $4 \times 10^{15}$  cm<sup>-3</sup> to  $7 \times 10^{18}$  cm<sup>-3</sup> and from  $7 \times 10^{15}$  cm<sup>-3</sup> to  $3 \times 10^{18}$  cm<sup>-3</sup>, respectively. This is well in accordance with the spin concentrations reported in earlier work on vacuum processed MTDATA:F<sub>4</sub>TCNQ ( $2 \times 10^{18}$  cm<sup>-3</sup>).<sup>[142]</sup> However, if replacing the dopant F<sub>4</sub>TCNQ with HATCN<sub>6</sub>, a somewhat lower increase of two orders of magnitude in the spin concentration is observed, yielding  $4 \times 10^{17}$  cm<sup>-3</sup> (MTDATA:HATCN<sub>6</sub>) or  $5 \times 10^{17}$  cm<sup>-3</sup> (PMTDATA:HATCN<sub>6</sub>), respectively.

It is important to point out, that the spin concentration in neat F<sub>4</sub>TCNQ and HATCN<sub>6</sub>, deposited from THF solution, converted to the used amount in the doped samples, is two to three orders of magnitude lower. Thus electrical doping of the matrix molecule rather than complex formation of residual THF and F<sub>4</sub>TCNQ or HATCN<sub>6</sub> is observed.

Based on the measured spin concentrations, doping efficiencies (percentage of doped host molecules) can be calculated, resulting in 7% for MTDATA:F<sub>4</sub>TCNQ, 2% for PMTDATA:F<sub>4</sub>TCNQ, and 0.3% for MTDATA:HATCN<sub>6</sub> and PMTDATA:HATCN<sub>6</sub>. The lower spin concentrations and doping efficiencies of HATCN<sub>6</sub> also matches the calculated the higher electron affinities. Most importantly, the doping efficiency of both matrices, the molecular MTDATA and the polymer PMTDATA, are comparable.

The same experiments are performed on doped and undoped TPD and similar tendencies are observed.

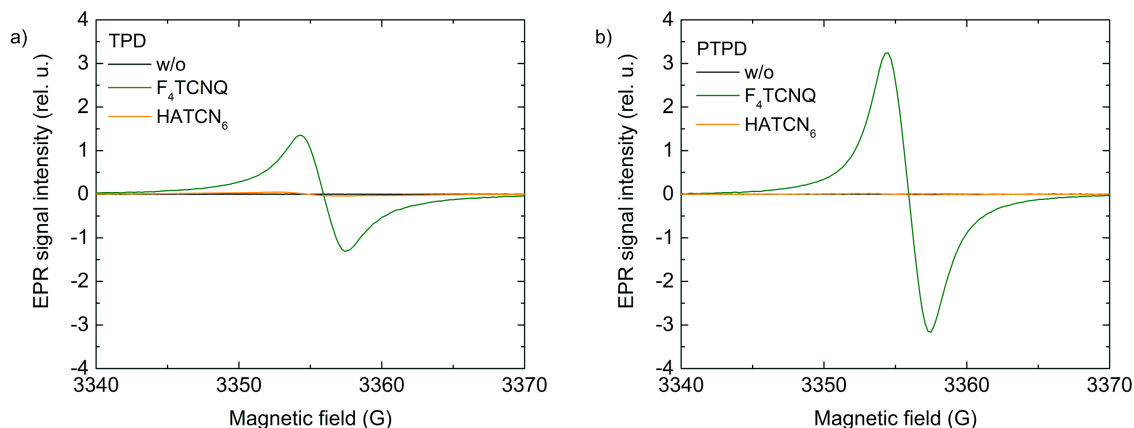


**Figure 5.11.** EPR spectra obtained from undoped and doped (20 mol%) TPD and PTPD. For undoped TPD and PTPD (black line), only weak EPR signals are observed. Upon *p*-doping of TPD or PTPD with F<sub>4</sub>TCNQ (green line), a strong EPR signal can be detected, indicating integer electron transfer to the dopant. Upon doping with HATCN<sub>6</sub> (orange line) an increased signal is observed, but significantly smaller.

For neat TPD and PTPD, figure 5.11 also exhibits only weak signatures of unpaired electrons. Upon doping with F<sub>4</sub>TCNQ, the EPR experiments yield a strong signature of unpaired spins and hence electrical doping, indicating integer electron transfer to the dopant. When employing the dopant HATCN<sub>6</sub>, a similar but significantly reduced signal is observed. All measured data and the derived electrical material properties are summarized in Table 5.2.

**Table 5.2.** Number of spins per volume and doping efficiencies of the matrix-dopant (20 mol%) combinations as calculated from EPR measurements. The doping efficiency is calculated based on the formation of polarons.

	Total amount of spins	Spin concentration ( $\text{cm}^{-3}$ )	Doping efficiency (%)
TPD	$6 \times 10^{11}$	$2 \times 10^{15}$	0
TPD:F <sub>4</sub> TCNQ	$8 \times 10^{14}$	$3 \times 10^{18}$	1
TPD:HATCN <sub>6</sub>	$5 \times 10^{13}$	$2 \times 10^{17}$	0.06
PTPD	$3 \times 10^{11}$	$1 \times 10^{15}$	0
PTPD:F <sub>4</sub> TCNQ	$9 \times 10^{14}$	$4 \times 10^{18}$	2
PTPD:HATCN <sub>6</sub>	$1 \times 10^{13}$	$4 \times 10^{16}$	0.02

The measured amount of spins of the undoped materials are within the resolution limit of the employed EPR setup yielding  $6 \times 10^{11}$  for TPD and  $3 \times 10^{11}$  for PTPD spins in the studied samples and the corresponding spin concentrations of  $2 \times 10^{15} \text{ cm}^{-3}$  (TPD) and  $1 \times 10^{15} \text{ cm}^{-3}$  (PTPD) within the resolution limit of the employed EPR setup. Upon doping with F<sub>4</sub>TCNQ, the spin concentration increased for both matrices by three orders of magnitude to  $3 \times 10^{18} \text{ cm}^{-3}$  and  $4 \times 10^{18} \text{ cm}^{-3}$ , respectively. This is one order of magnitude higher than the spin concentration of TPD:F<sub>4</sub>TCNQ reported in the literature[143] The fact that unpaired spins are measurable indicates that in this system an integer charge transfer occurs as well. If using HATCN<sub>6</sub> instead, the spin concentrations of TPD:HATCN<sub>6</sub> is one order of magnitude ( $2 \times 10^{17} \text{ cm}^{-3}$ ) and of PTPD:HATCN<sub>6</sub> two orders of magnitude ( $4 \times 10^{16} \text{ cm}^{-3}$ ) lower than for doping with F<sub>4</sub>TCNQ due to its lower acceptor strength.

The respective doping efficiencies are 1% for TPD:F<sub>4</sub>TCNQ, 2% for PTPD:F<sub>4</sub>TCNQ, 0.06% for TPD:HATCN<sub>6</sub> and 0.02% for PTPD:HATCN<sub>6</sub>. If doping with F<sub>4</sub>TCNQ, no significant difference is observed between the low-molecular weight material and the side-chain polymer. If doping with HATCN<sub>6</sub>, the difference is one order of magnitude higher for TPD than for PTPD. Similar to the doping of MTDATA and PMTDATA with HATCN<sub>6</sub>, in case of doping TPD and PTPD with HATCN<sub>6</sub>, the doping efficiencies and spin concentrations are lower than for doping with F<sub>4</sub>TCNQ.

The low-molecular weight TPD and the corresponding polymer PTPD yield similar results. Only the doping efficiencies of TPD and PTPD are slightly lower than for doping of MTDATA and PMTDATA which results from a slightly lower HOMO level of TPD and PTPD and therefore less energetic difference to the LUMO of the dopants.

### 5.2.3. Electrical properties

Electron depletion on the matrices and hence generation of equilibrium free holes are generally expected to enhance the conductivity of films. In this work, the conductivities of the films versus dopant concentration are determined utilizing MIS-CELIV (in the dark) and hole-only devices, meaning devices with the same electrode on both sides.

Using MIS-CELIV, the conductivities are determined from the initial slope of the equilibrium charge carrier extraction current according to the process described in the literature, not being sensitive to the device area and thickness.[132] Considering film thicknesses of 400-600 nm, the influence of any depletion zones at the electrodes is negligible.[144] Using hole-only devices, the hole current density  $J_\rho$  follows equation 5.1:

$$J_\rho = J_{\rho,\Omega} + J_{\rho,SCLC} = e \cdot \rho \cdot \mu \frac{U}{d} + \frac{9}{8} \epsilon_0 \cdot \epsilon_r \cdot \mu \frac{U^2}{d^3} \quad (5.1)$$

with the layer thickness  $d$ , the charge carrier mobility  $\mu$ , the equilibrium charge carrier density  $\rho$ , and the dielectric constant  $\epsilon_r$ . At low voltages, the Ohmic current density  $J_{\rho,\Omega}$  determines the monopolar device's response to an applied voltage. As the voltage increases, the hole-only devices are eventually driven into the space charge limited current (SCLC) regime. In case that  $J_{\rho,SCLC}$ , equation 5.1 dominates.[145] Accordingly, the conductivities

$$\sigma = \rho \cdot e \cdot \mu \quad (5.2)$$

were estimated in steady state conditions from the slope of the J-V curves at low voltages where the current density follows Ohm's law.[144, 145] Both, MTDATA and PMTDATA, are doped with different concentrations (0 – 15 mol%) of either dopant as depicted in Figure 5.12. In case of low doping concentration (1 mol%), the results of the hole-only devices are more reliable than the conductivities measured by MIS-CELIV as derived from the slope of the additional curve in MIS-CELIV measurements at low concentrations. In case of higher concentrations, the MIS-CELIV measurements are more reliable because injection of charges into the device is inhibited by the insulating  $\text{MgF}_2$  layer.

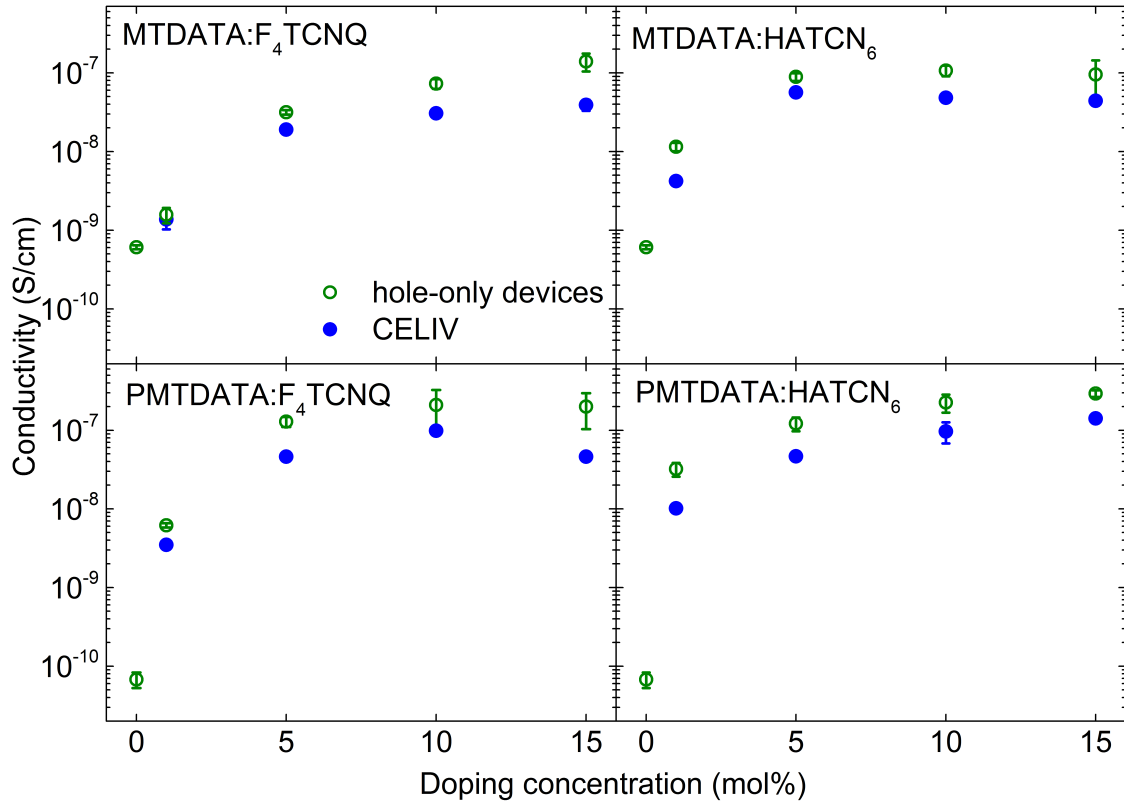


**Figure 5.12.** Conductivities of undoped and doped films as measured by MIS-CELIV (closed circles) and on hole-only devices (open circles), averaged over at least four samples. The conductivities improve with increasing doping concentration for all matrix-dopant combinations and saturate at around  $10^{-7}$  S/cm above a dopant concentration of about 10 mol%.

The conductivities measured with both methods are in good agreement which demonstrates the reliability of the experimental approaches. For undoped materials, the conductivities could only be measured by hole-only devices, because they do not provide additional charges which are crucial for the CELIV measurements.

The conductivity of undoped MTDATA ( $6 \times 10^{-10}$  S/cm) matches well the literature known conductivity of  $4 \times 10^{-10}$  S/cm that is extracted from bulk I-V data of vacuum deposited layers.[140] Even with a small amount of dopant (1 mol%) the conductivity is enhanced. With increasing doping concentration, the conductivities of all matrix-dopant combinations increase and saturate at around  $10^{-7}$  S/cm above a dopant concentration of 10 mol% which is again consistent with the conductivity of vacuum processed MTDATA thin-films doped with F<sub>4</sub>TCNQ.[142] An increase in the conductivity due to doping of more than two orders of magnitude is observed. Although undoped PMTDATA has a lower conductivity of  $2 \times 10^{-11}$  S/cm, similar conductivities can be achieved in the doped systems at comparable dopant concentrations.



The conductivities of TPD and PTPD doped at different concentrations (0 - 15 mol%) of  $F_4TCNQ$  and  $HATCN_6$  are measured with hole-only devices and MIS-CELIV likewise.

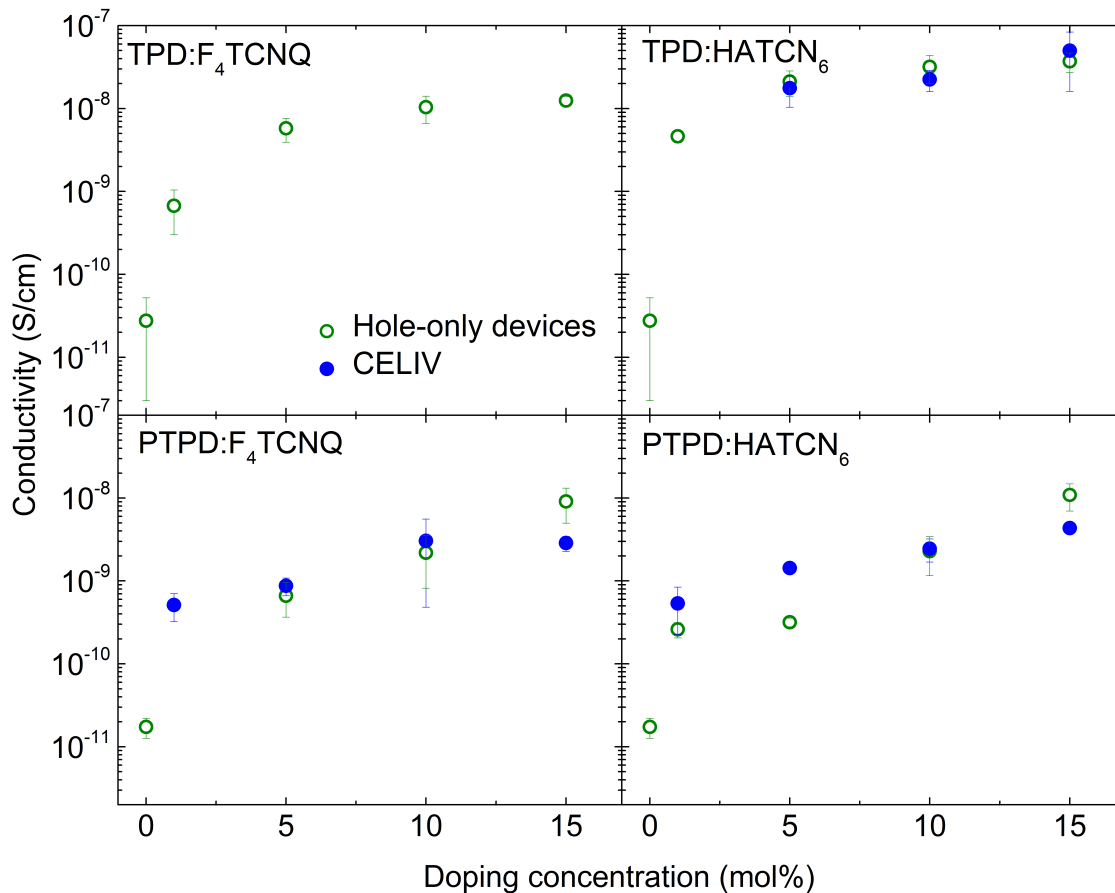


**Figure 5.13.** Conductivities of undoped and doped films as measured by MIS-CELIV (closed circles) and on hole-only devices (open circles), averaged over at least four samples. For TPD: $F_4TCNQ$  no additional charges upon doping could be measured by MIS-CELIV. In case of all other matrix-dopant combinations the conductivities improve with increasing doping concentration and saturate between  $10^{-7}$  and  $10^{-8}$  S/cm (TPD: $HATCN_6$ ) and between  $10^{-8}$  and  $10^{-9}$  S/cm (PTPD: $F_4TCNQ$ , PTPD: $HATCN_6$ ) above a dopant concentration of about 10 mol%.

The conductivities measured on hole-only devices show, in case of doped TPD, a similar trend as in case of doped MTDATA. In case of TPD: $F_4TCNQ$  no additional charges upon doping could be measured by MIS-CELIV and therefore no conductivities could be calculated. Because of the insulating layer in the MIS-CELIV-device and the fact that it can easily be recognized when charges are injected into the device, MIS-CELIV measurements are more trusted than the measurements of hole-only devices. Regarding the MIS-CELIV measurements, doping of TPD with  $F_4TCNQ$  is not successful, while other combinations of matrices and dopant are. The increased conductivity of TPD: $F_4TCNQ$  may result from shallow traps caused by the LUMO of  $F_4TCNQ$  slightly above the

HOMO of TPD. According to Murgatroyd et al., the current density increases more if traps are available due to the increasing field dependency of the mobility with the number of empty traps.[131] In case of the other doped matrices, the conductivities measured by MIS-CELIV are in a good accordance to the hole-only devices measurements. The conductivity of undoped TPD ( $10^{-11}$  S/cm) is slightly higher than the reported conductivity in the literature ( $10^{-12}$  S/cm)[146] which may be caused by different device architectures or measurement methods. The conductivities increase with increasing doping concentration and saturate, when measured with MIS-CELIV at a doping concentration of 10 mol% between  $10^{-7}$  and  $10^{-8}$  S/cm. This is in accordance with datas for TPD doped with  $F_4TCNQ$  reported in the literature.[146]

When doping the corresponding polymer, the conductivities increase with higher doping concentrations, too. But here they are around one order of magnitude lower than for the low-molecular weight material. They level between  $10^{-8}$  and  $10^{-9}$  S/cm at a doping concentration of 10 mol% for both dopants.

The conductivities of doped MTDATA, the corresponding polymer and TPD:HATCN<sub>6</sub> show similar conductivities of around  $10^{-7}$  S/cm. For doped PTPD it is only one order of magnitude lower. This underlines the suitability of the doped polymers as alternatives for low-molecular weight materials. No difference in the conductivity can be found when comparing the two dopants.

In addition to the promising results of increased conductivities due to doping, information about the mobility are of interest. Due to the injection of charge carriers from the aluminum electrode into the device at higher voltages for MTDATA and PMTDATA it is not possible to apply voltages high enough to reach the maximum of the additional part of the I-t curves without falsifying the results. Due to the superposition of the signal of the injected charges and the additional charges, the latter introduced by doping, it is not possible to differentiate the two signals. Thus no mobilities could be determined for doped and undoped MTDATA and the corresponding polymer.

In contrast, mobilities in doped and undoped TPD and PTPD are determined and shown in figure 5.14. Due to time constraints in this work, mobility measurements by MIS-CELIV were only realized for TPD:HATCN<sub>6</sub>. Based on the results of the conductivity measurements of TPD:HATCN<sub>6</sub>, it can be assumed that MIS-CELIV measurements would provide similar results like the shown hole-only devices.

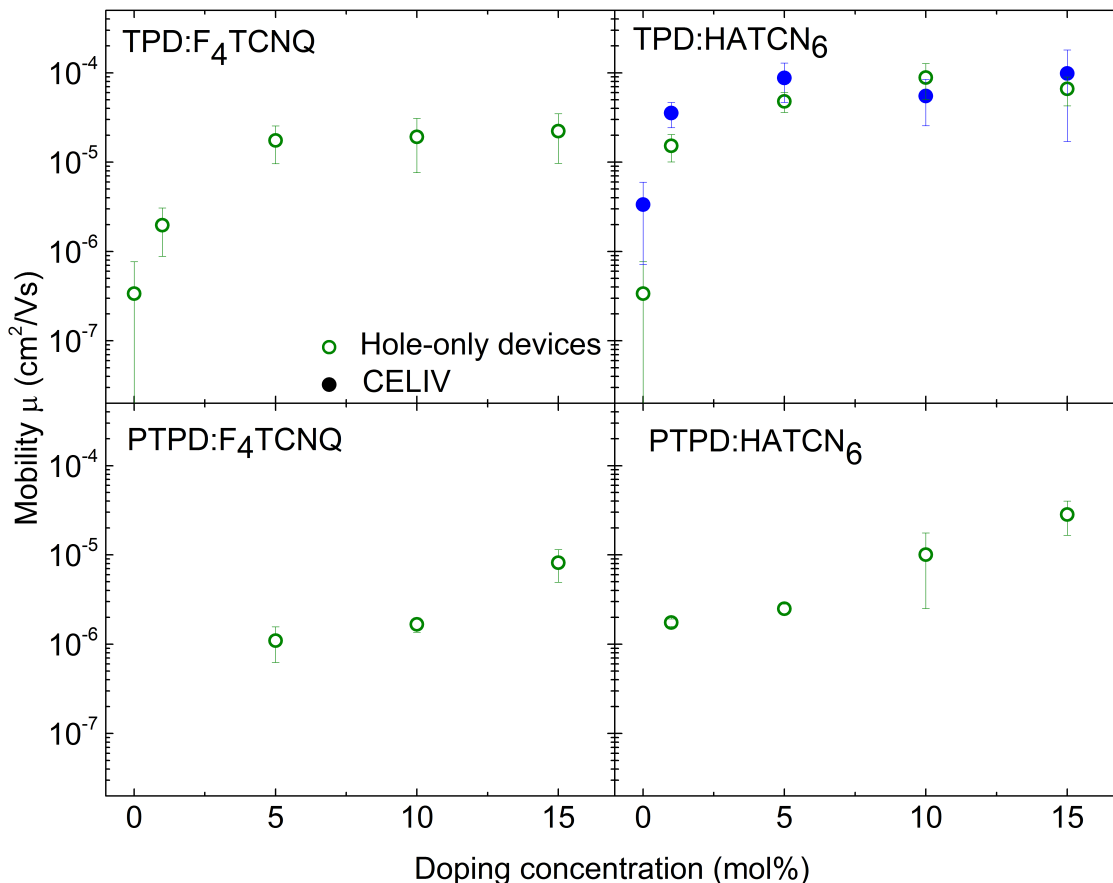


**Figure 5.14.** Mobilities of undoped and doped films as measured by MIS-CELIV (closed circles) and hole-only devices (open circles), averaged over at least four samples. For TPD:F<sub>4</sub>TCNQ no additional charges upon doping can be measured by MIS-CELIV. The mobility of TPD:HATCN<sub>6</sub> improves with increasing doping concentration from between 10<sup>-7</sup> and 10<sup>-6</sup> cm<sup>2</sup>/Vs to slightly below 10<sup>-4</sup> cm<sup>2</sup>/Vs. The mobilities measured by MIS-CELIV and hole-only devices match very nicely. In case of doped PTPD, the mobilities increase to 10<sup>-5</sup> cm<sup>2</sup>/Vs, but up to 15 mol% no saturation is observed.

As mentioned previously no additional charges can be measured in TPD:F<sub>4</sub>TCNQ by MIS-CELIV and thus no mobilities can be determined. The mobilities measured by hole-only devices may be caused by charge carrier transport in traps of the LUMO of F<sub>4</sub>TCNQ. The mobility of TPD:HATCN<sub>6</sub> increases from between 10<sup>-7</sup> and 10<sup>-6</sup> cm<sup>2</sup>/Vs due to doping and saturates at a doping concentration of 5 mol% at slightly below 10<sup>-4</sup> cm<sup>2</sup>/Vs. This is in accordance to data reported in the literature.[147] It is observed that the mobilities determined by MIS-CELIV measurements and from hole-only devices measured for TPD:HATCN<sub>6</sub> match nicely. In case of the corresponding polymer, the mobilities increase as well to 10<sup>-5</sup> cm<sup>2</sup>/Vs, with a similar trend as in case of the conductivities. No saturation is observed up to a doping concentration of 15 mol% and thus the optimal doping concentration is not reached for PTPD. Measurements at higher concentrations have not been carried out due to time constraints.

By EPR additional charges could be measured in TPD:F<sub>4</sub>TCNQ, that cannot be extracted concerning the MIS-CELIV measurements. An explanation might be that TPD tends to crystallize. To further investigate this, the surface topography of the doped and undoped films were analyzed by AFM.

#### 5.2.4. Investigation of film homogeneities

Before implementing the undoped and doped layers in organic electronic devices and to investigate the differences of TPD:F<sub>4</sub>TCNQ, compared to the other doped systems, their film homogeneities and the film conductivities are analyzed by AFM and peak-force-TUNA-AFM (PF-TUNA-AFM). The surfaces are shown in figure 5.15 - 5.19. The absolute datas of the measured currents cannot be compared between pictures, because the different layers are not on the same substrate, and by withdrawing the tip and engaging again to the surface, the state of the tip and the contact pressure can change. Thus the PF-TUNA-AFM measurements are only used to investigate the homogeneity of the films. In the bottom half of the picture a voltage is applied to measure the resulting currents.

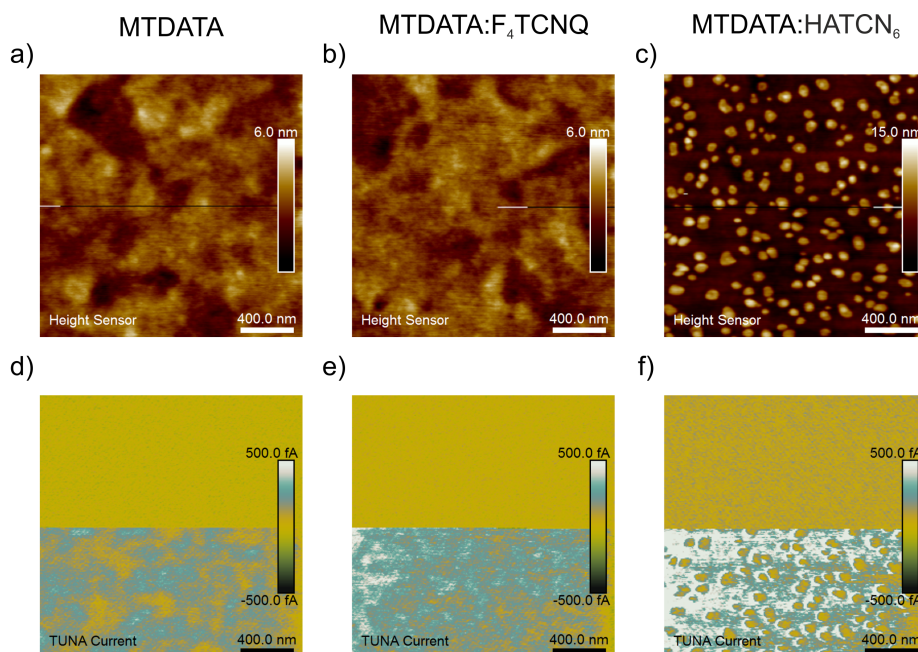


**Figure 5.15.** Film topography (first row) and current pictures (second row) of undoped and doped (10 mol%) MTDATA films. MTDATA and MTDATA:F<sub>4</sub>TCNQ films are very smooth and show homogeneous conductivity over the whole surface in the PF-TUNA-AFM micrographs. In MTDATA:HATCN<sub>6</sub> films, non-conductive agglomerates are observed which exhibit no defined structure. Thus they may predominantly consist of matrix molecules rather than dopant.

As depicted in figure 5.15 a, MTDATA forms a very smooth film. Due to the thin layer of around 30 nm, the surface of the ITO underneath is still visible. Even after doping with F<sub>4</sub>TCNQ (10 mol%), no changes in the surface roughness are observed (see figure 5.15 b). In the PF-TUNA-AFM micrographs, only weak currents of maximal 500 fA are measured which is near the measurement limit and thus may be noise. Nevertheless the images clearly show homogeneous conductivities over the whole film (see figure 5.15 d, e). Upon doping with HATCN<sub>6</sub> (10 mol%), agglomerates with a size of 100 nm and no defined structure are observed on the surface depicted in figure 5.15 c. In the corresponding PF-TUNA-AFM micrograph (figure 5.15 f), it is shown that these agglomerates are less conductive than the rest of the layer. This and the non-defined form of the agglomerates indicates that the agglomerates might be rather composed of MTDATA or a MTDATA:HATCN<sub>6</sub> mixture than of pure dopant due to a defined crystal structure and a higher conductivity of HATCN<sub>6</sub> crystals.[148] These agglomerates do not have influence on the conductivities of the films as shown in the hole-only devices and MIS-CELIV measurements.

All undoped and doped PMTDATA thin-films exhibit a smooth surface (see figure 5.16 a-c). In the current measurements, a high homogeneity in the conductivity of all films is observed as well (see figure 5.16 d-f). Thus no agglomerates hampering the doping are found which is in accordance to the previous characterization. Likewise, upon doping with HATCN<sub>6</sub>, no agglomerates are observed, showing the better film forming properties of the polymer compared to the low-molecular weight material.

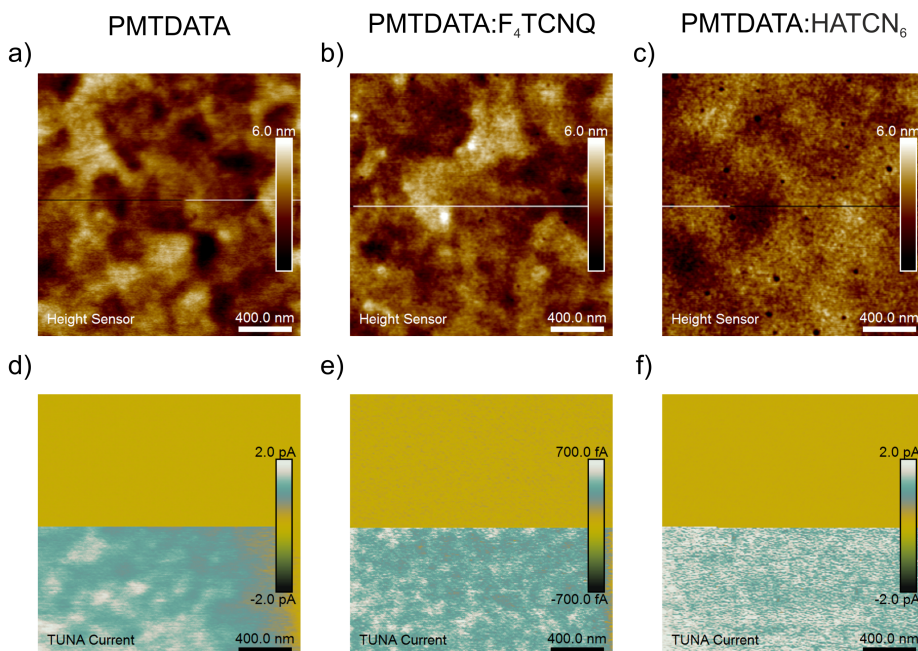


**Figure 5.16.** Topography (first row) and current pictures (second row) of undoped and doped (10 mol%) PMTDATA films. All films are very smooth and show homogeneous conductivity in the PF-TUNA-AFM micrograph.

The undoped and doped TPD and PTPD thin-films show similar properties. Due to the work function of the AFM tip between the Fermi energies of MTDATA and TPD, the current flows in opposite direction.

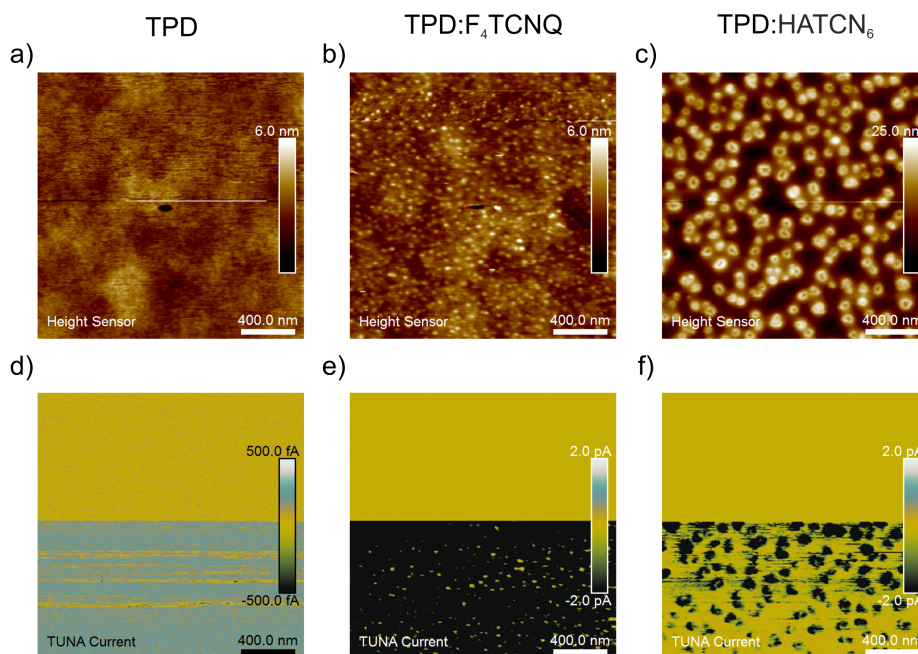


**Figure 5.17.** Topography (first row) and current pictures (second row) of undoped and doped (10 mol%) TPD films. The TPD film is smooth and the conductivity is homogeneous as visible in the PF-TUNA-AFM micrograph. In TPD:F<sub>4</sub>TCNQ and TPD:HATCN<sub>6</sub> films, agglomerates are observed.

As shown in figure 5.17 a, TPD forms a smooth surface, and in the PF-TUNA-AFM micrograph a homogeneous conductivity is observed (see figure 5.17 d). The measured currents are very low and again within the limit of measurability. In the doped films, agglomerates without defined structure are observed upon doping with F<sub>4</sub>TCNQ (20 nm) and HATCN<sub>6</sub> (50 nm) (see figure 5.17 b, c). In case of doping with F<sub>4</sub>TCNQ it is visible that the agglomerates are not conductive (see figure 5.17 e). In light of the MIS-CELIV measurements on TPD:F<sub>4</sub>TCNQ where no additional charges upon doping could be measured, these agglomerates might hamper the doping. In AFM it is not possible to get any information about the composition of the agglomerates. In light of the MIS-CELIV and EPR measurements, it might be the case that F<sub>4</sub>TCNQ is not distributed well in the TPD and forms the agglomerates. Charge transfers then occur only at the interface of the agglomerates, but the charges cannot be separated and are therefore visible in EPR, but not in MIS-CELIV measurements.

Based on figure 5.17 f, it is difficult to conclude whether the agglomerates measured on TPD:HATCN<sub>6</sub> are just measurement artifacts caused by the height difference within the image or real conductive centers. Thus some agglomerates are measured on smaller scan size (see figure 5.18).



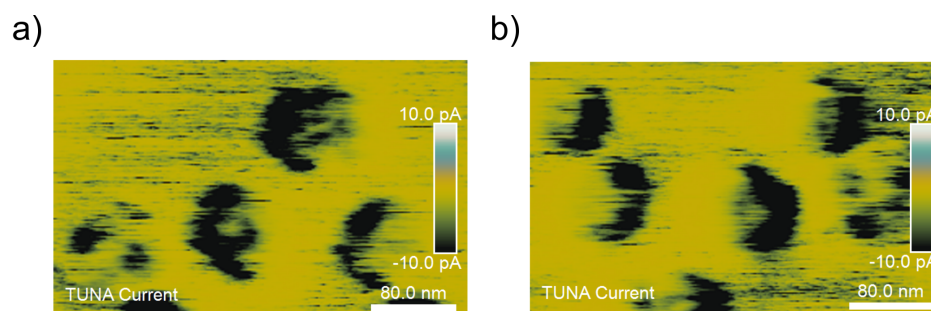


**Figure 5.18.** Detailed view of the agglomerates in TPD:HATCN<sub>6</sub> recorded in different scan directions (a) left to right, (b) right to left. Higher currents are only measured at the first larger height difference which indicates a measurement artifact.

The two pictures in figure 5.18 are measured in two different scan directions and show that higher currents are observed on the edges of the agglomerates, where the AFM tip makes first contact. On top and on the falling flank, no currents are measured. When measuring in the opposite direction the same observation is made. Together with the non-defined form of the agglomerates it can be concluded that they are not composed of neat dopant as in case of MTDATA:HATCN<sub>6</sub>.

In case of the corresponding polymer, the same smooth surfaces and conductivity homogeneities of the thin-films as for the PMTDATA films are observed as shown in figure 5.19 showing better film forming in case of the polymer as well. The homogeneous current pictures are also in accordance with the characterization before. This matches the former results of p-doping of PTPD in this chapter.

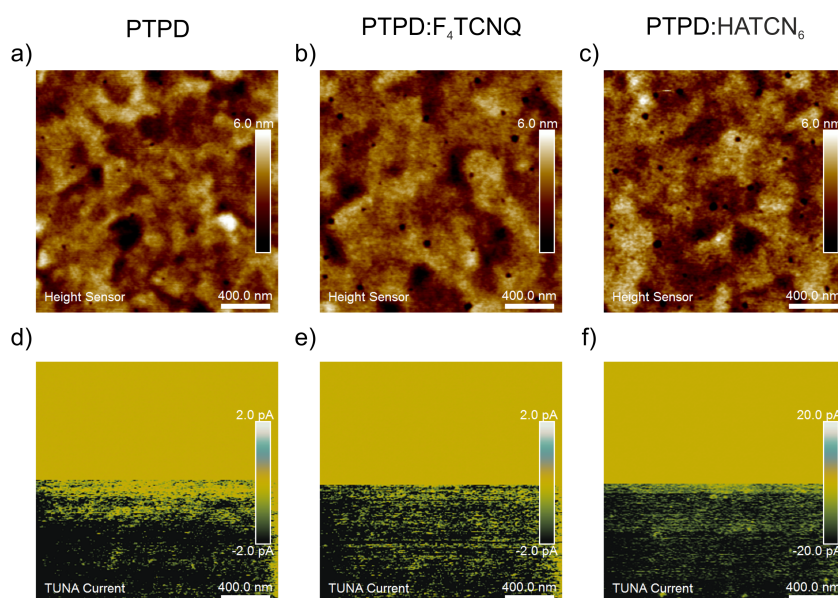


**Figure 5.19.** Topography (first row) and current pictures (second row) of undoped and doped (10 mol%) PTPD films. All films are very smooth and exhibit homogeneous conductivities in the PF-TUNA-AFM micrograph.

The AFM and PF-TUNA-AFM measurement showed agglomerates in molecular thin-films without defined form upon doping with HATCN<sub>6</sub> and enhanced film forming properties of the corresponding polymers. Nevertheless these agglomerates do not inhibit the doping as observed in the conductivity measurements by hole-only devices and MIS-CELIV which show the same conductivities for HATCN<sub>6</sub> doped polymers as for low-molecular weight matrices. In case of doping with F<sub>4</sub>TCNQ, the observed agglomerates may hamper the doping, because the only F<sub>4</sub>TCNQ doped film comprising agglomerates (TPD:F<sub>4</sub>TCNQ) does not show any doping effect in MIS-CELIV measurements.

### 5.2.5. Implementation of p-doped layers in organic light emitting diodes

To be employed as a hole injection or extraction layer in OLEDs or solar cells, the doped layer should be operated in the ohmic regime, e.g., below the transition voltage  $V_T$  between the ohmic and the SCLC regime.  $V_T$  can be calculated by equation 5.3 which is obtained from  $J_{\rho,\Omega} = J_{\rho,SCLC}$  in equation 5.1[149]

$$V_T = \frac{9}{8} \frac{e \cdot \rho \cdot d^2}{\epsilon_0 \cdot \epsilon_r} \quad (5.3)$$

Assuming a dielectric constant of 3.5 (estimated from the CELV displacement current) at a typical charge carrier injection layer thickness of 30 nm and taking into account the equilibrium hole density from Table 5.1,  $V_T = 21$  mV for undoped MTDATA is found.[150] Hence, at typical OLED driving voltages or typical photo-voltages in solar cells, the MTDATA layer will be driven into the SCLC regime with a substantial voltage drop over the charge carrier injection layer. In contrast, upon p-doping with F<sub>4</sub>TCNQ,  $V_T$  increases to 37 V. In this case, the MTDATA:F<sub>4</sub>TCNQ charge carrier injection layer is operated in the ohmic regime which implies less voltage drop over the layer and thus is more suited for device integration. In MTDATA:HATCN<sub>6</sub>,  $V_T$  is 2 V and therefore which is 100 times higher than for undoped MTDATA. PMTDATA shows a very low  $V_T = 37$  mV as well which increases for doping with HATCN<sub>6</sub> by a factor of 100 to 3 V. In PMTDATA:F<sub>4</sub>TCNQ,  $V_T = 16$  V is also much higher than any feasible device operating voltage.

Using pure TPD ( $V_T = 10$  mV) or PTPD ( $V_T = 5$  mV) the transition voltage is slightly lower. Upon doping with F<sub>4</sub>TCNQ,  $V_T$  increases to 16 V and 21 V, respectively which has about the same magnitude as MTDATA:F<sub>4</sub>TCNQ and PMTDATA:F<sub>4</sub>TCNQ. Upon doping of TPD with HATCN<sub>6</sub>, a transition voltage of 1 V is measured which is similar to HATCN<sub>6</sub> doped MTDATA and PMTDATA. Only  $V_T$  of PTPD:HATCN<sub>6</sub> is one order of magnitude lower ( $V_T = 0.2$  V), but still improved by a factor of 40 in comparison to undoped PTPD.



Thus, under common bias, all doped material systems operate in the ohmic regime and are therefore interesting for the implementation in OLEDs. Furthermore the corresponding polymers show similar results as the low-molecular materials but better film forming properties, making the p-doped polymers an interesting alternative.

To gain deeper insight into the performance of those materials the undoped and doped matrices are implemented in OLEDs. To ensure the same layer thicknesses of the soluble matrices and thus comparability, all following layers are evaporated. The energy levels of the employed materials are depicted in figure 5.20.

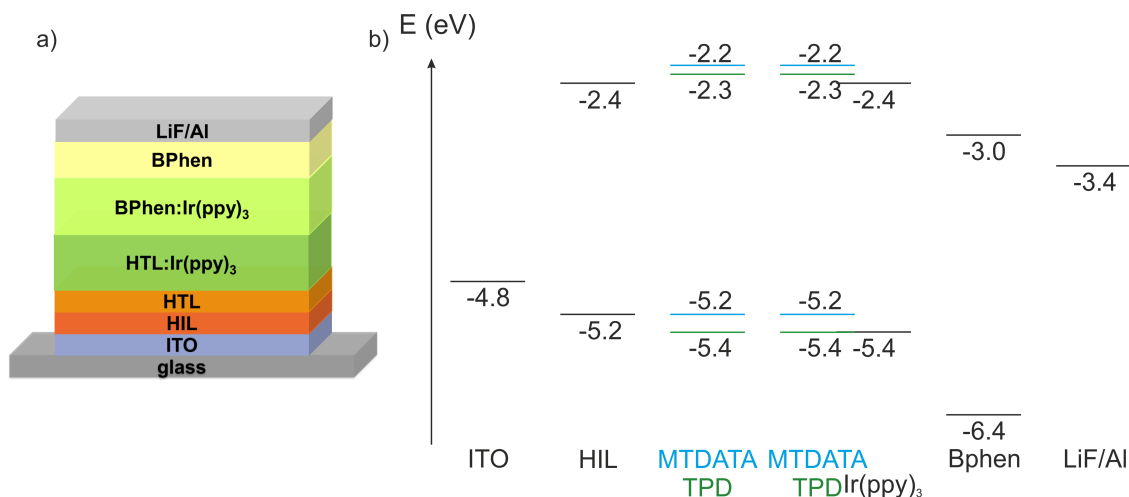


**Figure 5.20.** (a) Device architecture and (b) energy levels of the employed materials. An ITO/HIL/MTDATA/MTDATA:Ir(ppy)<sub>3</sub>/BPhen:Ir(ppy)<sub>3</sub>/BPhen/LiF/Al architecture was used. The energy levels are taken from the literature.[151–153]

ITO sputtered glass is used as transparent anode and LiF/Al as cathode. The solution processed undoped and doped matrices are used as hole injection layers and doped with 10 mol% due to the saturation at this concentration in the conductivity measurements. A thin layer of the pure matrix material is evaporated on top as hole transporting and electron blocking layer. This ensures that excess electrons cannot recombine with holes in the doped injection layer and thus quenching is inhibited. On the cathode side, as electron transporting and hole blocking layer, 4,7-diphenyl-1,10-phenanthroline (BPhen) is used for the same reasons. The triplet emitter tris[2-phenylpyridinato-C<sup>2</sup>,N]iridium(III) (Ir(ppy)<sub>3</sub>) is implemented in a hole transporting host (MTDATA or TPD) and an electron transporting host (BPhen). For reference, OLEDs containing an evaporated doped matrix layer (10 mol%) as HIL are built. The resulting J-V-L and power efficiency curves are shown in figure 5.21 - 5.24. For reasons of clarity, the curves of the reference OLEDs are not shown.

At first, OLEDs containing undoped and F<sub>4</sub>TCNQ doped MTDATA and PMTDATA as hole injection layers are investigated. The onset voltage at a luminance of 10 cd/m<sup>2</sup> shows no significant difference between undoped and doped matrices within the experimental

precision. All onset voltages  $V_{\text{on}} = 2.7$  V are well in accordance with the reference OLED comprising evaporated MTDATA:F<sub>4</sub>TCNQ HILs. No difference between the doped and undoped matrices is observed due to the negligible barrier between ITO and the emitter, but at higher luminosities, a shift of the L-V curves of doped matrices to lower voltages compared to undoped matrices is shown in figure 5.21:

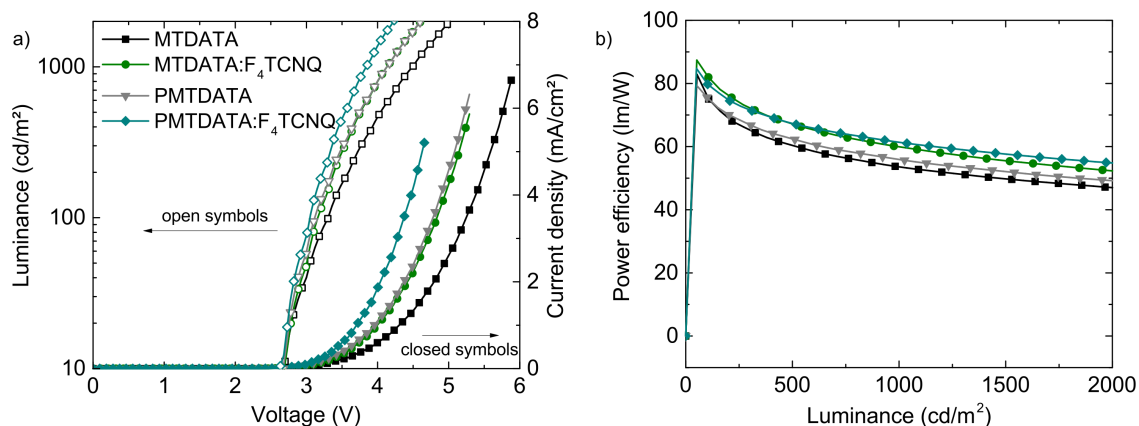


**Figure 5.21.** (a) J-V-L curves of OLEDs comprising undoped and F<sub>4</sub>TCNQ doped (10 mol%) MTDATA or PMTDATA as hole injection layers. Upon doping, a shift to lower voltages is observed. (b) Power efficiencies of the OLEDs including doped injection layers improve as well, together indicating a decrease of the injection barrier.

In figure 5.21 it is shown that to reach a given current density (1 mA/cm<sup>2</sup>) in undoped matrices, a voltage of  $V(J = 1 \text{ mA/cm}^2) = 4.3$  V (MTDATA) or  $V(J = 1 \text{ mA/cm}^2) = 4.0$  V (PMTDATA) is necessary. In case of MTDATA:F<sub>4</sub>TCNQ or PMTDATA:F<sub>4</sub>TCNQ, a 0.3 V lower voltage is required (4.0 V and 3.7 V, respectively). This indicates the formation of a hole injection barrier between the electrodes and the active material if undoped matrices are used. This barrier is reduced by implementing F<sub>4</sub>TCNQ doped MTDATA or PMTDATA layers which ensure ohmic contact to the electrodes. The evaporated MTDATA:F<sub>4</sub>TCNQ reference OLED exhibits a voltage of  $V(J = 1 \text{ mA/cm}^2) = 3.7$  V which matches the voltage of PMTDATA:F<sub>4</sub>TCNQ.

The same effect can be seen in the power efficiency. The OLEDs containing doped layers show a higher power efficiency of 60 lm/W (MTDATA:F<sub>4</sub>TCNQ) and 61 lm/W (PMTDATA:F<sub>4</sub>TCNQ) at a luminance of 1000 cd/m<sup>2</sup> while the undoped OLEDs show lower luminosities of 54 lm/W (MTDATA) and 56 lm/W (PMTDATA). The power efficiency of the completely evaporated reference OLED is slightly higher than the efficiency of OLEDs comprising doped matrices (63 lm/W). Both doped matrices show a good performance in OLEDs.

When using HATCN<sub>6</sub> instead of F<sub>4</sub>TCNQ, similar results are obtained. The onset voltage (2.6 V) at a luminance of 10 cd/m<sup>2</sup> shows no significant difference of all measured curves within the experimental precision. The reference OLED is almost the same (2.7 V). In comparison to undoped HILs, doped HILs exhibit a shift of the J-V curves to lower voltages at higher luminances which is visible in figure 5.22.

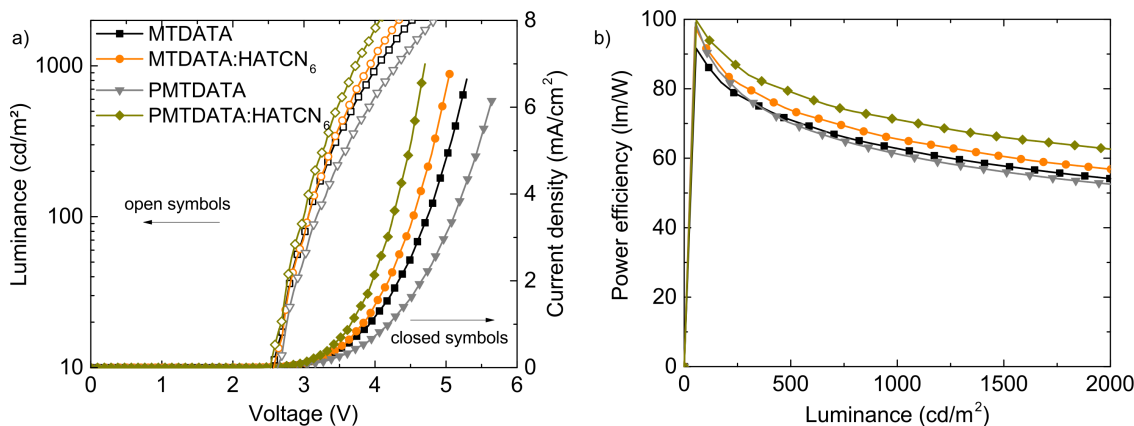


**Figure 5.22.** (a) J-V-L curves of OLEDs comprising undoped and HATCN<sub>6</sub> doped (10 mol%) MTDATA or PMTDATA as hole injection layers. Upon doping, a shift to lower voltages is observed. (b) The power efficiencies of the OLEDs including doped injection layers improve as well, Together indicating a decrease of the injection barrier.

Similar to the measurements of F<sub>4</sub>TCNQ doped matrices, the J-V curves in figure 5.22 show a shift to lower voltages if HATCN<sub>6</sub> doped matrices are used. The voltage to reach a  $J = 1 \text{ mA/cm}^2$  is 3.9 V (MTDATA) and 4.2 V (PMTDATA) in case of undoped matrices, and 3.8 V (MTDATA:HATCN<sub>6</sub>) and 3.7 V (PMTDATA:HATCN<sub>6</sub>) for doped ones. This again indicates a reduction of an injection barrier upon doping. The datas of both doped matrices are in accordance to the complete evaporated reference (3.6 V).

The power efficiency of the OLEDs comprising doped HILs is slightly increased from 63 lm/W to 66 lm/W in case of MTDATA and from 61 lm/W to 71 lm/W in case of PMTDATA. The reference OLED exhibits a power efficiency of 66 lm/W and agrees with the solution processed.

Both, MTDATA and the corresponding polymer, show increasing performance upon p-doping with F<sub>4</sub>TCNQ and HATCN<sub>6</sub>. Because the measured datas of doped PMTDATA are the same or even higher than of doped MTDATA, from the device data, it can be concluded, that attaching MTDATA moieties to a polymer backbone does not hamper the doping.

To test the performance of the undoped and doped matrices TPD and PTPD in optoelectronic devices, OLEDs containing TPD as host for Ir(ppy)<sub>3</sub> are characterized in the same way as the MTDATA matrices. The data are benchmarked against all-evaporated reference OLEDs containing doped hole injection layers.

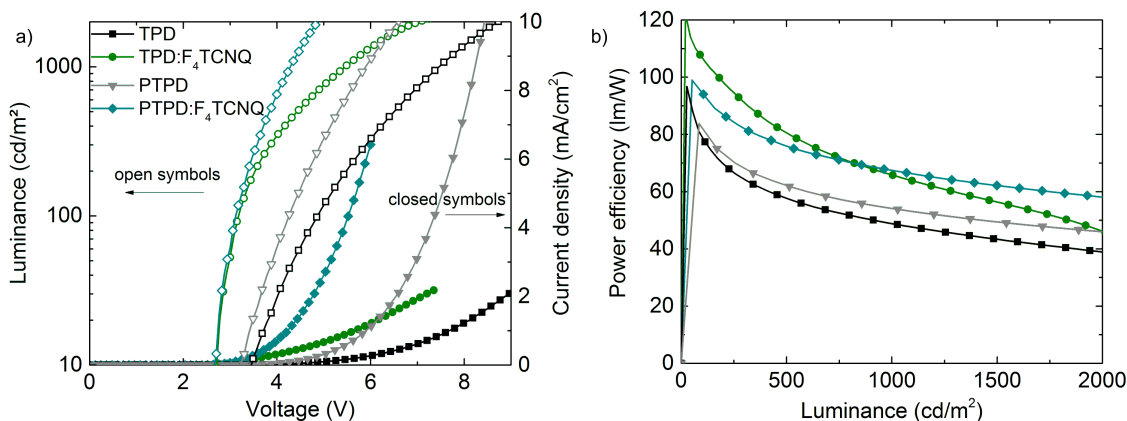


**Figure 5.23.** (a) J-V-L curves of OLEDs comprising undoped and F<sub>4</sub>TCNQ doped (10 mol%) TPD or PTPD as hole injection layers. Upon doping a shift to lower voltages is observed. (b) The power efficiencies of the OLEDs including doped injection layers improve as well, but for TPD:F<sub>4</sub>TCNQ the power efficiencies show a stronger roll-off. This matches the fact that the MIS-CELIV measurements for TPD:F<sub>4</sub>TCNQ does not show any doping.

Upon doping with F<sub>4</sub>TCNQ, the onset voltage is reduced from 3.4 V (TPD) and 3.3 V (PTPD) to 2.7 V in case of doped HILs (see figure 5.23 a). This is in accordance with the onset voltage of the reference OLED (2.8 V). A shift of the J-V curves to lower voltages is observed when F<sub>4</sub>TCNQ doped TPD or PTPD is used as hole injection layer. To reach a current density of 1 mA/cm<sup>2</sup>, 5.7 V (TPD:F<sub>4</sub>TCNQ) and 4.2 V (PTPD:F<sub>4</sub>TCNQ) are required. When using undoped HILs, to reach the same current density much higher voltages, 7.7 V (TPD) and 5.9 V (PTPD) are required. Thus the injection barrier is reduced upon doping.

The power efficiencies increase to 66 lm/W (TPD:F<sub>4</sub>TCNQ) and 67 lm/W (PTPD:F<sub>4</sub>TCNQ), whereas the undoped TPD and PTPD only enable OLED power efficiencies of 49 lm/W and 54 lm/W. The power efficiency of the all-evaporated reference OLED (52 lm/W) is below the others, except undoped TPD. This and the roll-off of the power efficiency of the OLED containing the solution processed TPD:F<sub>4</sub>TCNQ layer might be caused by inefficient doping as already shown in MIS-CELIV measurements.

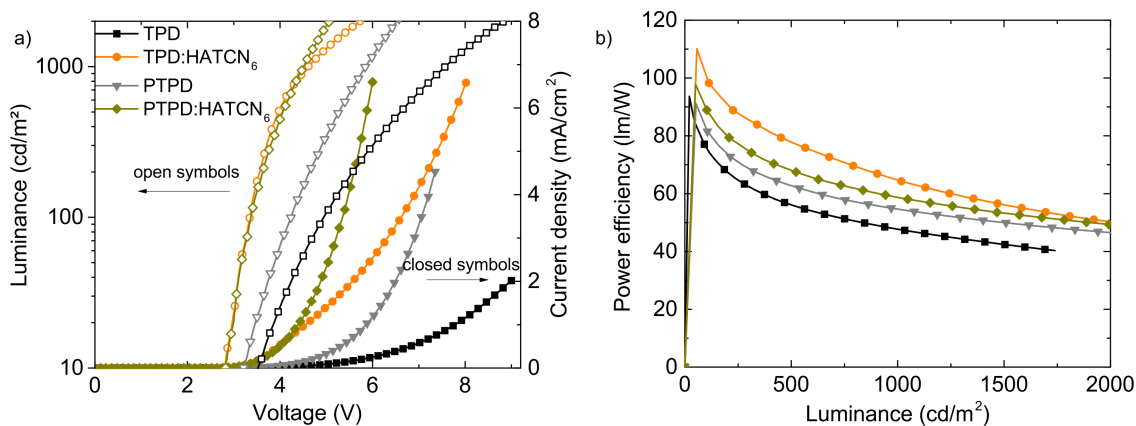


**Figure 5.24.** (a) J-V-L curves of OLEDs comprising undoped and HATCN<sub>6</sub> doped (10 mol%) TPD or PTPD as hole injection layers. Upon doping a shift to lower voltages is observed. (b) The power efficiencies of the OLEDs including doped injection layers are increased as well, together indicating a decrease of the injection barrier.

When using HATCN<sub>6</sub> instead, the onset voltage in figure 5.24 a at a given luminance of 10 cd/m<sup>2</sup> is reduced from 3.5 V (TPD) and 3.2 V (PTPD) to 2.8 V in both cases. This is in accordance with the all-evaporated reference OLED (2.8 V). The voltages at a current density of 1 mA/cm<sup>2</sup> show the same trends. The already discussed shift of the J-V curves to lower voltages due to doping is also observed in HATCN<sub>6</sub> doped TPD. The voltages required to reach a current density of 1 mA/cm<sup>2</sup> are 7.8 V and 5.8 V for undoped TPD and PTPD. If doping with HATCN<sub>6</sub>, this voltage is lowered to 4.5 and 4.4, respectively which is close to the the complete evaporated reference device (4.2 V). Thus the injection barrier between ITO and the emitter is effectively reduced.

The reduced barrier is also reflected in the power efficiencies (see figure 5.24 b). These are increased from 48 lm/W (TPD) and 55 lm/W (PTPD) to 65 lm/W (TPD:HATCN<sub>6</sub>) and 59 lm/W (PTPD:HATCN<sub>6</sub>). Those are higher than of the all-evaporated reference OLED (59 lm/W). Again, this shows that the side-chain polymers can be used as good alternatives for low-molecular weight materials without limitations of the optoelectronic properties.

### 5.2.6. Summary

TPD:F<sub>4</sub>TCNQ is the only matrix:dopant system that does not exhibit generation of additional charges due to doping as shown by MIS-CELIV measurements. This may originate from agglomerates observed in AFM. It may also cause the roll-off in the power efficiency of the OLEDs. For all other solution processable matrices, MTDATA, PMTDATA, TPD and PTPD, doping with the acceptors F<sub>4</sub>TCNQ and HATCN<sub>6</sub> leads to electron transfer from the matrix to the dopant. This p-doping equally enhances the spin concentration and electrical conductivities of the polymeric and the molecular thin-films. The characterization of the OLEDs showed that doped HILs injection barriers are reduced and ohmic contacts between the anode and the emitter are realized. With doped HILs at least the same datas as for complete evaporated devices are reached.

### 5.3. Crosslinkable polymer matrices

In the previous chapter it was concluded that the polymerization of the MTDATA- and TPD-like monomers have no negative influence on the *p*-doping. To evaluate whether this prevails if crosslinkable 1-alkynyl ether groups are added, the experiments described in chapter 5.2 are also carried out on the modified crosslinkable polymers XMTDATA and XTPD. Both are doped with F<sub>4</sub>TCNQ and HATCN<sub>6</sub> and their chemical and opto-electronic properties are analyzed before and after crosslinking by thermal annealing. In addition, the influence of the crosslinking conditions and the temperature dependency of the doping is investigated.

#### 5.3.1. Effect of the additional crosslinkable group on the *p*-doping

To investigate the effect of the crosslinkable group on *p*-doping only, at first, the characterization is carried out without thermal annealing and hence without triggering crosslinking.

##### 5.3.1.1. Shift of the ionization potential due to *p*-doping

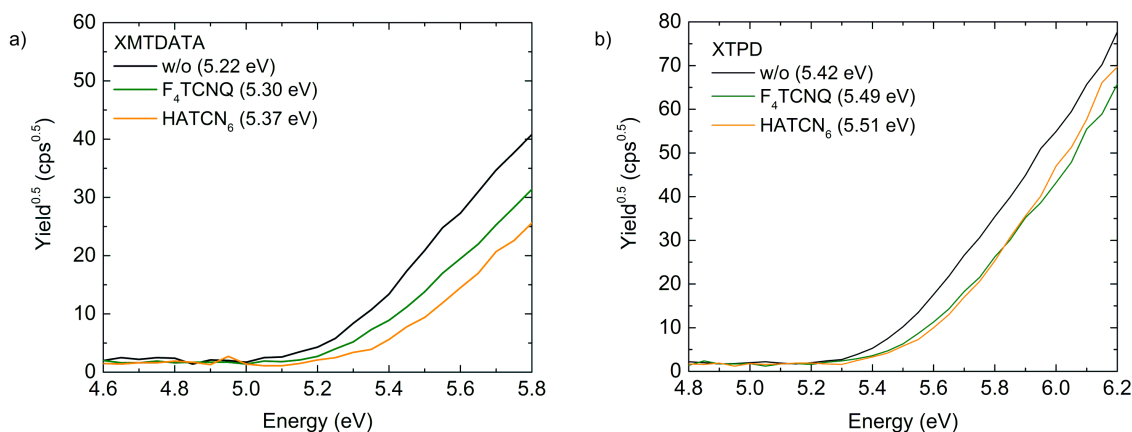


**Figure 5.25.** Photoelectron yield of undoped and doped (20 mol%) (a) XMTDATA and (b) XTPD before annealing, measured by PESA. The shift of the ionization potential to lower energies indicates an electron deficiency on the matrices due to doping with F<sub>4</sub>TCNQ and HATCN<sub>6</sub>.

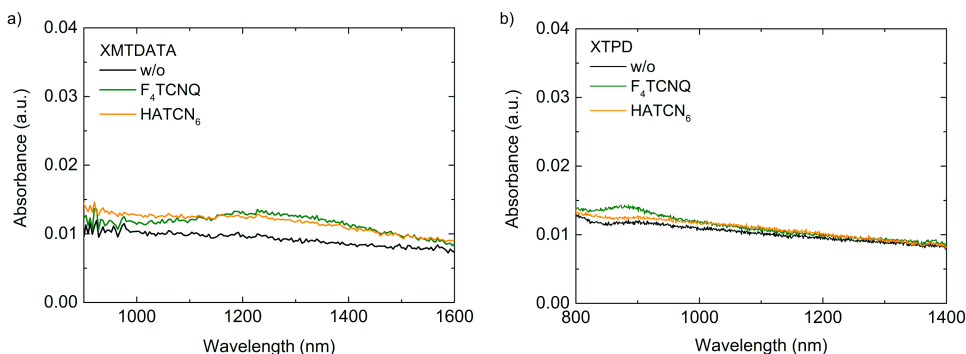
As shown in figure 5.25, the doping of the crosslinkable materials results in a shift in the ionization potential similar to the non-crosslinkable polymers. All ionization potentials are summarized within table 5.3. The E<sub>I</sub> of XMTDATA is identical with the E<sub>I</sub> of PMTDATA within experimental certainties. The shift in the ionization potential of  $\Delta E_I = (0.08 \pm 0.02)$  eV in case of XMTDATA:F<sub>4</sub>TCNQ compared to PMTDATA:F<sub>4</sub>TCNQ is almost the same. In case of HATCN<sub>6</sub>, an even stronger shift can be observed ( $\Delta E_I = (0.15 \pm 0.02)$  eV). Within measurement certainties the shifts in ionization potential upon doping of XTPD,  $\Delta E_I = (0.07 \pm 0.02)$  eV in case of XTPD:F<sub>4</sub>TCNQ and  $\Delta E_I = (0.09 \pm 0.02)$  eV in case of XTPD:HATCN<sub>6</sub>, are similar to the doped PTPD films. Hence the additional crosslinkable group has no effect on the ionization potential.

**Table 5.3.** Measured ionization potentials of all undoped and doped (20 mol%) matrix:dopant systems.

	$E_I$ (eV)		$E_I$
MTDATA	5.11±2	TPD	5.43±2
MTDATA:F <sub>4</sub> TCNQ	5.18±2	TPD:F <sub>4</sub> TCNQ	5.53±2
MTDATA:HATCN <sub>6</sub>	5.16±2	TPD:HATCN <sub>6</sub>	5.59±2
PMTDATA	5.20±2	PTPD	5.42±2
PMTDATA:F <sub>4</sub> TCNQ	5.26±2	PTPD:F <sub>4</sub> TCNQ	5.51±2
PMTDATA:HATCN <sub>6</sub>	5.26±2	PTPD:HATCN <sub>6</sub>	5.54±2
XMTDATA	5.22±2	XTPD	5.42±2
XMTDATA:F <sub>4</sub> TCNQ	5.30±2	XTPD:F <sub>4</sub> TCNQ	5.49±2
XMTDATA:HATCN <sub>6</sub>	5.37±2	XTPD:HATCN <sub>6</sub>	5.51±2

### 5.3.1.2. Electronic states and doping efficiencies

In analogy to the non-crosslinkable polymers and the low-molecular weight materials the electron transfer upon doping of the crosslinkable materials is studied by means of UV-vis-NIR spectrometry and EPR spectroscopy.

**Figure 5.26.** UV-vis-NIR absorption spectra of undoped and doped matrices (a) XMTDATA and (b) XTPD. Additional absorption bands indicate the formation of new polaronic states upon doping.

In the spectra of non-annealed doped XMTDATA (figure 5.26), additional bands upon doping with F<sub>4</sub>TCNQ and HATCN<sub>6</sub> are observed. As shown for the non-crosslinkable TPD matrices before, only doping with F<sub>4</sub>TCNQ yields an additional band for doped XTPD. The similarity of the spectra with the spectra of PMTDATA and PTPD indicates that the additional 1-alkynyl-ether group does not effect the formation of polaronic states upon doping.



To gain further information about the charge transfer of the non-annealed doped crosslinkable polymers, the numbers of unpaired spins are measured by EPR spectroscopy.

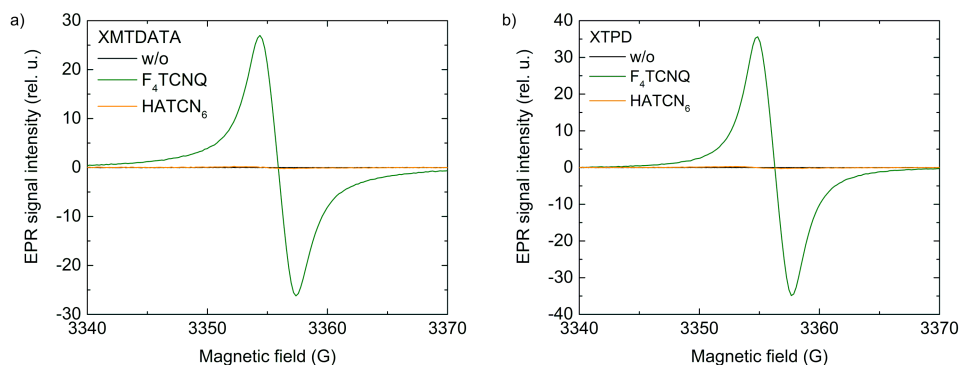


**Figure 5.27.** EPR spectra obtained from undoped and doped (20 mol%) XMTDATA and XTPD. For undoped matrices (black line), almost no EPR signals are observed. Upon doping with  $F_4TCNQ$  (green line), the EPR experiments show a strong signature of unpaired spins and hence an integer charge transfer. Such a signature is also visible when employing the dopant  $HATCN_6$  (orange line), but with a significantly reduced signal.

As depicted in figure 5.27, in analogy to the undoped matrices characterized before, no significant EPR signal is measured for undoped XMTDATA and XTPD. Upon doping with  $F_4TCNQ$  a strong signal is detected indicating an integer charge transfer to the dopant. The doping with  $HATCN_6$  exhibits a smaller increase in the EPR signal. Again this matches the higher electron affinity of  $HATCN_6$  compared to  $F_4TCNQ$  as in case of the non-crosslinkable matrices characterized before.

To gain quantitative information of the doping efficiencies, the absolute number of spins are also calculated for the crosslinkable species. The measured data and derived electrical material properties are summarized in Table 5.4:

**Table 5.4.** Number of spins per volume and doping efficiency of the non-annealed matrix-dopant (20 mol%) combinations as calculated from the EPR measurements.

	Total amount of spins	Spin concentration ( $cm^{-3}$ )	Doping efficiency (%)
XMTDATA	$5 \times 10^{11}$	$2 \times 10^{15}$	0
XMTDATA: $F_4TCNQ$	$1 \times 10^{15}$	$4 \times 10^{18}$	1
XMTDATA: $HATCN_6$	$4 \times 10^{13}$	$2 \times 10^{17}$	0.05
XTPD	$1 \times 10^{12}$	$5 \times 10^{15}$	0
XTPD: $F_4TCNQ$	$8 \times 10^{14}$	$3 \times 10^{18}$	1
XTPD: $HATCN_6$	$4 \times 10^{13}$	$2 \times 10^{17}$	0.04



The spin concentration of undoped XMTDATA and XTPD is with  $2 \times 10^{15} \text{ cm}^{-3}$  and  $5 \times 10^{15} \text{ cm}^{-3}$  again at the lower resolution limit. When doping with  $\text{F}_4\text{TCNQ}$ , in both cases, an increase of three orders of magnitude to  $4 \times 10^{18} \text{ cm}^{-3}$  (XMTDATA: $\text{F}_4\text{TCNQ}$ ) and  $3 \times 10^{18} \text{ cm}^{-3}$  (XTPD: $\text{F}_4\text{TCNQ}$ ) is determined. Upon doping with  $\text{HATCN}_6$ , a slightly lower increase of two orders of magnitude to  $2 \times 10^{17} \text{ cm}^{-3}$  (XMTDATA: $\text{HATCN}_6$ ) and  $2 \times 10^{17} \text{ cm}^{-3}$  (XTPD: $\text{HATCN}_6$ ) is observed. The derived numbers of unpaired spins, the calculated spin concentration and the doping efficiencies are similar to the datas of the non-crosslinkable side-chain polymers, again indicating that the 1-alkynyl ether group has no significant effect on the doping process.

After ensuring that the crosslinkable 1-alkynyl ether group itself has no detrimental effect on the doping, the effect of crosslinking on the doped matrices is investigated.

### 5.3.2. Doping stability during crosslinking

To gain information about undoped and doped XMTDATA and XTPD, UV-vis-NIR spectra are measured before and after crosslinking. The crosslinking of XMTDATA is achieved by annealing at  $160^\circ\text{C}$  for 30 min of XTPD 10 min at  $180^\circ\text{C}$ .

#### 5.3.2.1. Charge transfer after crosslinking

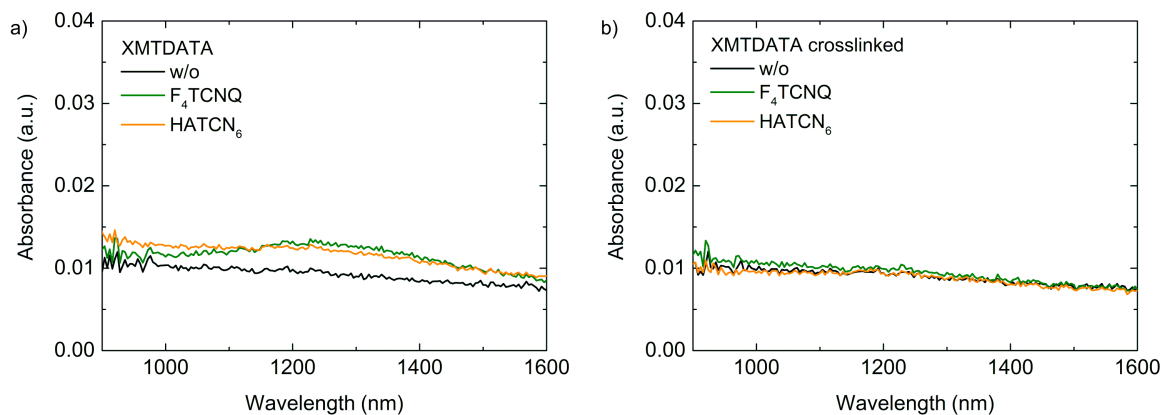


**Figure 5.28.** UV-vis-NIR spectra of undoped and doped (20 mol%) matrices XMTDATA (a) before and (b) after annealing. The additional absorption bands formed upon doping before annealing disappear after heating at  $160^\circ\text{C}$  for 30 min. This indicates that the doping is not stable at elevated temperatures.

In figure 5.28, the additional absorption bands caused by the doping disappear after thermal crosslinking ( $160^\circ\text{C}$ , 30 min). All samples show the same spectra as undoped XMTDATA which does not change upon annealing. This indicates that XMTDATA is not degenerated by annealing.

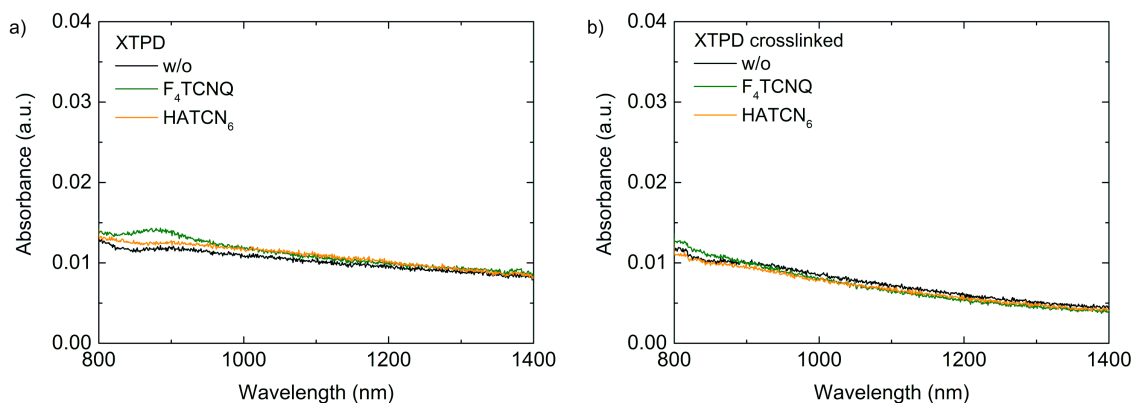


**Figure 5.29.** UV-vis-NIR spectra of doped (20 mol%) and undoped XTPD (a) before and (b) after annealing. Before annealing, doping with  $F_4TCNQ$  causes an additional bands which disappear after heating at  $180^\circ C$  for 10 min, indicating that the doping is not stable at elevated temperatures.

Similar results are observed for doped and undoped XTPD before and after annealing (see figure 5.29). Again, doping is not stable at the even higher crosslinking temperature ( $180^\circ C$ , 10 min), but no differences are observed in the undoped XTPD before and after annealing, indicating a stability of XTPD itself during crosslinking.

To evaluate whether annealing completely quenches the doping, conductivity measurements are performed on the doped crosslinked polymers. The conductivities are lower than  $10^{-11}$  S/cm and therefore they are not distinguishable from background noise. Thus it can be concluded, that doping dies not prevail crosslinking.

### 5.3.2.2. Surface properties of crosslinked film

To further study the changes within the films introduced by thermal annealing, topography measurements are performed on the undoped and doped 30 nm thick thin-films by AFM.

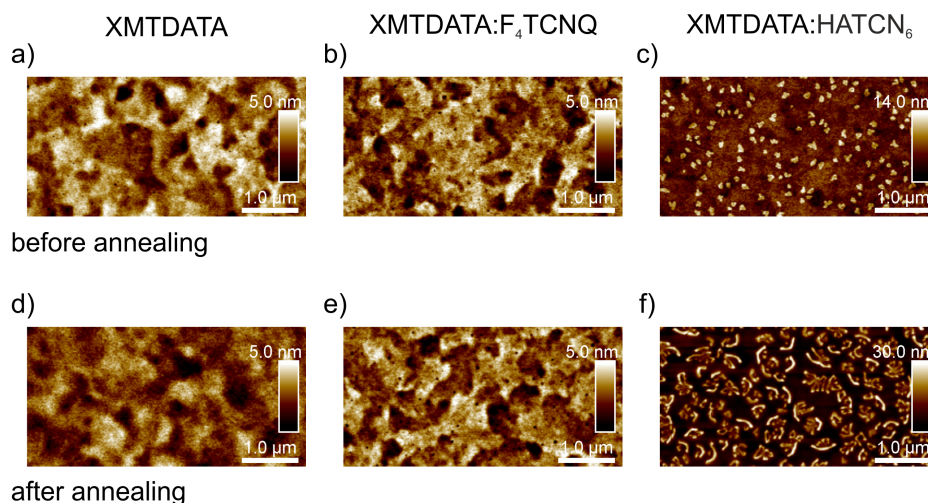


**Figure 5.30.** Topography of undoped and doped XMTDATA films before (first row) and after (second row) crosslinking. XMTDATA and XMTDATA: $F_4TCNQ$  films are very smooth independent of the annealing step. On the XMTDATA: $HATCN_6$  films, small agglomerates are observed which grow to large crystals after annealing.

In figure 5.30, topography measurements of undoped and doped XMTDATA films before and after crosslinking are shown. The AFM micrographs before annealing are similar to the topography measurements of undoped and doped MTDATA shown in chapter 5.2.4. After annealing, neat XMTDATA and XMTDATA:F<sub>4</sub>TCNQ exhibit very smooth films independent of the crosslinking. In case of XMTDATA:HATCN<sub>6</sub>, large crystals with sizes on the order of 350 nm are formed. The defined structure of these crystals indicates, that they are HATCN<sub>6</sub> crystals.

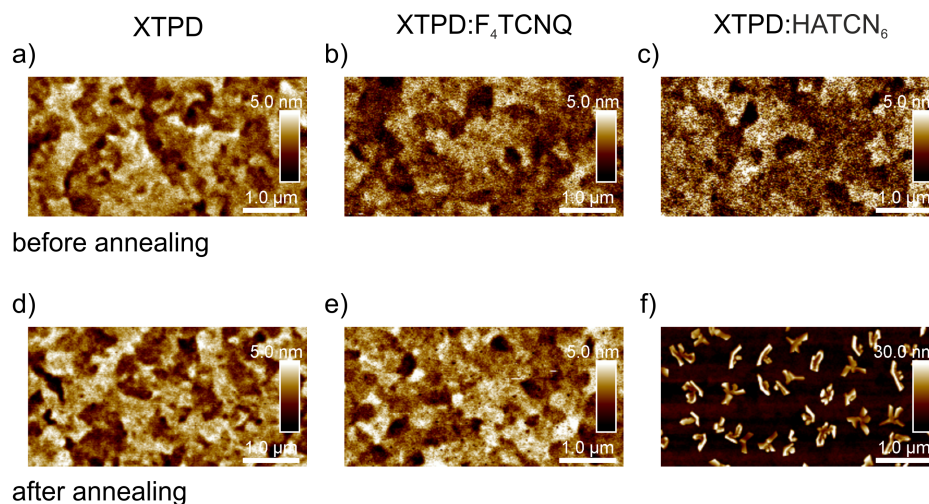


**Figure 5.31.** Topography of undoped and doped XTPD films before (first row) and after (second row) crosslinking. XTPD and XTPD:F<sub>4</sub>TCNQ films are very smooth before and after annealing. The XTPD:HATCN<sub>6</sub> film is very smooth before annealing, too, but afterwards large crystals are observed.

In the topography of XTPD films, similar observations are made. Before annealing, the films show similar results as the undoped and doped PTPD films discussed in chapter 5.2.4. After crosslinking pure XTPD and XTPD:F<sub>4</sub>TCNQ still exhibit a smooth surface, but on the XTPD:HATCN<sub>6</sub> films large three-armed crystals with sizes of around 350 nm are observed similar to crosslinked XMTDATA:HATCN<sub>6</sub> films which indicates that they are composed of pure HATCN<sub>6</sub> as well.

To gain further information about these crystals in annealed HATCN<sub>6</sub> doped matrices, the crosslinked polymer films are characterized by PF-TUNA-AFM as shown in figure 5.32.

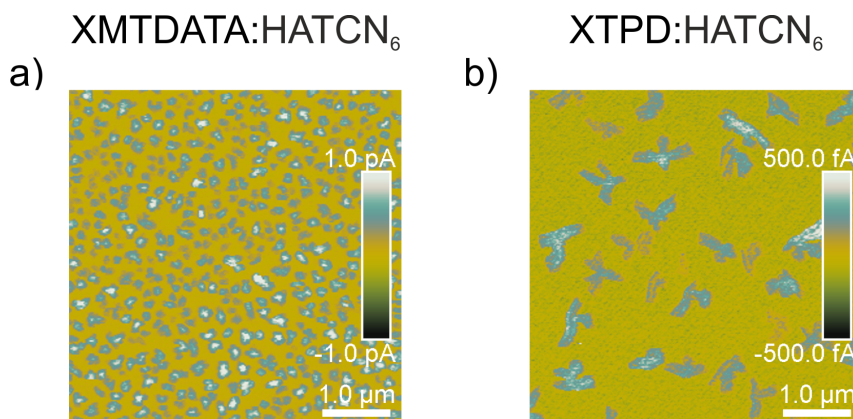


**Figure 5.32.** PF-TUNA-AFM micrographs of the crystals in the HATCN<sub>6</sub> doped crosslinked polymer films. The crystals are more conductive, especially in the center, than the surrounding surface. This indicates that the crystals create a contact to the ITO underneath.

In contrast to the non-conductive agglomerates without any defined structure observed in non-annealed HATCN<sub>6</sub> doped matrix films in chapter 5.2.4, the three-armed crystals in the crosslinked polymers exhibit a higher conductivity than the surrounding surface and also a defined crystalline structure. This indicates that the crystals are composed of pure HATCN<sub>6</sub> and are large enough to contact the ITO underneath through the 30 nm film.

### 5.3.2.3. Influence of crosslinking on undoped matrices in OLEDs

Since no differences in the characterization of undoped matrices before and after crosslinking were measured by different methods, annealed and non-annealed undoped crosslinkable and non-crosslinkable polymer matrices are implemented in OLEDs. This way the temperature dependency of the hole transport properties of the crosslinkable and non-crosslinkable polymers can be evaluated. To ensure the same layer thicknesses of the soluble matrices and thereby comparability, all subsequent layers are evaporated. The device architecture and the energy diagram of the OLEDs is illustrated in figure 5.33.

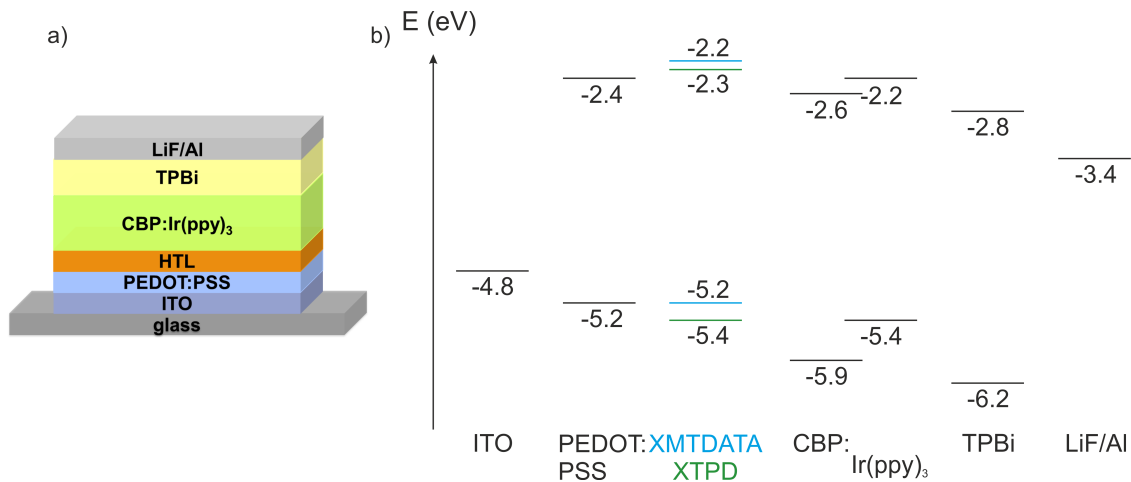


**Figure 5.33.** (a) Device architecture and (b) energetic structures of the used OLEDs. An ITO/PEDOT:PSS/HTL/CBP:Ir(ppy)<sub>3</sub>/TPBi/LiF/Al architecture was used. The energy levels are taken from the literature.[153]

ITO coated glass is used as transparent anode and LiF/Al as cathode. The common hole injection layer PEDOT:PSS is spincoated on top. The solution processed annealed and non-annealed undoped matrices are used as hole transport layers. As emission layer the green phosphorescent material tris[2-phenylpyridinato-C<sup>2</sup>,N]iridium(III) (Ir(ppy)<sub>3</sub>) is co-evaporated with the common host 4,4'-bis(N-carbazolyl)-1,1'-biphenyl (CBP) is used followed by TPBi as electron transporting and hole blocking layer on the cathode side. This OLED stack is known from efficient devices in the literature.[154] For reference, OLEDs are build comprising an evaporated hole transport layer (MTDATA or TPD).

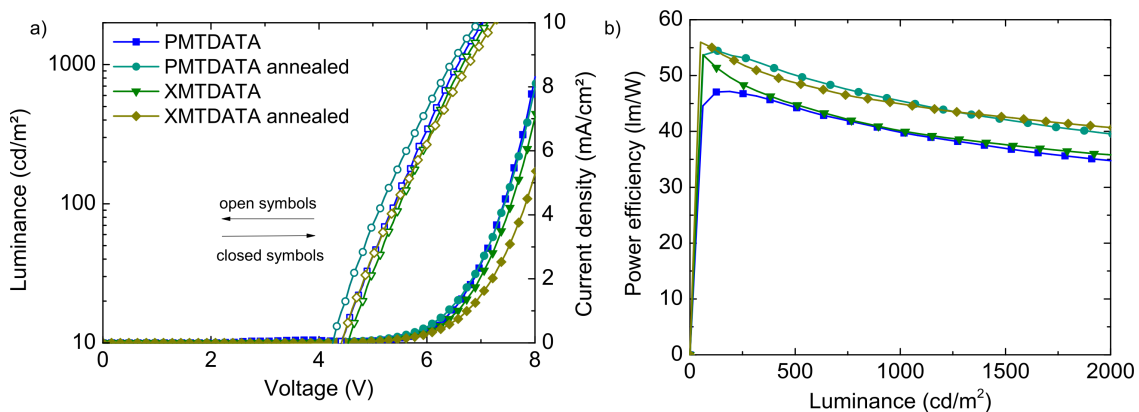


**Figure 5.34.** (a) J-V-L curves of OLEDs comprising annealed and non-annealed PMTDATA or XMTDATA as hole transport layers. No significant difference in the J-V curves and the onset voltage is observed. (b) The power efficiencies of the OLEDs comprising annealed transport layers are about 5 lm/W higher than the non-annealed.

At first, OLEDs with annealed and non-annealed PMTDATA and XMTDATA as hole transport layers are prepared. Figure 5.34 shows the corresponding J-V-L curves. The onset voltage at a luminance of 10 cd/m<sup>2</sup> shows no significant difference between annealed and non-annealed matrices within the experimental accuracy. In all devices, the onset voltage is around 4.4 V which is slightly lower than in case of the evaporated MTDATA HTL (4.8 V). To achieve a current density of 1 mA/cm<sup>2</sup> a voltage of  $V(J = 1 \text{ mA/cm}^2) = 6.5 \text{ V}$  is necessary for all HTLs (including the all-evaporated reference OLED) within the experimental accuracy. This indicates that the high temperature has no effect on the undoped matrices. Thus the polymers are stable against degeneration

at these temperatures. The power efficiency at a luminance of 1000  $\text{cd/m}^2$  after annealing is even higher (45  $\text{lm/W}$ ) than before (40  $\text{lm/W}$ ) for both polymers. In case of the reference OLED an even lower data (31  $\text{lm/W}$ ) is measured. Thus the non-crosslinkable and the crosslinkable polymers show good performance in OLEDs and no negative effect from annealing was found.

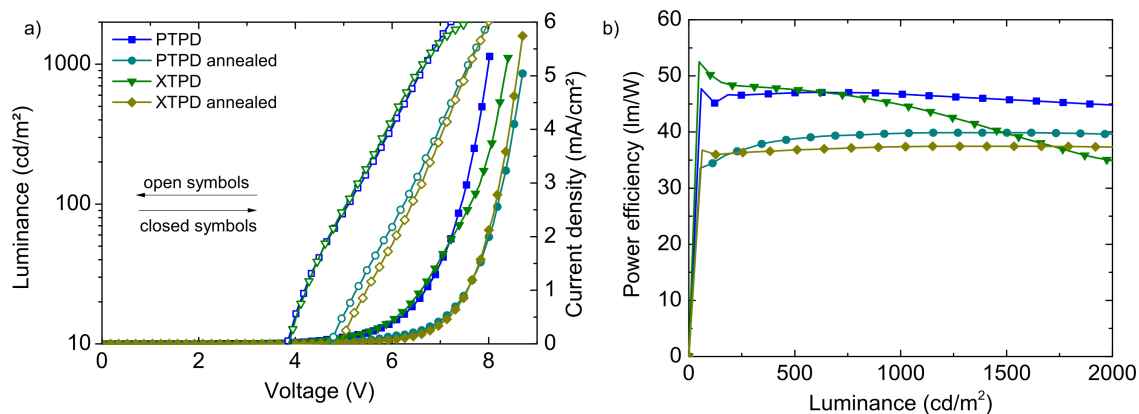


**Figure 5.35.** (a) J-V-L curves of OLEDs comprising annealed and non-annealed PTPD or XTPD as hole transport layers. No significant difference in the J-V curves and the onset voltage is observed. (b) The power efficiencies of the OLEDs including annealed transport layers are around 7  $\text{lm/W}$  lower than the undoped ones.

Using annealed and non-annealed PTPD and XTPD as hole transport layers slightly different datas are observed. As depicted in figure 5.35, upon annealing the onset voltage at a luminance of 10  $\text{cd/m}^2$  increases from 3.8 V (PTPD) and 3.9 V (XTPD) to 4.7 V and 4.9 V, respectively. For a current density of 1  $\text{mA/cm}^2$  a voltage of around 6.6 V is required for all polymers which increases to 7.5 V after annealing. The reference OLED with an evaporated TPD HTL exhibits a lower voltage of 5.5 V and a slightly lower onset voltage of 3.6 V, too. In contrast to the MTDATA polymers, PTPD and XTPD may be damaged at high temperatures. The same results are found in the power efficiencies. Before annealing, 47  $\text{lm/W}$  (PTPD) and 45  $\text{lm/W}$  (XTPD) are measured which is higher than after annealing (40  $\text{lm/W}$  for PTPD and 37  $\text{lm/W}$  for XTPD). The power efficiency of the reference OLED yields similar performance (36  $\text{lm/W}$ ). Thus the non-crosslinkable and the crosslinkable polymers still show a good performance in OLEDs, but a small negative effect of the annealing on the performance was found, in contrast to the MTDATA polymers which may be caused by the higher crosslinking temperature.

Therefore, it can be concluded that the crosslinking temperature has no (XMTDATA) or only a small (XTPD) negative impact on the optoelectronic properties of the materials. In contrast the doping process is not stable at the crosslinking temperatures.



## 5.4. Temperature stability of p-doping

To gain deeper insight in the origin of the incompatibility of doping and crosslinking, AFM and UV-vis-NIR measurements at different temperatures are performed.

### 5.4.1. Crystallization of dopants at higher temperatures

The surfaces of the films of undoped and doped matrices after annealing at the crosslinking conditions of the corresponding crosslinkable polymers are analyzed (MTDATA, PMTDATA: 160°C, 30 min/TPD, PTPD: 180°C, 10 min) and these are compared with AFM micrographs before annealing (see chapter 5.2.4).

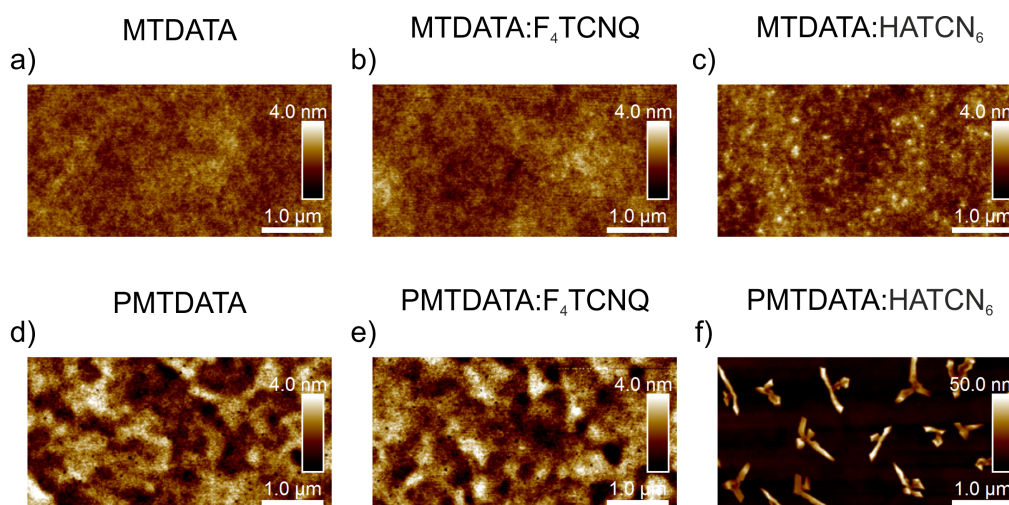


**Figure 5.36.** Topography of undoped and doped (10 mol%) MTDATA and PMTDATA films after annealing. Undoped and  $F_4TCNQ$  doped films exhibit a smooth surface. The large agglomerates in MTDATA:HATCN<sub>6</sub> before annealing (see figure 5.15) shrink afterwards. The initially smooth PMTDATA:HATCN<sub>6</sub> film forms large crystals after annealing.

In figure 5.36, the undoped and  $F_4TCNQ$  doped MTDATA (see figure 5.36 a, b) and PMTDATA (see figure 5.36 d, e) films still exhibit smooth surfaces, even after annealing (compare figure 5.15 a, b and 5.16 a, b). In case of MTDATA:HATCN<sub>6</sub> (see figure 5.36 c), before annealing, agglomerates are found on the surface (see figure 5.15 c). Their size is significantly reduced after annealing. This originates from the higher mobility of the molecules after heating far above the glass temperature ( $T_g = 75^\circ C$ ).<sup>[136]</sup> In HATCN<sub>6</sub> doped PMTDATA films (see figure 5.36 f) which show a smooth surface before thermal treatment (see figure 5.16 c), three-armed HATCN<sub>6</sub> crystals with the size of 800 nm are formed after annealing. The same crystals are observed in the crosslinked polymers. From the defined structure of the crystals which differs very much from the non-defined agglomerates depicted in figure 5.15 c, it can be concluded, that these are HATCN<sub>6</sub> crystals. The formation of crystals only in the polymer film may stem from the generally worse miscibility of polymers compared to low-molecular weight materials. During

spincoating the system is quenched in a metastable state which is allowed to equilibrate during annealing. In case of polymer mixtures this often leads to phase separation. Similar observations are made in annealed TPD matrices (see figure 5.37).

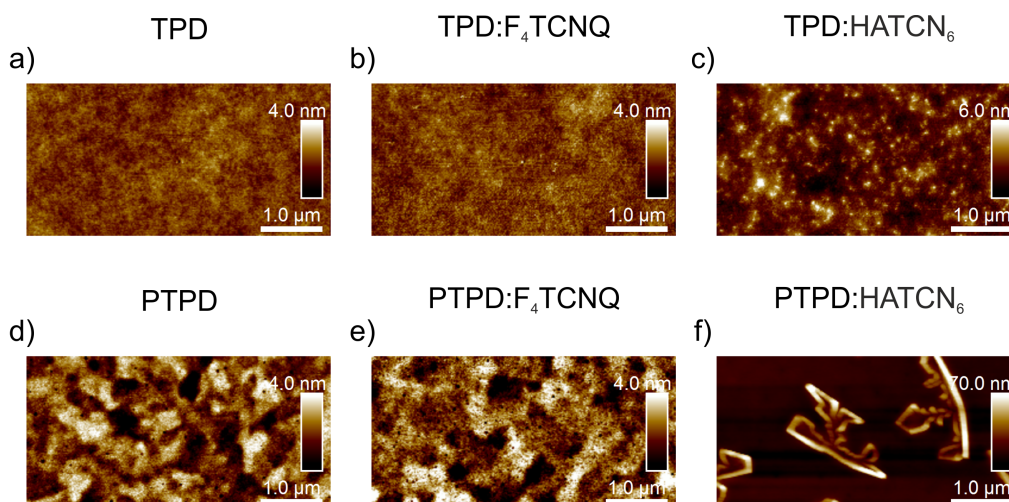


**Figure 5.37.** Topography of undoped and doped (10 mol%) TPD and PTPD films after annealing. Undoped matrices and PTPD:F<sub>4</sub>TCNQ doped films exhibit a smooth surface. The agglomerates in TPD:F<sub>4</sub>TCNQ and TPD:HATCN<sub>6</sub> before annealing (compare figure 5.17 b, c) shrink afterwards. The initially smooth PTPD:HATCN<sub>6</sub> film (compare figure 5.19 c) forms large three-armed crystals after annealing.

Figure 5.37 a, d and e show smooth films for undoped TPD, PTPD and PTPD:F<sub>4</sub>TCNQ, similar to the films without thermal treatment (see figure 5.17 a, 5.19 a, b). The agglomerates on TPD:F<sub>4</sub>TCNQ and TPD:HATCN<sub>6</sub> films which are observed in non-annealed samples (see figure 5.17 b, c), shrink during annealing and, in case of doping with F<sub>4</sub>TCNQ (b), vanish completely after heating at 180°C for 10 min. Again the annealing temperature (180°C) is much higher than the material's glass temperature ( $T_g = 60^\circ\text{C}$ ).<sup>[137]</sup> The HATCN<sub>6</sub> doped PTPD film which is very smooth before heating (figure 5.19 c), exhibits large three-armed HATCN<sub>6</sub> crystals after annealing under crosslinking conditions (see figure 5.37 f). Again, this might be a problem of the general low miscibility of polymers.

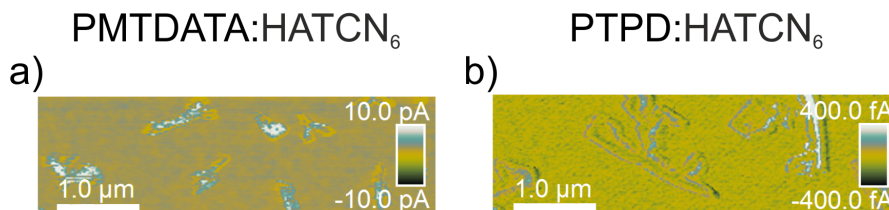


**Figure 5.38.** PF-TUNA-AFM micrographs of (a) HATCN<sub>6</sub> doped PMTDATA and (b) PTPD after annealing. The crystals on the PMTDATA surface are more conductive than the surrounding surface due to a contact to ITO. The crystals on PTPD show no connection to the underlying ITO.



The HATCN<sub>6</sub> crystals are further investigated by PF-TUNA-AFM (see figure 5.38). The higher conductivity of the crystals in PMTDATA compared to the surrounding surface indicates that the crystals create short cuts to the ITO layer underneath. In case of PTPD:HATCN<sub>6</sub>, no contact to the ITO is found.

These results show a thermal instability of the doping of polymers with HATCN<sub>6</sub> due to a phase separation at higher temperatures. In addition, this phase separation can lead to short cuts by HATCN<sub>6</sub> crystals.

### 5.4.2. Temperature dependency

To further investigate the stability of p-doping by F<sub>4</sub>TCNQ against thermal annealing, vis-NIR spectra of MTDATA:F<sub>4</sub>TCNQ are recorded at different temperatures in solution and in thin-films. For this purpose, the solution is heated in 25°C steps from 25°C to 100°C and cooled down with the same step size back to 25°C. The spectra are measured after 10 min at the respective temperature to ensure thermal equilibrium. The resulting spectra of a MTDATA:F<sub>4</sub>TCNQ solution in toluene are shown in figure 5.39.

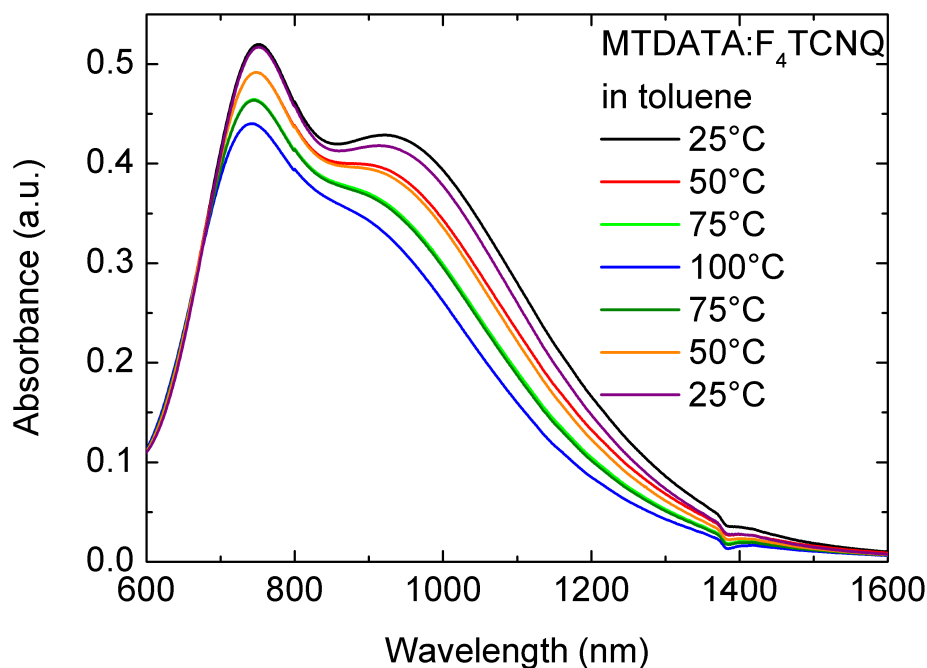


**Figure 5.39.** Vis-NIR spectra of MTDATA:F<sub>4</sub>TCNQ-solution in toluene (20 mol%) at different temperatures. The temperature is increased from 25 to 100°C in 25°C steps and afterwards cooled down to 25°C again in 25°C steps. Before each measurement, the sample is equilibrated at the measurement temperature for 10 min. The absorption band between 600 and 1600 nm decreases with increasing temperature and increases back to its original data while cooling down again.

The absorption band between 600 and 1600 nm which reflects polaronic states created upon doping, decreases with increasing temperature. When cooling down again, the former intensity of the band is recovered. This indicates that the doping process is reversible. Thus thermal energy introduced to the system can reverse the electron transfer. If the temperature is reduced, the thermal energy is no longer high enough to hold the electron in the matrix' HOMO and it is transferred to the dopants LUMO again. The processes are reversible at least up to 100°C. Unfortunately, higher temperatures cannot be studied in toluene solution due to its high vapor pressure.

Based on the results of the solution spectra, several thin-films of F<sub>4</sub>TCNQ doped (20 mol%) and undoped MTDATA are processed and heated for 10 min at different temperatures (70°C, 100°C, 130°C). The films are measured after cooling down to room temperature. In this way the reversibility at higher temperatures is probed.

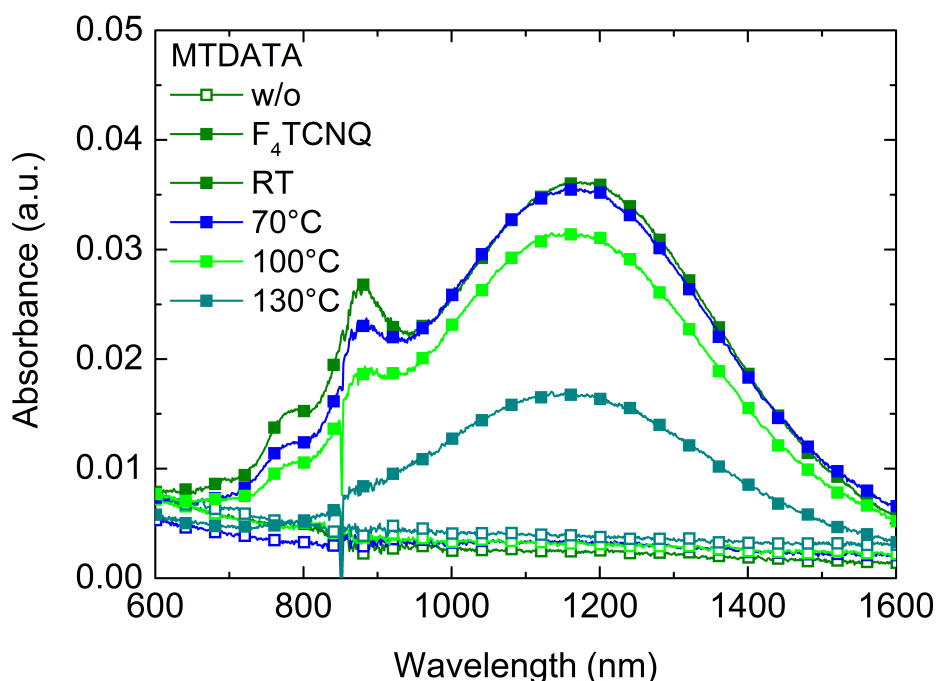


**Figure 5.40.** Vis-NIR spectra of MTDATA:F<sub>4</sub>TCNQ (20 mol%) films at different temperatures. The absorption band between 600 and 1600 nm irreversibly decreases with increasing temperature.

In figure 5.40, the spectra of undoped MTDATA films do not differ much at the different temperatures. In contrast, the doped films show a significant decrease of the intensity of the absorption band between 600 and 1600 nm at temperatures above 70°C. At 130°C the band shows only half of the original intensity. Due to the fact that the films are cooled down before measuring a reestablishing of the original doped state is not reached anymore. This is in accordance with observation in the literature.[139] Li et al. showed that F<sub>4</sub>TCNQ evaporates from the sample at 150°C. Thus the crosslinking temperature of the used hole-transport polymers should be as low as possible to ensure an effective doping.

### 5.4.3. Summary

In conclusion, 1-alkynyl ethers can be used in side-chain copolymers as crosslinkers without significant changes in the optoelectronic film properties. A major challenge are the demanding crosslinking conditions which hamper an effective doping with the dopants  $F_4$ TCNQ and HATCN<sub>6</sub>. One mitigation plan would be to use dopants that are temperature stable above 180°C. Another option would be to lower the glass transition temperature of the side-chain polymers which would also reduce the crosslinking temperature.

## 5.5. Sample preparation

All used materials and their purities are listed in appendix A.2. All chemicals have been used without further purification. The used PEDOT:PSS formulation (Clevios P VP AI 4083) was purchased from Heraeus.

Poly-[4-*N,N*-bis[4-(*N,N*-phenyl(*m*-tolyl)amino]phenylamino)vinylphenyl] (PMTDATA) and poly-[*N*-phenyl-*N,N'*-di(*m*-tolyl-*N'*-(4-vinylphenyl)biphenyl-4,4'-diamine)] (PTPD) were synthesized by the group of Dr. Krüger from the Fraunhofer Institute for Applied Polymer Research in Potsdam (IAP) according to the literature.[55] For the crosslinkable version, additionally, an alkynylether connected to a styrene was statistically copolymerized by the Fraunhofer IAP with the previous monomers from the side-chain-polymers.

All processing and optoelectronic characterization processes were realized in a clean-room (class 1000 - 100 000). This was necessary because organic layers often exhibit thicknesses of only a few ten nanometers. Thus a dust grain may lead to short cuts and destroy the device. Therefore, substrates were cleaned for 10 minutes in acetone and 2-propanol in an ultrasonic bath. Then they were treated with oxygen plasma to remove residual organic material and, in some cases, to enhance the adhesion of PEDOT:PSS (Clevios P VP AI 4083). As substrates either pure glass or structured ITO coated glass substrates ( $R_{\square} = 13 \Omega/\square$ ) were used. Unless mentioned otherwise all further processing and characterization steps have been carried out in nitrogen atmosphere in a glovebox system.

MTDATA, PMTDATA, TPD, PTPD,  $F_4$ TCNQ and HATCN<sub>6</sub> were dissolved with different concentrations in tetrahydrofuran (THF). These initial solutions were mixed to yield matrix:dopant solutions with different molecular dopant concentrations. For ultraviolet-visible-near infrared (UV-vis-NIR), photoelectron yield spectroscopy in air (PESA), electron paramagnetic spin resonance (EPR) measurements and the fabrication of OLEDs, a concentration of 5 g/L was used, for hole-only devices and charge extraction by linear increasing voltage (CELIV), 20 g/L were used. The dopant concentrations are mentioned at the respective graphs.

For impedance measurements, 30 nm of doped and undoped MTDATA and the corresponding polymer was sandwiched between an ITO covered glass and a 100 nm thick evaporated silver electrode. The measurement setup consists of a potentiostat PGSTAT302N including a FRA32M impedance module from Metrohm Autolab B.V. Impedance spectroscopy was measured by Daniel Bahro.

The HOMO levels of the same films as used for UV-vis-NIR-measurements were measured using an AC-2E by Riken Keiki at a beam power of 10 nW.

All measurements were performed using a Cary 5000 by Agilent Technologies under ambient conditions. The MTDATA:F<sub>4</sub>TCNQ and PMTDATA:F<sub>4</sub>TCNQ solutions were heated by a CARY Dual Cell Peltier Accessory. The solutions were measured in quartz cuvettes of 1 cm thickness against a cuvette filled with pure solvent as a reference. In addition spincoated organic thin-films with a thickness of around 30 nm (1000 rpm, 45s, 4000 rpm, 3 s) were measured on glass substrates against a glass reference.

The EPR experiments in this work have been realized in cooperation with the group of Professor Jan Behrends at the Joint EPR Lab at the FU Berlin measured either by Kelvin Yao (depending on the systems either the first test measurements or the tests for reproducibility for MTDATA/PMTDATA matrix:dopant combinations), or by Nils Jürgensen during his master thesis (TPD/PTPD matrix:dopant combinations) or by myself (depending on the systems either the first test measurements or the tests for reproducibility for MTDATA/PMTDATA matrix:dopant combinations) under supervision of Professor Jan Behrends.

To measure electrical conductivities, symmetric hole-only devices with a Ag (20 nm)/MoO<sub>x</sub> (10 nm)/HTL/MoO<sub>x</sub> (10 nm)/Ag (100 nm) architecture were built comprising undoped and electrically doped matrix layers. Ag and MoO<sub>x</sub> were thermally evaporated whereupon the MoO<sub>x</sub> layer ensures the ohmic contact to the silver electrode. The doped and undoped matrix solutions with varying dopant concentrations were spin coated from THF (20 g/L, 1000 rpm, 45 s, 4000 rpm, 3s) which was stirred overnight. J-V curves were recorded using a source measure unit (Keithley 238).

The material under study is sandwiched between two different electrodes, and thus current can only flow in one direction and is blocked in the other. To guarantee an ohmic contact to one electrode, a highly doped layer (in this case PEDOT:PSS) is implemented between the electrode and the matrix. In this work, metal-insulator-semiconductor charge extraction by linear increasing voltage (MIS-CELIV) was used to measure conductivities. Here, an insulation layer between the matrix and the other electrode prevents transport

of charge carriers through the blocking electrode. Hence higher voltages for extraction can be used. The MIS-CELIV samples employed an ITO/PEDOT:PSS/HTL/MgF<sub>2</sub>/Al architecture. 30 nm PEDOT:PSS (Clevios P VP AI 4083) was spin coated on the ITO glass (500 rpm, 3s, 4000 rpm, 25 s) and annealed at 150 °C for 10 min. The matrix materials were processed as described for hole-only devices. 50 nm magnesium fluoride (MgF<sub>2</sub>) as insulator and 200 nm Al were evaporated as electrode. MIS-CELIV measurements were carried out after device encapsulation in ambient atmosphere in the dark partly by Nils Jürgensen during his master thesis.[132] An Agilent 33522A arbitrary waveform generator was used to apply the triangular voltage pulse which was amplified by a Linear Technology LT1210 operational amplifier with an input impedance of 10 MΩ. The oscilloscope input signal (voltage) was amplified to the range of ±15 V. The current signal was amplified by a Femto DHPA-100 transimpedance amplifier with a gain of 104 V/A and recorded by an Agilent DSO 6102A digital storage oscilloscope with a load resistance of 50 Ω.

Samples were prepared by spincoating doped and undoped matrices (5 g/L, 1000 rpm, 45 s, 4000 rpm, 3 s) on ITO coated glass substrates. For all samples the ITO was contacted by silver conductive paint after scratching one edge free of organic material. They were measured by Stefan Reich, Stefan Gärtner and Tobias Leonhard by PF-TUNA in peak-force-tapping mode on a Bruker Dimension ICON under nitrogen in a glovebox utilizing a PF-TUNA tip.

Finally, doped organic material have been tested in organic light emitting diodes. To investigate the influence of the polymerization of the hole injection materials OLEDs were build using an ITO/HIL (30 nm)/HTL (10 nm)/ matrix:Ir(ppy)<sub>3</sub> (20 nm)/BPhen:Ir(ppy)<sub>3</sub> (20 nm)/BPhen (25 nm)/LiF (1 nm)/Al (200 nm) architecture. A HIL layer of doped and undoped matrix was applied on top of the ITO (1000 rpm, 45 s, 4000 rpm, 3 s). As a reference an evaporated doped matrix layer with the same thickness was used. All following layers were evaporated to ensure comparability and reproducibility. On top of the solution processed layer first a thin matrix layer was evaporated to prevent quenching at the interface of the doped layers. For light emission a double emission layer was used. Therefore, the phosphorescent emitter was thermally co-evaporated with the matrix with a ratio of 6 mol% and afterwards with BPhen with a ration of 3 mol%. As electron transport and hole blocking layer, pure BPhen was applied. As counter electrode, a thin LiF layer followed by Al was used.

For the investigation of the influence of the crosslinking group and the crosslinking conditions OLEDs with an ITO/PEDOT:PSS (30 nm)/HTL (10 nm)/CBP:Ir(ppy)<sub>3</sub> (35 nm)/TPBi (20 nm)/LiF (1 nm)/Al (200 nm) were built. As HIL PEDOT:PSS was diluted with water (1:1, v:v), spin cast onto the substrates (4000 rpm, 30 s) and annealed (150°C,

10 min) to remove residual water. The non-crosslinkable and crosslinkable polymers (2 g/L, toluene) were deposited on top (1000 rpm, 45 s; 4000 rpm, 3 s). Half of the samples were annealed above the cross-linking temperature on a hotplate (XMTDATA: 160°C, 30 min; XTPD: 180°C, 10 min), whereas the reference samples were dried only in a vacuum oven (80°C, 15 min). All following layers were evaporated to ensure comparability and reproducibility. Atop the HTL the phosphorescent emitter Ir(ppy)<sub>3</sub> was co-evaporated with the common host CBP. TPBi was applied as electron transporting and hole blocking layer, followed by the counter electrode LiF/Al.

All current density-voltage and current-voltage characteristics were recorded on a source measurement unit (Keithley 238). The OLED device luminance was calculated from the emission spectrum. The spectrometer was calibrated with a secondary standard calibration halogen lamp (Philips FEL-1000 W). Optoelectronic characteristics were calculated from the electrical and optical properties assuming Lambertian light distribution.

## 6 | n-Doped thin-films, processed from solution

n-Doping is much more challenging than p-doping due to the requirement of the dopants to exhibit a HOMO higher than the LUMO of the matrix.<sup>†</sup> This often results in highly reactive and oxygen-sensitive dopants. One option to achieve n-doping is the use of alkali metals due to their low work functions. Another option is the in situ formation of the reactive form of the dopant which is employed by doping with cationic dyes. Both reactions are known from the literature for evaporated films[32, 33, 36] and therefore a reasonable starting point for solution processed n-doping.

In this chapter first, n-doping of an organic semiconductor with sodium is transferred to solution processing. Charge carrier transfer to the dopant is characterized by UV-vis and EPR spectroscopy and the shift of the Fermi energy is measured by KPFM. Sodium doped TPBi films are also implemented as electron extraction layers (EELs) in organic solar cells and showed superior performance compared to undoped TPBi layers, if commonly used ZnO is replaced. The integrity of the undoped and doped TPBi layers after processing the absorber layer from *o*-xylene solution on top is verified by ToF-SIMS. These measurements also show no diffusion of sodium in the stack over several months.

In the second part, different fullerenes are n-doped with rhodamine B, processed from solution. The doping and the doping efficiencies are characterized by EPR measurements under illumination. By replacing ZnO an improved performance of organic solar cells comprising doped films compared to non-doped films is observed.

---

<sup>†</sup>Parts of the following section are reprinted (and adapted) from T. Schneider, J. Czolk, D. Landerer, S. Gärtner, A. Pütz, M. Bruns, J. Behrends, A. Colsmann, submitted to *J. Mater. Chem. A* **2016**, with permission of Royal Society of Chemistry and T. Schneider, S. Gärtner, B. Ebenhoch, J. Behrends and A. Colsmann, submitted to *Synthetic Metals* **2016**, with permission of Elsevier. T. Schneider designed and conducted all experiments unless otherwise stated and wrote the manuscript. J. Czolk measured UV-vis of the TPBi solutions and did the preparatory work together with A. Pütz, D. Landerer developed the efficient additive-free absorber system, S. Gärtner measured KPFM and developed the synthesis of the unstabilized P3HT:ICBA nanoparticles and M. Bruns measured ToF-SIMS. J. Behrends carried out the repeating EPR measurements of the doped fullerenes and helped with the discussions regarding EPR. B. Ebenhoch helped with discussion regarding solar cells. A. Colsmann motivated and supervised the project and contributed to scientific discussions.

## 6.1. Selection of electron transport materials and suitable dopants

In order to avoid losses in the open-circuit voltage ( $V_{OC}$ ) of organic solar cells, as a rule of thumb, EELs with Fermi energies higher than or equal to the electron affinity of the fullerene acceptor have to be chosen. Therefore, as electron extraction layers, TPBi and different soluble fullerenes (PCBM and the bisadducts bis-PCBM and ICBA) are chosen due to their various applications in organic electronic devices as efficient electron transporting layers, that can also block holes successfully.[155, 156]

As mentioned before, in case of n-doping, dopants with HOMO energies higher than the LUMO energies of the electron transport materials are required. Therefore, sodium, with an ionization energy of about 2.75 eV,[97] is a suitable n-dopant for TPBi, having a LUMO energy of about -2.8 eV.[157] Thus 3s valence electrons of sodium can transfer to TPBi, resulting in an electron excess on the TPBi matrix.

In case of doping with cationic dyes, doped  $C_{60}$  is a common electron extraction layer in vacuum processed organic solar cells. Unfortunately its low solubility in most common solvents, does not allow to readily transfer of the layer deposition to solution processing. Due to their enhanced solubility, PCBM, bis-PCBM and ICBA are the most used functionalized fullerene derivatives in solution processable organic optoelectronic devices. However, the functionalization of fullerenes by solubilizing groups changes the energetic levels of the fullerene. The more adducts, the higher the LUMO energy of the fullerene. Whereas  $C_{60}$  exhibits a LUMO energy of -4.3 eV, -3.91 eV has been reported for PCBM, -3.7 eV for bis-PCBM and -3.7 eV for ICBA.[158–161] As a consequence, this change of LUMO energy does affect the number of electrons transferred from the dopants to the matrix molecules.

Rhodamine B in its ground state does not n-dope fullerenes. When activated by heat or light, it is converted in its leuco form and an electron transfer to the fullerenes occurs.[42] The chemical structures of the used matrices and dopants (except sodium) are depicted in figure 6.1.



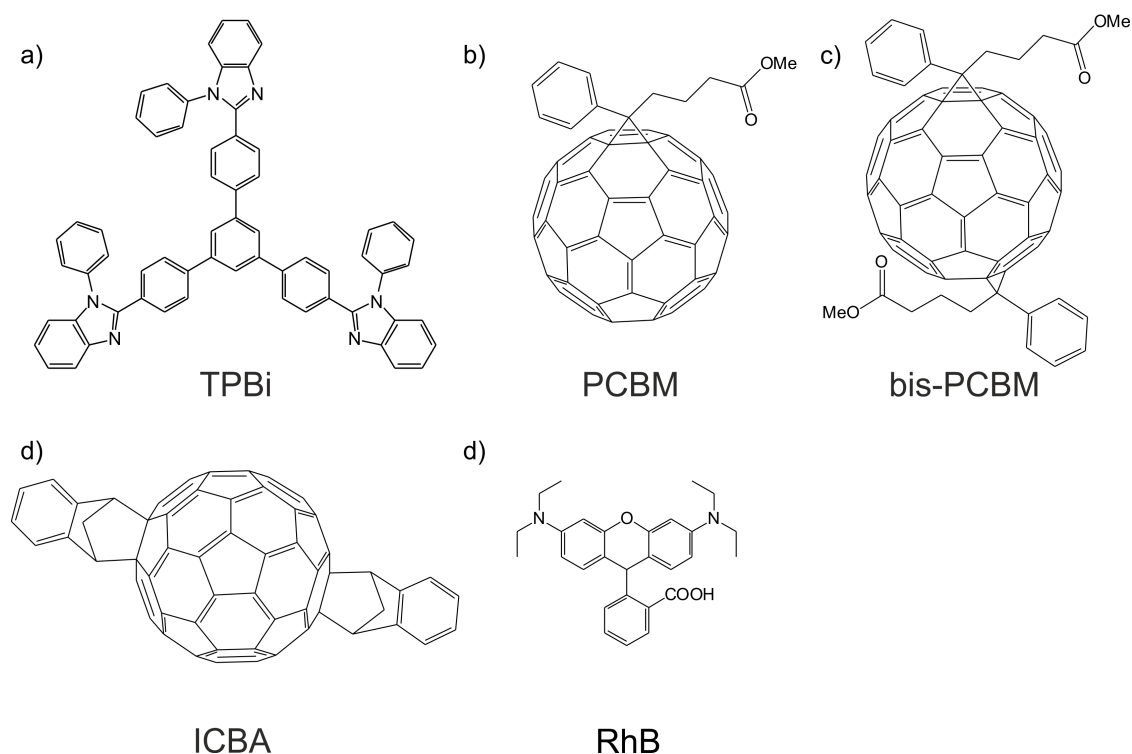


**Figure 6.1.** Chemical structures of all investigated electron transport materials and the dopant RhB in its active leuco form.

## 6.2. n-Doping by employing alkali metals

Whereas alkali metal doping is widely used in vacuum deposited organic semiconductor devices, its applicability by wet processing is widely unexplored, since neat sodium does not dissolve in common processing agents. Therefore, in this chapter, a process to dissolve alkali metals in a solution of a semiconductor in a commonly used organic solvent is introduced. The reaction of this semiconductor, here TPBi, with the alkali metal, in this case sodium, is investigated in solution by UV-vis and NMR spectroscopy. The thin-films are further investigated by EPR spectroscopy to characterize the charge carrier transfer from sodium to TPBi and the doping efficiencies. KPFM measurements provide access to the shift of the Fermi energy towards the LUMO of TPBi. In the end, solar cells are built comprising undoped and sodium doped TPBi as electron extraction layers. The integrity of the EELs in the stack after processing the active layer on top is demonstrated by ToF-SIMS measurements.

### 6.2.1. Solution processing of alkali metal doping

Adding a piece of sodium to a 10 g/L solution of TPBi in toluene at room temperature, the clear TPBi/toluene solution turns red (see figure 6.2, inset).

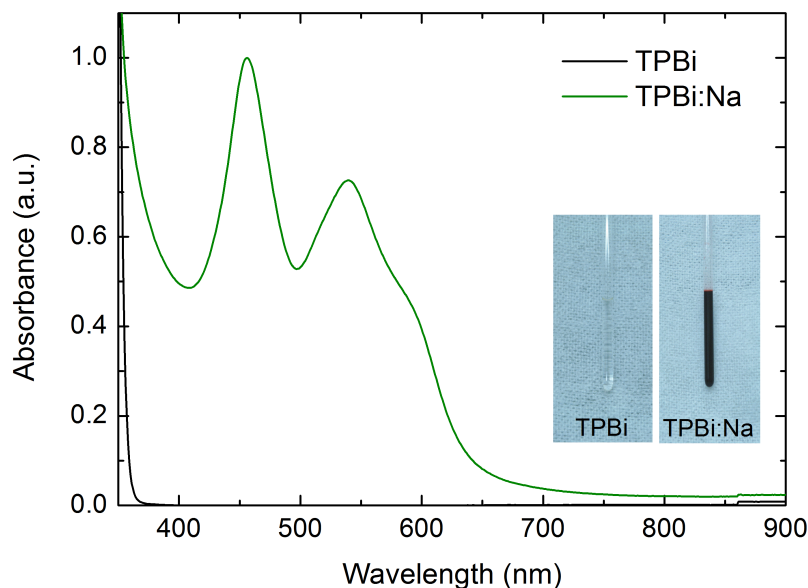


**Figure 6.2.** Normalized UV-vis absorbance spectra of neat TPBi/toluene and TPBi<sup>-</sup>/Na<sup>+</sup>/toluene solutions. Upon addition of sodium, absorption bands between 350 and 650 nm occur, indicating the formation of new polaronic states through transfer of the 3s electrons from sodium to TPBi.

The respective UV-vis absorption spectrum depicted in figure 6.2 shows additional absorption bands that hint towards new polaronic states in the reduced TPBi. These bands are not observed in neat TPBi solution. After exposing the TPBi<sup>-</sup>/Na<sup>+</sup>/toluene solution to air, the solution turns clear again which shows that the reduction of TPBi molecules is reversible.

When working with sodium and polymerizable materials one has to keep in mind that it is usually used as initiator in anionic polymerizations. Thus NMR spectra of the TPBi/toluene and the TPBi<sup>-</sup>/Na<sup>+</sup>/toluene solution are recorded, to explore changes of the molecular conformation after reducing the TPBi molecules. The resulting spectra are shown in figure 6.3.

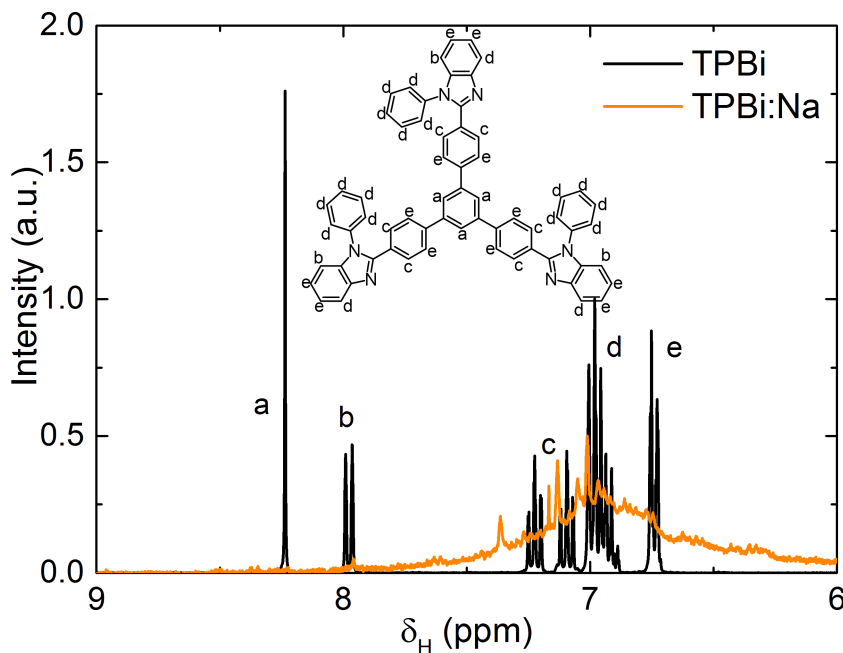


**Figure 6.3.** NMR spectra of neat TPBi and TPBi<sup>-</sup>:Na<sup>+</sup> solutions in toluene-D<sub>8</sub>. The spectrum of undoped TPBi exhibits sharp peaks whereas the peaks of the doped TPBi are much broader. This broadening is attributed to an oligomerization of TPBi molecules induced by the electron transfer from sodium to TPBi. For better visibility, the spectra have been plotted using arbitrary units.

Upon doping, we observed a broadening of all peaks which can be attributed to an oligomerization of the TPBi molecules, initiated by an electron transfer from sodium to TPBi. Due to the decreasing reactivity with increasing chain length, only oligomers of a few repeating units are formed which are still soluble in toluene. We note that the oligomerization of TPBi in solution does not affect the principle electron excess on the TPBi molecules.

## 6.2.2. Analysis of the doping process and its efficiency

After the characterization of the TPBi<sup>-</sup>/Na<sup>+</sup>/toluene solution, the effect of doping on the solid TPBi:Na bulk and, for reference, neat TPBi samples is investigated to evaluate the applications of n-doped materials as thin layers in organic electronics.

### 6.2.2.1. Measurement of the number of unpaired spins with EPR spectroscopy and calculation of doping efficiencies

To further investigate the charge carrier transfer from sodium to TPBi, the number of unpaired electrons within the dry thin-films is measured by EPR.

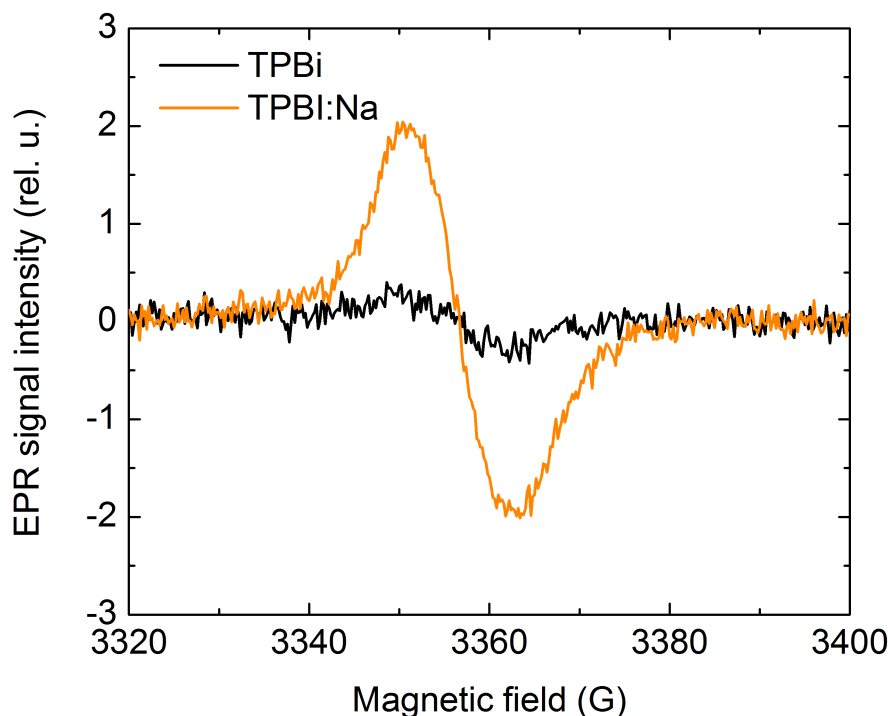


**Figure 6.4.** EPR spectra of neat TPBi and TPBi:Na films. Whereas undoped TPBi exhibits only a weak EPR signal, the doped TPBi:Na thin-film shows a strong signature of unpaired spins which can be attributed to doping-induced electrons and hence to *n*-doping of TPBi.

As depicted in figure 6.4, films of undoped TPBi show weak background signatures of unpaired electrons. However, for doped thin-films deposited from TPBi<sup>-</sup>/Na<sup>+</sup>/toluene solution, a significantly stronger EPR signal can be detected, indicating the presence of doping-induced electrons in the TPBi layer. It can be ruled out that the signal is caused by residual Na-atoms. On the one hand, residual sodium is removed before preparing the thin-films. On the other hand, sodium signals are expected at different magnetic fields. The absolute number of spins per sample is calculated by double-integration of the EPR signal and comparison to a 4-hydroxy-TEMPO-reference sample with a known number of spins in the same way as the *p*-doped matrices before. Spin concentrations are calculated by dividing the total amount of measured spins by the sample volume, and the doping efficiencies are calculated by neglecting the number of sodium atoms and calculation of the fraction of *n*-doped TPBi molecules. The concentration of unpaired spins increases from  $1 \times 10^{16} \text{ cm}^{-3}$  in case of undoped TPBi by more than one order of magnitude to  $4 \times 10^{17} \text{ cm}^{-3}$  in case of TPBi:Na. This spin concentration corresponds to 1 unpaired electron per 5000 TPBi molecules. During the oligomerization generated electrons are used in the chemical bond between monomer units. Therefore the actual number of electrons transferred from sodium to TPBi is higher, because it is calculated on the amount of monomers not oligomers.

### 6.2.2.2. Shift of the Fermi energy upon *n*-doping

To investigate the effect of Na-doping on the physical properties of TPBi films, thin-films from both the undoped and sodium doped TPBi solution are spin cast and the surface potentials of the films on ITO are measured by KPFM. Upon Na-doping, the surface potential of the TPBi on ITO shifts from -4.40 eV (undoped TPBi) to -3.55 eV, indicating a Fermi energy shift towards the TPBi LUMO, as expected.

This change should affect the  $V_{OC}$  of organic solar cells, when incorporated as electron transport layers. In general, a built-in field smaller than the energetical difference between the HOMO of the absorber polymer and the LUMO of the fullerene will reduce the  $V_{OC}$ . [99, 162, 163] In contrast, a difference of the transport layer work functions larger than mentioned HOMO(Donor)-LUMO(Acc.) difference ensures a full  $V_{OC}$ .

### 6.2.3. Implementation of *n*-doped layers in organic solar cells

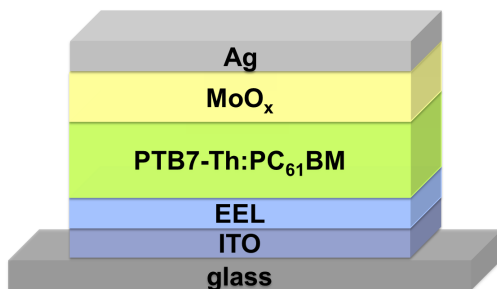


**Figure 6.5.** Device architecture of solar cells: ITO/EEL/PTB7-Th:PCBM/MoO<sub>x</sub>/Ag.

To study the effect of the *n*-doped EELs, organic solar cells featuring a ITO/EEL/PTB7-Th:PCBM/MoO<sub>x</sub>/Ag device architecture are built (see figure 6.5), employing a 30 nm EEL from either neat TPBi, sodium doped TPBi or, for reference, nanoparticulate ZnO, the latter being widely used for electron extraction and allowing comparison with the literature. The 90 nm PTB7-Th:PCBM photo-active layer are deposited from *o*-xylene, intentionally omitting processing additives such as 1,8-diiodooctane or *p*-anisaldehyde, to avoid chemical reactions with the sodium in the underlying EEL.

The integrity of the layer stack and in particular the presence of an intact TPBi or TPBi:Na EEL is studied in a ToF-SIMS analysis. Therefore, the devices are successively ablated with a Cs<sup>+</sup> ion beam while the resulting positive and negative charged ions are detected. The ToF-SIMS signals and the corresponding layers of the solar cell are depicted in figure 6.6.

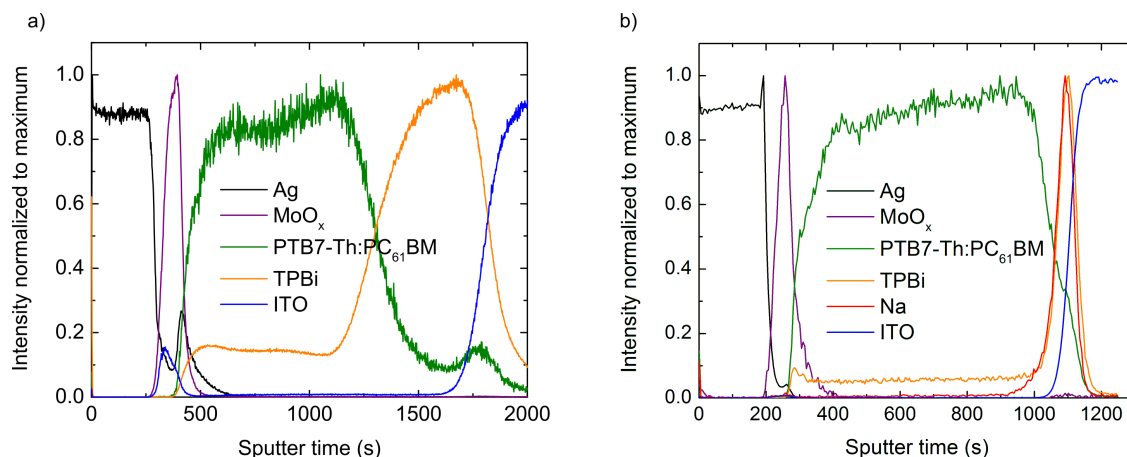


**Figure 6.6.** ToF-SIMS measurements on a typical solar cell comprising a (a) TPBi or a (b) TPBi:Na layer. Ag ( $\text{CsAg}^+$ ),  $\text{MoO}_x$  ( $\text{CsMo}^+$ ) and Na ( $\text{CsNa}^+$ ) are detected in the positive polarity spectrum. PTB7-Th:PC<sub>61</sub>BM ( $\text{CS}^-$ ), TPBi ( $\text{C}_2\text{N}_2^-$ ) and ITO ( $\text{In}_2\text{O}_2^-$ ) are detected in the negative polarity spectrum. The co-location of TPBi and TPBi and Na proves the integrity of the doped and undoped TPBi electron extraction layer between the photo-active PTB7-Th:PC<sub>61</sub>BM layer and the ITO cathode.

Starting the analysis from the Ag top electrode ( $\text{CsAg}^+$ ), the sequentially identified layers are the  $\text{MoO}_x$  layer ( $\text{CsMo}^+$ ), the photo-active PTB7-Th:PC<sub>61</sub>BM layer ( $\text{CS}^-$ ), the TPBi or TPBi:Na EEL ( $\text{C}_2\text{N}_2^-$ ,  $\text{Na}^+$ ) and the ITO bottom electrode ( $\text{In}_2\text{O}_2^-$ ). The  $\text{CsNa}^+$  signal provided information about the sodium content throughout the layer stack. For better readability, all curves are normalized to their respective maxima, leading to a somewhat higher background noise of the  $\text{C}_2\text{N}_2^-$  signal.

The  $\text{C}_2\text{N}_2^-$  signal in figure 6.6 a and b shows that the undoped TPBi and sodium doped TPBi layer prevail between the ITO and the active layer in the layer stack, indicating an intact EEL even after spincoating the absorber on top from *o*-xylene solution. In the doped TPBi layers, the sodium peak is found not only coinciding with the TPBi layer, indicating an intact TPBi:Na EEL. It is also observed that (over a period of 4-6 month) sodium did not diffuse within the device which is an often observed process, e.g., for the smaller alkali metal lithium that is detrimental to the device performance.[40]

After evidencing the integrity of the electron extraction layer including the position of sodium, the organic solar cells are characterized by means of current density-voltage measurements.

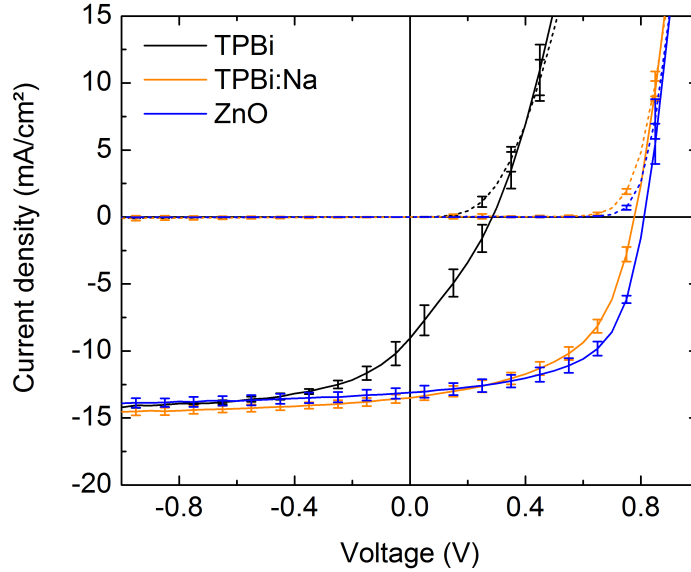


**Figure 6.7.** Typical J-V curves of glass/ITO/EEL/PTB7-Th:PC<sub>61</sub>BM/MoO<sub>x</sub>/Ag solar cells under AM1.5 illumination. The solar cell with a TPBi:Na EEL exhibits a higher  $V_{OC}$  and FF than the solar cell comprising neat TPBi and almost matches the performance of the reference solar cell with an EEL from ZnO.

Figure 6.7 depicts the corresponding J-V curves. The key performance data open-circuit voltage ( $V_{OC}$ ), short-circuit current density ( $J_{SC}$ ), fill factor (FF) and power conversion efficiency (PCE) are summarized in Table 6.1. Even without additives, the reference PTB7-Th:PCBM cells with ZnO EELs yielded here efficiencies of almost 7%, thereby outperforming additive-free, literature-known solar cells.[51, 164]

**Table 6.1.** Averaged key-performance data of organic solar cells. The PCE in parentheses represent hereo devices.

	$V_{OC}$ (mV)	$J_{SC}$ (mA/cm <sup>2</sup> )	FF (%)	PCE (%)
TPBi	290±20	9.0±1.1	28±0.8	0.7±0.16 (0.90)
TPBi:Na	777±5	13.5±0.3	54±1.4	5.6±0.3 (6.1)
ZnO	812±6	13.1±0.4	60±2	6.4±0.3 (6.8)

Under reverse bias and hence upon field-assisted charge carrier extraction, all solar cells exhibit the same saturation current density which indicates about equal photo-generation of charge carriers in all three devices. However, solar cells comprising EELs of undoped TPBi yielded only moderate PCEs below 1%, mainly being limited by the  $V_{OC} = 290$  mV and the  $FF = 28\%$ . Due to the Fermi energy of undoped TPBi (-4.40 eV) which is lower than the LUMO of PCBM (-3.91 eV), the built-in field is reduced.[159] This results in a

loss in  $V_{OC}$  by around 500 mV. In contrast, the built-in field for devices exhibiting doped TPBi layers is significantly increased due to the shift of the Fermi energy of TPBi:Na to 3.55 eV. Hence, the full  $V_{OC} = 780$  mV is reached. Additionally, in case of undoped TPBi, a barrier of around 1 eV is created due to the large difference between the LUMO of PCBM (3.91 eV) and the LUMO of TPBi (2.8 eV)[157]. This hampers the electron transfer of photo-generated electrons on PCBM to the cathode. Therefore, the cells with an undoped EEL exhibit a  $J_{SC}$  of only 9.0 mA/cm<sup>2</sup>. Upon doping, the Fermi energy shifts to the LUMO, as measured by KPFM. This results in a thin barrier which can be tunneled by the charges and enables efficient charge carrier extraction. Thus in solar cells comprising doped EELs, much higher  $J_{SC}$  of 13.5 mA/cm<sup>2</sup> can be achieved compared to solar cells comprising undoped films. In fact, they are even comparable to the ZnO reference cells ( $J_{SC} = 13.1$  mA/cm<sup>2</sup>). Based on the measured  $J_{SC}$  and the FF of 54%, in case of sodium doped TPBi, a hero PCE = 6.1% is reached which is only 10% (rel.) below the performance of the ZnO reference device.

#### 6.2.4. Summary

Sodium is soluble in a TPBi-toluene solution, where it transfers 3s electrons into the LUMO of the organic semiconductor. The latter is proven by EPR. The electron transfer also initiates the formation of TPBi-oligomers. Due to this side reaction and the unknown size and amount of the oligomers, an unambiguous doping efficiency cannot be calculated. The shift of the Fermi energy upon doping is nicely shown in KPFM measurements. Implemented in organic solar cells as electron extraction layers, the solar cells comprising doped layers show an improved performance in comparison to solar cells comprising undoped EELs. Due to the efficient doping, the key performance parameters are similar to organic solar cells with commonly used ZnO EELs.

#### 6.2.5. Sample preparation

All used materials and their purities are listed in appendix A.2. All chemicals have been used without further purification. Toluene was dried over sodium (Na) to remove all residual water and oxygen. Sodium was cut in toluene under nitrogen atmosphere and cleaned with toluene from residual mineral oil.

The ZnO layers were applied from a ZnO nanoparticle dispersion in isopropanol (Nano-grade N-10, 2.5 wt%) from Nanograde Ltd. As absorber polymer poly[[2,6'-4,8-di(5-ethylhexylthienyl)benzo[1,2-b;3,3-b]dithiophene][3-fluoro-2[(2-ethylhexyl)carbonyl]thieno[3,4-b]thiophenediyl]] (PTB7-Th) ( $M_w = 105$  kDa,  $\mathcal{D}_M = 2$ ) from 1-Material Inc was used.

All processing and optoelectronic characterization processes were realized in a clean-room (class 1000 - 100 000). This was necessary because organic layers often exhibit thicknesses of only a few ten nanometers. Thus a dust grain may lead to short cuts and



destroy the device. Therefore, substrates were cleaned for 10 minutes in acetone and 2-propanol in an ultrasonic bath. Then they were treated with oxygen plasma to remove residual organic material. As substrates either pure glass or structured ITO coated glass substrates ( $R_{\square} = 13 \Omega/\square$ ) were used. Unless mentioned otherwise all further processing and characterization steps have been carried out in nitrogen atmosphere in a glovebox system.

TPBi was dissolved (10 g/L) in dry toluene and sodium was added to the TPBi/toluene solution. After stirring the solution overnight, the solid sodium surplus was removed.

NMR spectra were measured by Silke Wolf on a Bruker Avance III Microbay 400 MHz. Toluene-D8 solutions of TPBi:Na or neat TPBi as reference sample were filled into NMR tubes under inert atmosphere and sealed using a blowtorch.

All measurements were performed using a Cary 5000 by Agilent Technologies under ambient conditions. The TPBi-solutions in sealed cuvettes have been measured by Jens Czolk using a Lambda 1050 by Perkin Elmer. The solutions were measured in quartz cuvettes of 1 cm thickness against a cuvette filled with pure solvent as a reference.

The EPR experiments in this work have been realized in cooperation with the group of Professor Jan Behrends at the Joint EPR Lab at the FU Berlin measured under supervision of Professor Jan Behrends.

AM-KPFM dual pass experiments were carried out by Stefan Gärtner on 30 nm films of undoped and doped films in tapping mode on the AFM described in the former chapter using Pt/Ir coated FMV-PT tip to measure the contact potential difference (CPD) between the tip and the sample. The CPD was referenced with the work function of highly oriented pyrolytic graphite (HOPG, -4.4 eV).[165]

Finally, doped organic material have been tested in organic solar cells. Solar cells were built on ITO coated glass substrates. The efficiency of the alkali metal doping was studied on a ITO/EEL (30 nm)/PTB7-Th:PCBM (90 nm)/MoO<sub>x</sub> (10 nm)/Ag (100 nm) architecture, comprising either undoped or sodium doped TPBi as electron extraction layer (EEL). ZnO was used as reference material. Sodium doped or undoped matrices were spin cast from solution (1000 rpm, 30 s, 4000 rpm, 3 s). ZnO was spin casted from nanoparticle dispersion (4000 rpm, 30 s) and thermally annealed on a hotplate (85°C, 10 min). PTB7-Th and PCBM were dissolved in *o*-xylene (1:1.5, w:w, 23 g/L) and stirred overnight at 85°C. The warm solution was spin cast (1500 rpm, 60 s) on top of the electron extraction layer. As counter electrode MoO<sub>x</sub>/silver was thermally evaporated through a shadow mask defining the photo-active area of the solar cell (3 × 3.5 mm<sup>2</sup>).

J-V curves were recorded on a source measure unit (Keithley 238) under illumination from a spectrally monitored solar simulator (Oriel 300 W, 1000 W/m<sup>2</sup>, ASTM AM 1.5G), calibrated by a KG5 filtered silicon reference cell (91150-KG5, Newport). The sample edges were masked to avoid light-incoupling through substrate modes.

Time of flight secondary ion mass spectrometry was performed on a TOF.SIMS5 instrument (ION-TOF GmbH, Münster, Germany) by Dr Michael Bruns at the Institute for applied Materials - Energy Storage Systems (IAM) at the KIT. It is equipped with a Bi cluster liquid metal primary ion source and a non-linear time of flight analyzer. The Bi source was operated in "bunched" mode providing 1 ns Bi<sub>3</sub><sup>+</sup> ion pulses at 25 keV energy, an analyzed area of 100 × 100 μm<sup>2</sup>, and a lateral resolution of approx. 4 μm. Negative polarity spectra were calibrated on the C<sup>-</sup>, C<sub>2</sub><sup>-</sup>, C<sub>3</sub><sup>-</sup>, and C<sub>4</sub><sup>-</sup> peaks. Positive polarity spectra were calibrated on the C<sup>+</sup>, CH<sup>+</sup>, CH<sub>2</sub><sup>+</sup>, and CH<sub>3</sub><sup>+</sup> peaks. Sputter depth profiles were performed using a 1 keV Cs<sup>+</sup> ion beam and a raster size of 500×500 μm<sup>2</sup>. All spectra were normalized to their highest peak.

## 6.3. *n*-Doping by employing cationic dyes

The second process for *n*-doping, namely the doping with cationic dyes, is also only known from vacuum processed devices. During evaporation the dye converts into its leuco form which is crucial to act as an electron donor, is done during the evaporation step.

In this chapter, soluble fullerenes are doped with RhB from solution. The transformation of the cationic dye and therefore the doping process, is activated by illumination with white light. The doping process and doping efficiencies are characterized by EPR. To test the performance of the doped and undoped fullerenes in organic solar cells, the active layer is deposited from an ethanolic nanoparticle solution due to the solubility of the fullerenes in most common organic solvents. The stability of the electron extraction layers against EtOH is shown in UV-vis spectra of pristine and EtOH rinsed films. In the last part of the chapter, the key performance parameters of the organic solar cells comprising undoped and RhB doped EEL are analyzed and compared to the commonly used ZnO EEL.

### 6.3.1. Electrical properties

As discussed in chapter 3.5.2.3, the charge carrier transfer between the cationic dye and the fullerene is activated by illumination with white light. As already shown earlier, the number of transferred electrons and thus the doping efficiency can be derived from EPR measurements. Therefore, EPR measurements are carried out on RhB doped samples of different fullerene derivatives. The samples are measured in the dark and under illumination with white light. The corresponding EPR measurements are depicted in figure 6.8.

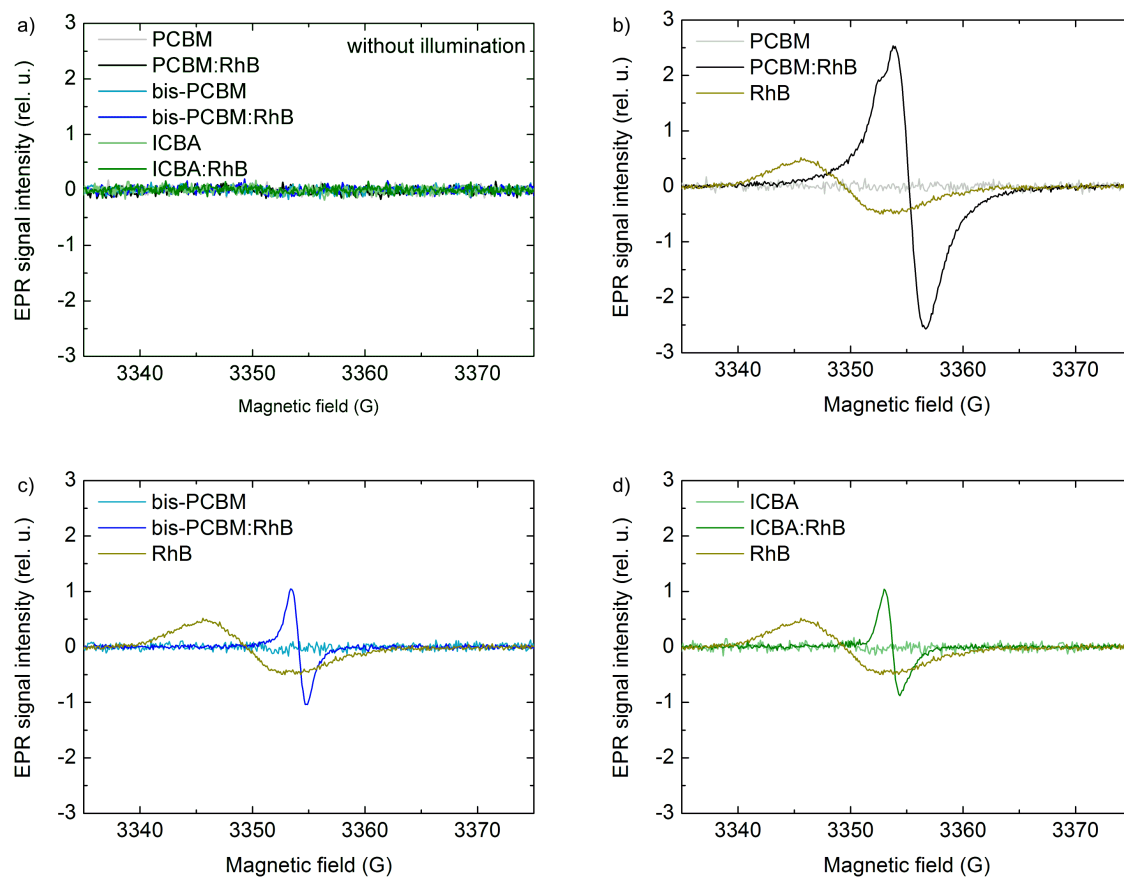


**Figure 6.8.** EPR spectra of doped fullerene layers (20 mol%), measured (a) without and (b)-(d) under illumination. In undoped reference fullerene layers, no EPR signals is observed. Upon doping with RhB, all data show strong signatures of unpaired spins. Neat RhB also shows a signature of unpaired spins that appears at lower magnetic field.

As depicted in figure 6.8 a no EPR signals are measured without illumination. In contrast, under illumination (see figure 6.8 b-d) no unpaired spins are observed in the spectra of all non-doped fullerenes. The RhB doped PCBM films showed the distinct signature of unpaired electrons, indicating electron transfer from RhB to the PCBM matrix, when illuminated with white light. Likewise, a signature of non-paired spins in bis-PCBM:RhB and ICBA:RhB is found yielding a lower intensity. The small shift of the EPR responses of both fullerene bis-adduct:RhB combinations towards lower magnetic fields can be attributed to small structural differences of the fullerene derivatives. Unpaired spins are also measured in neat RhB at lower magnitude after transformation to the leuco form at lower magnetic fields, the latter allowing to distinguish between excited electrons in RhB and electrons transferred to the fullerene derivatives.

To gain more quantitative information of the electron transfer yield, the absolute number of spins in the samples is calculated by double-integration of the EPR signals and comparison to a 4-hydroxy-TEMPO-reference sample as described before. All measured data and the derived electrical material properties are summarized in Table 6.2.

**Table 6.2.** Number of spins per volume and doping efficiency of the matrix-dopant combinations (20 mol%) as calculated from the EPR measurements.

	Total amount of spins	Spin concentration ( $\text{cm}^{-3}$ )	Doping efficiency (%)
PCBM	$1 \times 10^{12}$	$1 \times 10^{16}$	0
PCBM:RhB	$3 \times 10^{14}$	$3 \times 10^{18}$	0.3
bis-PCBM	$9 \times 10^{11}$	$9 \times 10^{15}$	0
bis-PCBM:RhB	$2 \times 10^{13}$	$2 \times 10^{17}$	0.02
ICBA	$2 \times 10^{12}$	$2 \times 10^{16}$	0
ICBA:RhB	$3 \times 10^{13}$	$3 \times 10^{17}$	0.02

The total amount of spins in the sample of illuminated undoped PCBM, bis-PCBM and ICBA is around  $10^{12}$  and the corresponding spin concentration around  $10^{16} \text{ cm}^{-3}$  which is close to the lowest detectable concentration. Upon doping with RhB, the spin concentration on the bisadducts, bis-PCBM or ICBA, increases by about one order of magnitude to  $2 \times 10^{17} \text{ cm}^{-3}$  and  $3 \times 10^{17} \text{ cm}^{-3}$ , respectively, yielding a doping efficiency of 0.02%. This effect is even more enhanced in PCBM:RhB where the spin concentration increases by two orders of magnitude to  $3 \times 10^{18} \text{ cm}^{-3}$ , yielding a doping efficiency of 0.3%, nicely reflecting the lower LUMO energy of PCBM versus bis-PCBM and ICBA. This leads to a more efficient electron transfer from the dopant RhB to the fullerene.

### 6.3.2. Implementation of *n*-doped layers in organic solar cells

In light of the successful implementation of  $\text{C}_{60}$ :RhB layers into vacuum processed organic solar cells, the implementation of *n*-doped PCBM:RhB, bis-PCBM:RhB and ICBA:RhB layers as EEL in solution processed solar cells is investigated. Since all three fullerene:RhB combinations are soluble in 1,2-dichlorobenzene and other organic solvents that are commonly used to deposit the polymer:fullerene bulk-heterojunction, an inverted device architecture is chosen, applying the bulk-heterojunction from nanoparticulate ethanol dispersion following processes described in the literature.[166] Today, such nanoparticle dispersion allow for the fabrication of 4% efficient organic solar cells, with P3HT:ICBA being the most efficient nanoparticulate photo-active absorber blend.

Whereas the fullerenes are insoluble in EtOH it is known, that RhB can be dissolved in this solvent. Thus, the stability of the undoped and RhB doped fullerene films against EtOH is investigated. Therefore, UV-Vis spectra of undoped and doped thin-films before and after rinsing with EtOH are measured (figure 6.9).

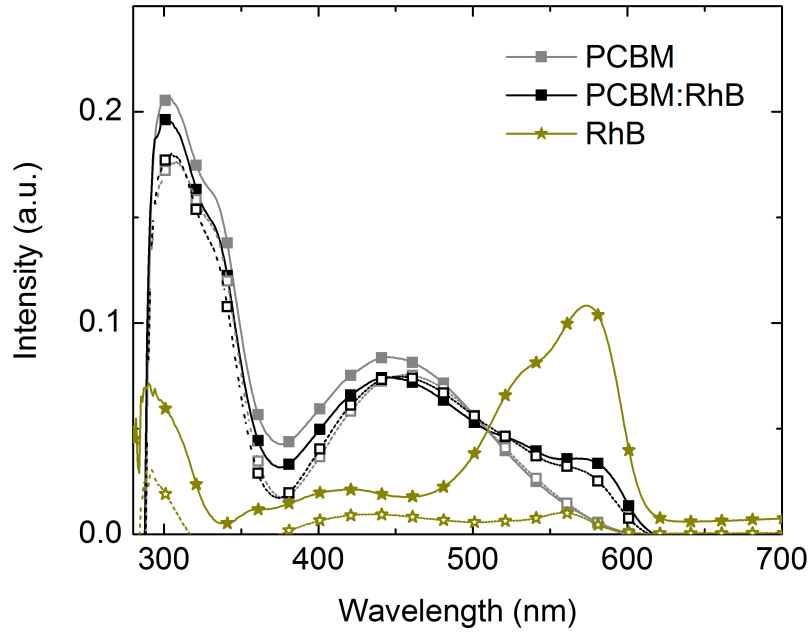


**Figure 6.9.** UV-Vis absorption spectra of 20 nm thin-films of undoped and doped bis-PCBM (20 mol%) on glass before (closed symbols) and after (open symbols) rinsing with EtOH, and the absorption spectrum of RhB for reference. Upon rinsing with EtOH, the absorption spectrum of PCBM and hence the layer thickness do not change. Although RhB is highly soluble in EtOH, rinsing hardly effects the PCBM:RhB layer, indicating that the PCBM matrix affixes the RhB dopant. Similar observations are made for PCBM:RhB and ICBA:RhB thin-films (see appendix A.3).

The UV-Vis spectra show that the intensity and absorption features of RhB of fullerene:RhB thin-films at 570 nm remain vastly unchanged even after rinsing with EtOH. Thus it can be assumed that the RhB is firmly affixed by the fullerene matrix.

According to the solubility of the absorber in *o*-xylene, an inverted ITO/EEL/P3HT:ICBA/PEDOT:PSS/Ag solar cell architecture, as depicted in figure 6.10 a, appears most appropriate. EELs from undoped and RhB doped PCBM, bis-PCBM, ICBA and, for reference, ZnO are implemented. The solar cells were measured two times, once directly after fabrication and again 10 days later. Due to shunt burning the second measurement exhibits slightly increased performance. The corresponding J-V curves and key performance parameters of the first measurement can be found in appendix A.4.

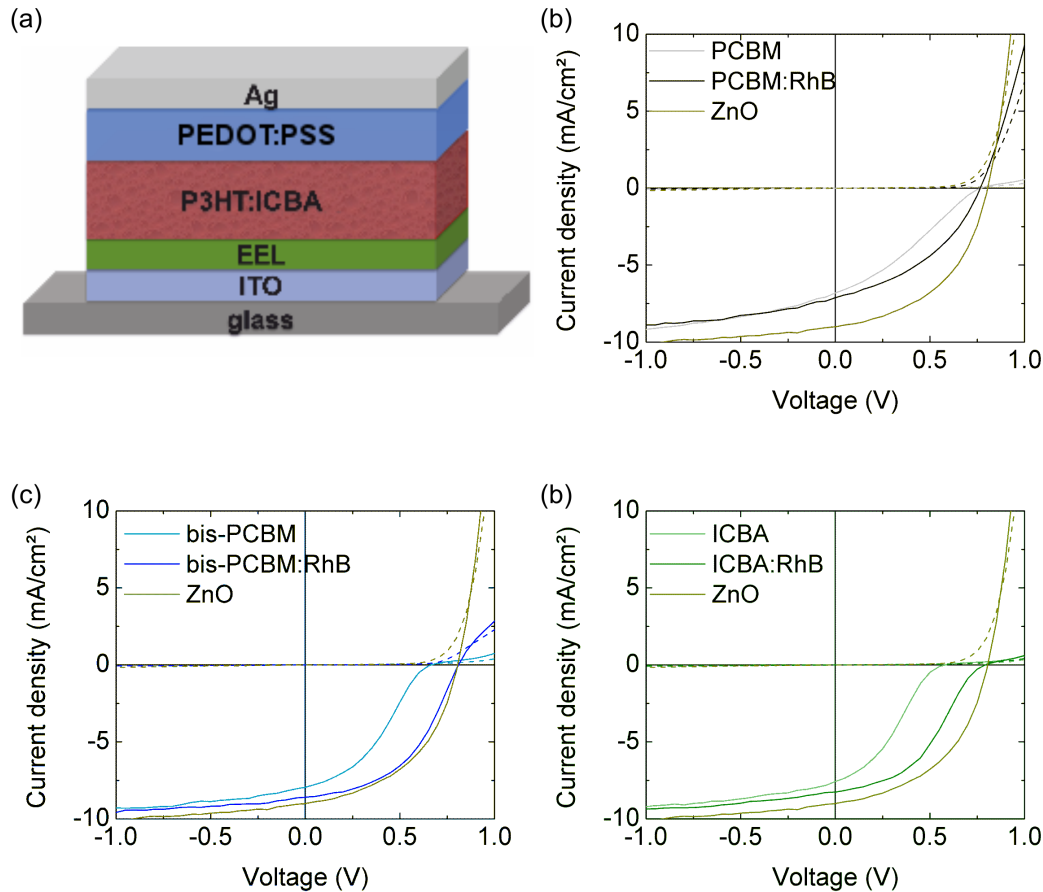


**Figure 6.10.** (a) Device architecture and (b)-(d) typical J-V curves of glass/ITO/EEL/P3HT:ICBA/PEDOT:PSS/Ag solar cells under AM1.5 illumination, comprising RhB doped EELs (20 mol%, closed symbols) versus non-doped EELs PCBM:RhB, bis-PCBM:RhB, ICBA:RhB.) remeasured after 10 days for the second time. Solar cells comprising state-of-the-art EELs from nanoparticulate ZnO are depicted for reference).

The corresponding current density-voltage curves are shown in figures 6.10 b-d. The key performance parameters - open-circuit voltage, short-circuit current density, fill factor and power conversion efficiency - are summarized in Table 6.3.

**Table 6.3.** Averaged key-performance data of organic solar cells remeasured after 10 days. The PCE in parentheses represent hero devices.

	$V_{OC}$ (mV)	$J_{SC}$ (mA/cm <sup>2</sup> )	FF (%)	PCE (%)
PCBM	779±6	6.7±0.3	31±1.0	1.6±0.08 (1.7)
PCBM:RhB	768±2	7.2±0.14	41±0.8	2.2±0.07 (2.4)
bis-PCBM	660±19	8.0±0.10	35±0.8	1.9±0.10 (2.0)
bis-PCBM:RhB	813±3	8.6±0.2	47±2	3.3±0.16 (3.5)
ICBA	590±30	7.6±0.3	31±1.7	1.4±0.15 (1.6)
ICBA:RhB	785±12	8.3±0.3	41±1.3	2.7±0.17 (3.0)
ZnO	803±3	8.9±0.19	48±1.4	3.5±0.17 (3.7)

If the doped EELs are incorporated in the organic solar cells, a significant improvement of the device performance is observed. The s-shape is significantly reduced for devices with PCBM, bis-PCBM and ICBA after doping with RhB. The performance of the ZnO reference devices is almost reached. This improvement is attributed to the doping effect in the EELs.

Kirchartz et al. recently published a simulation that matches this data very well. They reported that the lowered built-in field affects only the fill factor and not, as often assumed, shifts the J-V curve to lower voltages if using selective contacts.[144] When using fullerene EELs and also fullerenes in the absorber selective contacts can be assumed. Therefore, recombination happens only at the internal donor-acceptor interface inside the absorber. Indeed, a s-shape rather than a voltage shift is observed. Hence, for the EELs studied herein, the reduced s-shape is directly related to the Fermi energy shift introduced by doping of the fullerenes. This as well is in accordance with the doping efficiency determined from the EPR measurements (table 6.3). For doped PCBM, the s-shape vanishes almost completely due to the higher doping efficiency, whereas, for the doped bisadducts, a s-shape is still observed. Due to the low shunt resistance, an shift of the J-V curve to higher current densities is observed leading to higher  $V_{OC}$  when using doped EELs instead of non-doped EELs.

### 6.3.3. Summary

The doping process of different fullerenes with the cationic dye RhB is successfully transferred from evaporation to solution processing. EPR measurements under illumination show an increase in the spin concentration upon doping. The monoadduct with the lower LUMO level shows higher doping efficiencies than the bisadducts due to their higher LUMO. By using an ethanolic nanoparticle solution for depositing the active layer, solution processed organic solar cells can be built utilizing the insolubility of the undoped and doped matrix layers in EtOH. The solar cells comprising doped EELs show an increased performance compared to solar cells comprising undoped EELs and similar key performance parameters as the reference ZnO.

### 6.3.4. Sample preparation

All used materials and their purities are listed in appendix A.2. All chemicals have been used without further purification.

The ZnO layers were applied from a ZnO nanoparticle dispersion in isopropanol (Nanograde N-10, 2.5 wt%) from Nanograde Ltd. The used PEDOT:PSS formulation (HTL Solar) was purchased from Heraeus.



For the synthesis of the absorber nanoparticles as absorber, that can be deposited from alcoholic dispersion, P3HT ( $M_w = 57$  kDa,  $DM = 2.4$ ,  $RR = 91\%$ ) from Rieke Metals was used. Poly(3-hexylthiophene):indene- $C_{60}$  bisadduct (P3HT:ICBA) nanoparticle (NP) dispersions (1:1, w:w, 10 g/L, EtOH,  $R_H=165$  nm) have been synthesized according to the literature.[166] Therefore P3HT (35.6 mg) and ICBA (35.6 mg, 1 eq.) were dissolved in chloroform (7.12 ml, 10 g/L) at  $50^\circ\text{C}$  for 1.5 h. The solution was precipitated in EtOH (28 ml) at  $50^\circ\text{C}$ . The resulting dispersion was heated at  $65^\circ\text{C}$  to remove the chloroform and most of the EtOH to increase the concentration to 10 g/L. The particle size and distribution were measured by dynamic light scattering with a Malvern Instruments Zetasizer Nano-ZS.

All processing and optoelectronic characterization processes were realized in a clean-room (class 1000 - 100 000). This was necessary because organic layers often exhibit thicknesses of only a few ten nanometers. Thus a dust grain may lead to short cuts and destroy the device. Therefore, substrates were cleaned for 10 minutes in acetone and 2-propanol in an ultrasonic bath. Then they were treated with oxygen plasma to remove residual organic material. As substrates either pure glass or structured ITO coated glass substrates ( $R_{\square} = 13 \Omega/\square$ ) were used. Unless mentioned otherwise all further processing and characterization steps have been carried out in nitrogen atmosphere in a glovebox system.

[6,6]-Phenyl  $C_{61}$ -butyric acid methyl ester (PCBM), [6,6]-diphenyl  $C_{62}$ -bis(butyric acid methyl ester) (bis-PCBM) and ICBA were dissolved (20 g/L) in dichlorobenzene (DCB). RhB was dissolved (20 g/L) in EtOH. The initial solutions were mixed to yield fullerene:RhB solutions with a molecular dopant concentration of 20 mol%.

All measurements were performed using a Cary 5000 by Agilent Technologies under ambient conditions. Spincoated organic thin-films with a thickness of around 30 nm (1000 rpm, 45s, 4000 rpm, 3 s) were measured on glass substrates against a glass reference.

The EPR experiments in this work have been realized in cooperation with the group of Professor Jan Behrends at the Joint EPR Lab at the FU Berlin measured either by Kelvin Yao (tests for reproducibility for fullerene:RhB matrix:dopant combinations) or by myself (first test measurements of fullerene:RhB matrix:dopant combinations) under supervision of Professor Jan Behrends.

To study the influence of electrical doping by cationic dyes, the architecture ITO/EEL (20 nm)/P3HT:ICBA (160 nm)/ PEDOT:PSS (35 nm)/Ag (100 nm) was used, comprising undoped and doped fullerenes as EEL. Again, ZnO was used as reference material.

The doped or undoped fullerenes were spin cast from solution (4000 rpm, 45 s). ZnO was processed as described before. P3HT:ICBA nanoparticles were used as active layer of the organic solar cells. They were deposited by iterative spin coating ( $3 \times 1000$  rpm, 20 s) of alcoholic nanoparticle dispersions on a rotating substrate to prevent dissolution of the fullerene layers underneath. After deposition the samples were annealed at 150°C for 10 min. Afterwards an aqueous solution (1:1, v:v) of PEDOT:PSS (HTL Solar) was spin coated (500 rpm, 5 s; 2000 rpm, 30 s) on top and the samples were annealed on a hotplate (120°C, 10 min). The silver electrode was processed as described before.

J-V curves were recorded on a source measure unit (Keithley 238) under illumination from a spectrally monitored solar simulator (Oriel 300 W, 1000 W/m<sup>2</sup>, ASTM AM 1.5G), calibrated by a KG5 filtered silicon reference cell (91150-KG5, Newport). The sample edges were masked to avoid light-incoupling through substrate modes. The solar cells comprising P3HT:ICBA NP were measured again after 10 days because the results become slightly better when remeasured due to shunt burning.

## 7 | Concluding remarks and outlook

To enhance the efficiency of organic optoelectronic devices doped and to ensure ohmic contacts between the active material and the electrodes to prevent voltage losses interlayers are used. Common devices are built using evaporation processes, but more and more research is progressing towards solution processing, enabling cheap large-area roll-to-roll production on flexible substrates.

This thesis investigates different procedures for electrical doping processed from solution. In case of p-doping, a feasible way to combine the optoelectronic properties of low-molecular weight materials, that tend to form aggregates when processed from solution, with the better film forming properties of amorphous polymers by the usage of non-conjugated side-chain polymers with attached functional groups is shown. MTDATA, TPD, PMTDATA, PTPD, XMTDATA and XTPD are p-doped with the commercial available dopants  $F_4TCNQ$  and  $HATCN_6$ . The doping of these non-crosslinkable and crosslinkable polymers occurs to be as efficient as the doping of molecular materials or better and shows no negative effects upon attaching the functional groups to the polystyrene backbone or the implementation of a crosslinkable group.

The charge carrier transfer from the HOMO of the matrix to the LUMO of the dopant is proven by additional absorption bands in UV-vis-NIR spectra and increased EPR-signals. By PESA, the depletion of the matrix' HOMO is shown. An increased conductivity and mobility is measured by monopolar devices and CELIV and the formation of ohmic contacts is observed when implementing the doped matrices as hole-injection layers in OLEDs.

While the non-crosslinkable and crosslinkable polymers show similar results in all characterized electronic properties as the low-molecular species. Nevertheless the high crosslinking temperature remains challenging. At higher temperatures,  $F_4TCNQ$  evaporates from the layer and  $HATCN_6$  forms large crystals due to demixing with the polymers. The main reason why the crosslinking reaction has to be carried out at such high temperatures is the high  $T_g$  of the polymeric materials. Therefore, the glass transition temperature of the polymers should be further decreased in the future, e.g. by introducing side-chains on the functional moieties which is currently investigated by our collaboration partner at the Fraunhofer IAP.

It was also shown that the doping concentration to reach a saturation in conductivity measurements is not the same as measured by concentration dependent UV-vis and PESA. This shows, that the molecular properties cannot be transferred 1:1 to the device properties.

The second part of this thesis focuses on the solution processing of n-doped organic semiconductors. This represents a bigger challenge due to the insolubility of commonly used alkali metal dopants. So far, they were only soluble under very rough conditions (e.g.  $-78^{\circ}\text{C}$  in ammonia) which are not suitable for industrial processes.

In this thesis, it is also shown that n-doping can be achieved employing wet processes. By adding solid alkali metals (here: sodium) to a solution of an organic semiconductor in an organic solvent at room temperature, the alkali metal is dissolved. With this technique, alkali metal doped layers are no longer exclusively accessible by using evaporation techniques. In future work, non-crosslinkable and crosslinkable side-chain polymers, like for the p-dopable organic semiconductors, should be considered to ease the processing from solution of the n-doped materials. The first tests were already realized together with our collaboration partner from the Fraunhofer IAP.

This thesis also shows a process to solution process n-doped layers by using cationic dyes (here: rhodamine B). The doping can be activated directly in the applied films by white-light irradiation which transfers the dye to its active leuco form. Nevertheless, the EPR spectra show that the doping is only efficient, if the sample is illuminated by white light during the measurement. On the other hand, in vacuum processed thin films an efficient doping can also be realized by a transfer in the leuco form by evaporation. This difference may be caused by a different integration in the matrix, if processed on a charged layer instead. Therefore, it may be worth trying to illuminate the samples during spincoating. In organic solar cells, this does not make a difference because they work under illumination only.

In both cases, electrical doping prevails thin-film deposition under inert atmosphere. An enhanced electron extraction is realized when incorporating the respective layers into organic solar cells. Here, also coupling of the fullerenes to a polymer backbone may be possible. We already started to develop a suitable polymer to which the fullerenes can be attached.

In this thesis, it is verified that the various doping processes can be transferred from vacuum to solution processes which will allow to employ cheaper printing techniques in industry. The efficiency of OLEDs comprising p-doped HILs is demonstrated, whereas n-doping is tested in electron extraction layers in organic solar cells. Due to the similar structure of organic solar cells and organic light emitting diodes, both p- and n-doped charge extraction/injection layers should be convertible to be also used in the respective

other organic optoelectronic devices. Future printable organic solar cells and OLEDs may therefore rely on such solution processed p- and n-doped charge carrier extraction or injections layers, respectively. The systems studied here provide a viable alternative to the commonly used acidic PEDOT:PSS or the fragile ZnO.



# Bibliography

- [1] Erneuerbare Energien in Deutschland - Daten zur Entwicklung 2015, tech. rep., Bundesministerium für Wirtschaft und Energie (BMWi), Berlin, **2015**.
- [2] S. Beaupré, P. L. T. Boudreault, M. Leclerc, *Adv. Mater.* **2010**, *22*, DOI 10.1002/adma.200903484.
- [3] M. A. Green, K. Emery, Y. Hishikawa, W. Warta, E. D. Dunlop, *Prog. Photovolt Res. Appl.* **2016**, *24*, 3–11.
- [4] Research Cell Efficiency Records, **2016**.
- [5] S. E. Shaheen, D. S. Ginley, G. E. Jabbour, G. Editors, **2005**, *30*, 10–19.
- [6] Y. Li, Y. Zou, *Adv. Mater.* **2008**, *20*, 2952–2958.
- [7] N. Holonyak, S. F. Bevacqua, *Appl. Phys. Lett.* **1962**, *1*, 82–83.
- [8] H. Riechert, *Phys. Status Solidi* **2015**, *212*, 893–896.
- [9] Samsung Galaxy Round is now official, phone has October 10th release date in Korea, **2013**.
- [10] LG unveils flexible and transparent OLED displays, **2014**.
- [11] R. Sondergaard, M. Hösel, D. Angmo, T. T. Larsen-Olsen, F. C. Krebs, *Mater. Today* **2012**, *15*, 36–49.
- [12] B. Maennig, M. Pfeiffer, a. Nollau, X. Zhou, K. Leo, P. Simon, *Phys. Rev. B* **2001**, *64*, 1–9.
- [13] Y. Zhao, L. Chen, C. Li, K. Müllen, *Synth. Met.* **2013**, *174*, 46–49.
- [14] T. Aytun, A. Turak, I. Baikie, G. Halek, C. W. Ow-Yang, *Nano Lett.* **2012**, *12*, 39–44.
- [15] F. Nickel, M. Reinhard, Z. Zhang, A. Pütz, S. Kettlitz, U. Lemmer, A. Colmann, *Appl. Phys. Lett.* **2012**, *101*, 10–13.
- [16] Y.-M. Chang, C.-Y. Leu, *J. Mater. Chem. A* **2013**, *1*, 6446–6451.
- [17] S. Woo, W. Hyun Kim, H. Kim, Y. Yi, H.-K. Lyu, Y. Kim, *Adv. Energy Mater.* **May 2014**, *4*, n/a–n/a.
- [18] H. S. Yang, L. S. Wu, Z. Y. Huang, *Appl. Mech. Mater.* **Apr. 2014**, *536-537*, 1426–1430.
- [19] S. Stolz, M. Scherer, E. Mankel, R. Lovrinčić, J. Schinke, W. Kowalsky, W. Jaegermann, U. Lemmer, N. Mechau, G. Hernandez-Sosa, *ACS Appl. Mater. Interfaces* **May 2014**, *6*, 6616–22.
- [20] K. Zhang, C. Zhong, S. Liu, A.-h. Liang, S. Dong, F. Huang, *J. Mater. Chem. C* **2014**, *2*, 3270–3277.

- [21] Y. Zhou, C. Fuentes-Hernandez, J. Shim, J. Meyer, a. J. Giordano, H. Li, P. Winget, T. Papadopoulos, H. Cheun, J. Kim, M. Fenoll, A. Dindar, W. Haske, E. Najafabadi, T. M. Khan, H. Sojoudi, S. Barlow, S. Graham, J.-L. Bredas, S. R. Marder, A. Kahn, B. Kippelen, *Science (80-. )*. **2012**, *336*, 327–332.
- [22] S. Höfle, M. Bruns, S. Strässle, C. Feldmann, U. Lemmer, A. Colsmann, *Adv. Mater.* **Aug. 2013**, *25*, 4113–6.
- [23] S. Höfle, H. Do, E. Mankel, M. Pfaff, Z. Zhang, D. Bahro, T. Mayer, W. Jaegermann, D. Gerthsen, C. Feldmann, U. Lemmer, A. Colsmann, *Org. Electron.* **2013**, *14*, 1820–1824.
- [24] K. Walzer, B. Maennig, M. Pfeiffer, K. Leo, *Chem. Rev.* **2007**, *107*, 1233–1271.
- [25] B. Lüssem, M. Riede, K. Leo, *Phys. status solidi* **2013**, *210*, 9–43.
- [26] W. Gao, A. Kahn, *Appl. Phys. Lett.* **2001**, *79*, 4040–4042.
- [27] J. Huang, M. Pfeiffer, A. Werner, J. Blochwitz, K. Leo, S. Liu, *Appl. Phys. Lett.* **2002**, *80*, 139–141.
- [28] X. Zhou, M. Pfeiffer, J. S. Huang, J. Blochwitz-Nimoth, D. S. Qin, A. Werner, J. Drechsel, B. Maennig, K. Leo, *Appl. Phys. Lett.* **2002**, *81*, 922–924.
- [29] J. Tardy, M. B. Khalifa, D. Vaufrey, *Mater. Sci. Eng. C* **2006**, *26*, 196–201.
- [30] M. B. Khalifa, D. Vaufrey, J. Tardy, *Org. Electron.* **2004**, *5*, 187–198.
- [31] L. Sims, U. Hörmann, R. Hanfland, R. C. MacKenzie, F. R. Kogler, R. Steim, W. Brütting, P. Schilinsky, *Org. Electron.* **Aug. 2014**, 6–11.
- [32] F. Li, A. Werner, M. Pfeiffer, K. Leo, X. Liu, *J. Phys. Chem. B* **2004**, *108*, 17076–17082.
- [33] F. Li, M. Pfeiffer, A. Werner, K. Harada, K. Leo, N. Hayashi, K. Seki, X. Liu, X.-D. Dang, *J. Appl. Phys.* **2006**, *100*, 23716.
- [34] A. G. Werner, F. Li, K. Harada, M. Pfeiffer, T. Fritz, K. Leo, *Appl. Phys. Lett.* **2003**, *82*, 4495–4497.
- [35] T. Menke, D. Ray, H. Kleemann, K. Leo, M. Riede, *Phys. Status Solidi Basic Res.* **2015**, *252*, 1877–1883.
- [36] T. Uchida, S. Kaneta, M. Ichihara, M. Ohtsuka, T. Otomo, D. R. Marx, *Jpn. J. Appl. Phys.* **2005**, *44*, L282–L284.
- [37] J. Kido, T. Matsumoto, *Appl. Phys. Lett.* **1998**, *73*, 2866–2868.
- [38] J.-H. Lee, M.-H. Wu, C.-C. Chao, H.-L. Chen, M.-K. Leung, *Chem. Phys. Lett.* **2005**, *416*, 234–237.
- [39] D. Moses, N. Colaneri, A. J. Heeger, *Solid State Commun.* **1986**, *58*, 535–539.
- [40] G. Parthasarathy, C. Shen, a. Kahn, S. R. Forrest, *J. Appl. Phys.* **2001**, *89*, 4986–4992.
- [41] A. Werner, F. Li, K. Harada, M. Pfeiffer, T. Fritz, K. Leo, S. Machill, *Adv. Funct. Mater.* **2004**, *14*, 255–260.
- [42] F. Liu, J.-M. Nunzi, *Appl. Phys. Lett.* **2011**, *99*, 63301.



- [43] F. Nickel, T. Haas, E. Wegner, D. Bahro, S. Salehin, O. Kraft, P. A. Gruber, A. Colsmann, *Sol. Energy Mater. Sol. Cells* **Nov. 2014**, *130*, 317–321.
- [44] S. D. Yambem, K.-S. Liao, N. J. Alley, S. a. Curran, *J. Mater. Chem.* **2012**, *22*, 6894–6898.
- [45] S. Nam, H. Kim, M. Shin, H. Lee, Y. Kim, *J. Org. Semicond.* **2013**, *1*, 22–29.
- [46] J. S. Swensen, L. Wang, J. E. Rainbolt, P. K. Koech, E. Polikarpov, D. J. Gaspar, A. B. Padmaperuma, *Org. Electron.* **2012**, *13*, 3085–3090.
- [47] J. S. Swensen, L. Wang, E. Polikarpov, J. E. Rainbolt, P. K. Koech, L. Cosimbescu, A. B. Padmaperuma, *Synth. Met.* **2013**, *163*, 29–32.
- [48] J. E. Rainbolt, A. B. Padmaperuma, N. Govind, D. J. Gaspar, *Mol. Simul.* **2013**, *39*, 350–356.
- [49] K. Kanakarajan, A. W. Czarnik, *J. Org. Chem.* **1986**, *51*, 5241–5243.
- [50] R. C. Wheland, E. L. Martin, *J. Org. Chem.* **1975**, *40*, 3101–3109.
- [51] C. Sprau, F. Buss, M. Wagner, D. Landerer, M. Koppitz, A. Schulz, D. Bahro, W. Schabel, P. Scharfer, A. Colsmann, *Energy Environ. Sci.* **2015**, *8*, 2744–2752.
- [52] P. Wei, J. H. Oh, G. Dong, Z. Bao, *J. Am. Chem. Soc.* **2010**, *132*, 8852–8853.
- [53] C.-Z. Li, C.-C. Chueh, H.-L. Yip, F. Ding, X. Li, A. K.-Y. Jen, *Adv. Mater.* **2013**, *25*, 2457–2461.
- [54] S. E. Shaheen, G. E. Jabbour, B. Kippelen, N. Peyghambarian, J. D. Anderson, S. R. Marder, N. R. Armstrong, E. Bellmann, R. H. Grubbs, *Appl. Phys. Lett.* **1999**, *74*, 3212–3214.
- [55] M. W. Thesen, B. Höfer, M. Debeaux, S. Janietz, A. Wedel, A. Köhler, H.-h. Johannes, H. Krueger, *J. Poly. Sci. A Poly. Chem.* **2010**, *48*, 3417–3430.
- [56] D. I. Son, H. H. Kim, S. Cho, D. K. Hwang, J. W. Seo, W. K. Choi, *Org. Electron.* **2014**, *15*, 886–892.
- [57] W. Ki Bae, J. Kwak, J. Lim, D. Lee, M. Ki Nam, K. Char, C. Lee, S. Lee, *Nanotechnology* **2009**, *20*, 075202.
- [58] X. Gong, S.-H. Lim, J. C. Ostrowski, D. Moses, C. J. Bardeen, G. C. Bazab, *J. Appl. Phys.* **2004**, *95*, 948–953.
- [59] S. Tokito, M. Suzuki, F. Sato, M. Kamachi, K. Shirane, *Org. Electron.* **Sept. 2003**, *4*, 105–111.
- [60] V. R. Nikitenko, V. I. Arkhipov, Y.-H. Tak, J. Pommerehne, H. Bässler, H.-H. Hörhold, *J. Appl. Phys.* **1997**, *81*, 7514.
- [61] S. Sax, N. Rugen-Penkalla, A. Neuhold, S. Schuh, E. Zojer, E. J. W. List, K. M??llen, *Adv. Mater.* **2010**, *22*, 2087–2091.
- [62] E. Bellmann, S. E. Shaheen, S. Thayumanavan, S. Barlow, R. H. Grubbs, S. R. Marder, B. Kippelen, *Chem. Mater.* **1998**, *10*, 1668–1676.
- [63] S. Liu, X. Jiang, H. Ma, M. S. Liu, A. K. Jen, **2000**, 3514–3517.
- [64] X. Z. Jiang, S. Liu, M. S. Liu, H. Ma, A. K.-Y. Jen, *Appl. Phys. Lett.* **2000**, *76*, 2985–2987.

- [65] P. S. Rudati, D. C. Mueller, K. Meerholz, *Procedia Chem.* **2012**, *4*, 216–223.
- [66] W.-Y. Hung, C.-Y. Lin, T.-L. Cheng, S.-W. Yang, A. Chaskar, G.-L. Fan, K.-T. Wong, T.-C. Chao, M.-R. Tseng, *Org. Electron.* **2012**, *13*, 2508–2515.
- [67] G. Liaptsis, K. Meerholz, *Adv. Funct. Mater.* **2013**, *23*, 359–365.
- [68] C. A. Zuniga, J. Abdallah, W. Haske, Y. Zhang, I. Coropceanu, S. Barlow, B. Kippelen, S. R. Marder, *Adv. Mater.* **2013**, *25*, 1739–1744.
- [69] X.-c. Li, T.-m. Yong, J. Griiner, B. H. Andrew, *Synth. Met.* **1997**, *84*, 437–438.
- [70] M. Lechner, K. Gehrke, E. H. Nordmeier, *Makromolekulare Chemie*, Springer Basel AG, Basel, 3rd editio, **2003**.
- [71] H. Akamatu, H. Inokuchi, Y. Matsunaga, *Nature* **1954**, *173*, 168–169.
- [72] T. Ito, H. Shirakawa, S. Ikeda, **1974**, *12*, 11–20.
- [73] H. Shirakawa, E. J. Louis, A. G. MacDiarmid, C. K. Chiang, A. J. Heeger, *J. Chem. Soc. Chem. Commun.* **1977**, 578–580.
- [74] C. W. Tang, *Appl. Phys. Lett.* **1986**, *48*, 183–185.
- [75] C. W. Tang, S. A. Vanslyke, *Appl. Phys. Lett.* **1987**, *51*, 913–915.
- [76] F. A. Carey, R. J. Sundberg, *Advanced Organic Chemistry Part A: Structures and Mechanisms*, Kluwer Academic Publishers-Plenum Publishers, New York, 4th editio, **2000**.
- [77] J. Clayden, N. Greeves, S. Warren, *Organic Chemistry*, Oxford University Press Inc., New York, 2nd editio, **2000**.
- [78] A. A. Frost, B. Musulin, *J. Chem. Phys.* **1953**, *21*, 572–573.
- [79] *Physics of Organic Semiconductors*, (Ed.: W. Brütting), WILEY-VCH Verlag GmbH, Weinheim, 1st editio, **2005**.
- [80] *Organic Photovoltaics: Materials, Device Physics, and Manufacturing Technologies*, (Eds.: C. Brabec, U. Scherf, V. Dyakonov), WILEY-VCH Verlag GmbH, Weinheim, 1st editio, **2008**.
- [81] H. Ilbach, H. Lüth, *Festkörperphysik: Einführung in die Grundlagen*, Springer Berlin-Heidelberg, Berlin, Heidelberg, 7th editio, **2009**.
- [82] P. Prins, F. Grozema, F. Galbrecht, U. Scherf, L. Siebbeles, *J. Phys. Chem. C* **2007**, *111*, 11104–11112.
- [83] M. Rehahn, *Chemie unserer Zeit* **2003**, *37*, 18–30.
- [84] H. Meier, U. Stalmach, H. Kolshorn, *Acta Polym.* **1997**, *48*, 379–384.
- [85] A. Ajayaghosh, *Chem. Soc. Rev.* **2003**, *32*, 181.
- [86] Z. Shen, P. Burrows, V. Bulovic, D. McCarty, M. Thompson, S. Forrest, *Jpn. J. Appl. Phys.* **1996**, *35-2*, L401–L404.
- [87] S. Barth, P. Müller, H. Riel, P. F. Seidler, W. Rieß, H. Vestweber, H. Bässler, *J. Appl. Phys.* **2001**, *89*, 3711–3719.
- [88] J. Staudigel, M. Stossel, F. Steuber, J. Simmerer, *Appl. Phys. Lett.* **1999**, *75*, 217–219.

- [89] S. M. Sze, K. K. Ng, *Physics of semiconductor devices*, Wiley Interscience, New Jersey, 3rd editio, **2007**.
- [90] A. Pivrikas, H. Neugebauer, N. S. Sariciftci, *Sel. Top. Quantum Electron. IEEE J. Nov.* **2010**, *16*, 1746–1758.
- [91] S. H. Park, A. Roy, S. Beaupré, S. Cho, N. Coates, J. S. Moon, D. Moses, M. Leclerc, K. Lee, S. Beaupre, A. J. Heeger, *Nat. Photon.* **2009**, *3*, 297–302.
- [92] R. Kroon, M. Lenes, J. C. Hummelen, P. W. M. Blom, B. De Boer, *Polym. Rev.* **2008**, *48*, 531–582.
- [93] F. Huang, Y.-J. Cheng, Y. Zhang, M. S. Liu, A. K.-Y. Jen, *J. Mater. Chem.* **2008**, *18*, 4495.
- [94] I. G. Hill, a. Kahn, Z. G. Soos, R. a. Pascal, *Chem. Phys. Lett.* **2000**, *327*, 181–188.
- [95] P. Peumans, A. Yakimov, S. R. Forrest, *J. Appl. Phys.* **2003**, *93*, 3693–3723.
- [96] Y. Liang, Z. Xu, J. Xia, S. T. Tsai, Y. Wu, G. Li, C. Ray, L. Yu, *Adv. Mater.* **2010**, *22*, 135–138.
- [97] H. B. Michaelson, *J. Appl. Phys.* **1977**, *48*, 4729–4733.
- [98] A. Facchetti, *Chem. Mater.* **2011**, *23*, 733–758.
- [99] M. C. Scharber, D. Mühlbacher, M. Koppe, P. Denk, C. Waldauf, A. J. Heeger, C. J. Brabec, *Adv. Mater.* **2006**, *18*, 789–794.
- [100] A. Gadisa, M. Svensson, M. R. Andersson, O. Inganäs, *Appl. Phys. Lett.* **2004**, *84*, 1609–1611.
- [101] K. Vandewal, K. Tvingstedt, A. Gadisa, O. Inganäs, J. V. Manca, *Nat. Mater.* **2009**, *8*, 904–909.
- [102] G. G. Malliaras, J. R. Salem, P. J. Brock, J. C. Scott, *J. Appl. Phys.* **1998**, *84*, 1583–1587.
- [103] H.-G. Wagemann, H. Eschrich, *Photovoltaik : Solarstrahlung und Halbleitereigenschaften, Solarzellen- konzepte und Aufgaben*, Vieweg + Teubner, Wiesbaden, 2nd editio, **2010**.
- [104] Y. M. Nam, J. Huh, W. Ho Jo, *Sol. Energy Mater. Sol. Cells* **2010**, *94*, 1118–1124.
- [105] C. Winder, N. S. Sariciftci, *J. Mater. Chem.* **2004**, *14*, 1077.
- [106] T. Muneer, *Solar Radiation and Daylight Models*, Elsevier Ltd, Oxford, 2nd editio, **2004**.
- [107] Standard Tables for Reference Solar Spectral Irradiances : Direct Normal and Hemispherical on 37° Tilted Surface, tech. rep. Reapproved, ASTM International, West Conshohocken, PA, **2012**, pp. 1–21.
- [108] J. Kalinowski, *Organic Light-Emitting Diodes - Principles, Characteristics, and Processes*, Marcel Dekker, New York, 1st editio, **2005**.
- [109] *Organic Light Emitting Devices*, (Ed.: J. Singh), InTech, Rijeka, **2012**.
- [110] H. Kim, C. M. Gilmore, A. Piqué, J. S. Horwitz, H. Mattoussi, H. Murata, Z. H. Kafafi, D. B. Chrisey, *J. Appl. Phys.* **1999**, *86*, 6451–6461.
- [111] H. Ishii, K. Sugiyama, E. Ito, K. Seki, *Adv. Mater.* **1999**, *11*, 605–625.

- [112] C. J. Brabec, a. Cravino, D. Meissner, N. Serdar Sariciftci, T. Fromherz, M. T. Rispens, L. Sanchez, J. C. Hummelen, *Adv. Funtional Mater.* **2001**, *11*, 374–380.
- [113] I. Salzmann, G. Heimel, S. Duhm, M. Oehzelt, P. Pingel, B. M. George, A. Schnegg, K. Lips, R.-P. Blum, A. Vollmer, N. Koch, *Phys. Rev. Lett.* **Jan. 2012**, *108*, 035502.
- [114] G.-T. Chen, S.-H. Su, M. Yokoyama, *J. Electrochem. Soc.* **2006**, *153*, H68.
- [115] P. K. Koech, A. B. Padmaperuma, L. Wang, J. S. Swensen, E. Polikarpov, J. T. Darsell, J. E. Rainbolt, D. J. Gaspar, *Chem. Mater.* **2010**, *22*, 3926–3932.
- [116] D. Y. Kondakov, *J. Appl. Phys.* **2006**, *99*,
- [117] M. A. Khan, W. Xu, Khizar-ul-Haq, Y. Bai, F. Wei, X. Y. Jiang, Z. L. Zhang, W. Q. Zhu, *J. Phys. D. Appl. Phys.* **2007**, *40*, 6535.
- [118] E. S. Lewis, J. M. Perry, R. H. Grinstead, **1969**, *917*, 899–905.
- [119] B. Maennig, J. Drechsel, D. Gebeyehu, P. Simon, F. Kozlowski, A. Werner, F. Li, S. Grundmann, S. Sonntag, M. Koch, K. Leo, M. Pfeiffer, H. Hoppe, D. Meissner, N. Sariciftci, I. Riedel, V. Dyakonov, J. Parisi, *Appl. Phys. A Mater. Sci. Process.* **2004**, *79*, 1–14.
- [120] G. R. Eaton, S. S. Eaton, D. P. Barr, R. T. Weber, *Quantitative EPR*, Springer Wien, SpringerLink (Online Service), New York, **2010**.
- [121] T. Glatzel, S. Sadewasser, M. C. Lux-Steiner, *Appl. Surf. Sci.* **2003**, *210*, 84–89.
- [122] U. Ahlrichs, M. Bär, M. Häser, H. Horn, C. Kölmel, *Chem. Phys. Lett.* **1989**, *162*, DOI doi:10.1016/0009-2614(89)85118-8.
- [123] A. D. Becke, *J. Chem. Phys.* **1993**, *98*, 1372.
- [124] A. Schäfer, H. Horn, R. Ahlrichs, *J. Chem. Phys.* **1992**, *97*, 2571.
- [125] J. J. P. Stewart, *J. Mol. Model.* **2007**, *13*, 1173–1213.
- [126] J. J. P. Stewart, *MOPAC2012*, Colorado Springs, **2012**.
- [127] T. Neumann, D. Danilov, C. Lennartz, W. Wenzel, *J. Comput. Chem.* **2013**, *34*, 2716–25.
- [128] P. Friederich, F. Symalla, V. Meded, T. Neumann, W. Wenzel, *J. Chem. Theory Comput.* **2014**, *10*, 3720–3725.
- [129] P. Friederich, V. Meded, F. Symalla, M. Elstner, W. Wenzel, *J. Chem. Theory Comput.* **2015**, *11*, 560–567.
- [130] P. S. Davids, I. H. Campbell, D. L. Smith, **1997**, *82*, 6319–6325.
- [131] P. N. Murgatroyd, *J. Phys. D. Appl. Phys.* **1970**, *3*, 308.
- [132] G. Juska, K. Arlauskas, M. Viliu, K. Genevic, R. Österbacka, H. Stubb, *Phys. Rev. B* **2000**, *62*, 235–238.
- [133] *Impedance Spectroscopy Theory, Experiment, and Applications*, (Eds.: E. Barsoukov, J. R. Macdonald), Wiley Interscience, New Jersey, second edi, **2005**.
- [134] <http://elektroarsenal.net/frequency-dependence-dielectric-constant-and-dielectric-loss.html>.

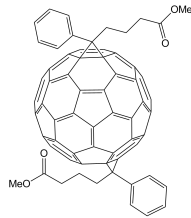
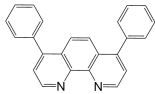
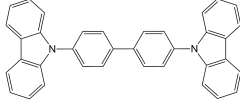
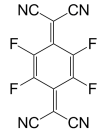
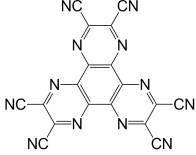
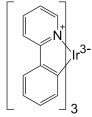

- [135] F. R. P. Limberg, T. Schneider, S. Hoeffle, F. Reisbeck, S. Janietz, A. Colsmann, H. Krüger, *Adv. Energy Mater.*, *submitted*.
- [136] Y. Shirota, T. Kobata, N. Noma, Starburst molecules for amorphous molecular materials. 4,4',4''-Tris(N,N-diphenylamino)triphenylamine and 4,4',4''-tris[N-(3-methylphenyl)-N-phenylamino]triphenylamine. **1989**.
- [137] K. Naito, a. Miura, *J. Phys. Chem.* **1993**, *97*, 6240–6248.
- [138] S. H. Kim, J. Jang, K. S. Yook, J. Y. Lee, *Synth. Met.* **2009**, *159*, 568–570.
- [139] J. Li, C. W. Rochester, I. E. Jacobs, S. Friedrich, P. Stroeve, M. Riede, A. J. Moule, *ACS Appl. Mater. Interfaces* **2015**, acsami.5b09216.
- [140] M. Pfeiffer, K. Leo, X. Zhou, J. S. Huang, M. Hofmann, A. Werner, J. Blochwitz-Nimoth, *Org. Electron.* **2003**, *4*, 89–103.
- [141] K. Tada, S. Takaishi, M. Onoda, *Appl. Phys. Express* **June 2008**, *1*, 071801.
- [142] J. Drechsel, M. Pfeiffer, X. Zhou, A. Nollau, K. Leo, *Synth. Met.* **2002**, *127*, 201–205.
- [143] D. Ray, K. L. Narasimhan, *J. Appl. Phys.* **2008**, *103*, 1–6.
- [144] T. Kirchartz, W. Gong, S. a. Hawks, T. Agostinelli, R. C. I. MacKenzie, Y. Yang, J. Nelson, *J. Phys. Chem. C* **2012**, *116*, 7672–7680.
- [145] A. Armin, G. Juska, B. W. Philippa, P. L. Burn, P. Meredith, R. D. White, A. Pivrikas, *Adv. Energy Mater.* **2013**, *3*, 321–327.
- [146] M. Patankar, K. Joshi, K. Narasimhan, *arXiv Prepr. arXiv1312.0223* **2013**, 1–22.
- [147] Y. Ma, Y. H. Chung, L. Zheng, D. Zhang, X. Yu, L. Xiao, Z. Chen, S. Wang, B. Qu, Q. Gong, D. Zou, *ACS Appl. Mater. Interfaces* **2015**, *7*, 6406–6411.
- [148] N. Boden, R. J. Bushby, O. R. Lozman, *Mol. Cryst. Liq. Cryst.* **2003**, *400*, 105–113.
- [149] Y. Zhang, B. D. Boer, P. W. M. Blom, *Adv. Funct. Mater.* **2009**, *19*, 1901–1905.
- [150] Q. Lin, A. Armin, R. C. R. Nagiri, P. L. Burn, P. Meredith, *Nat Phot.* **2015**, *9*, 106–112.
- [151] Y. Kawabe, J. Abe, *Appl. Phys. Lett.* **2002**, *81*, 493–495.
- [152] G. He, M. Pfeiffer, K. Leo, M. Hofmann, J. Birnstock, R. Pudzich, J. Salbeck, *Appl. Phys. Lett.* **2004**, *85*, 3911–3913.
- [153] S. H. Kim, J. Jang, J. Y. Lee, *Appl. Phys. Lett.* **2007**, *91*, DOI 10.1063/1.2773941.
- [154] S. Höfle, M. Pfaff, H. Do, C. Bernhard, D. Gerthsen, U. Lemmer, A. Colsmann, *Org. Electron. physics, Mater. Appl.* **2014**, *15*, 337–341.
- [155] J. T. Cho, D. H. Kim, E. I. Koh, T. W. Kim, *Thin Solid Films* **Nov. 2014**, *570*, 63–67.
- [156] F.-Z. Sun, A.-L. Shi, Z.-Q. Xu, H.-X. Wei, Y.-Q. Li, S.-T. Lee, J.-X. Tang, *Appl. Phys. Lett.* **2013**, *102*, 133303.
- [157] S. H. Kim, J. Jang, J. Y. Lee, *Appl. Phys. Lett.* **2007**, *91*, DOI 10.1063/1.2773941.

- [158] P. J. Benning, D. M. Poirier, T. R. Ohno, Y. Chen, M. B. Jost, F. Stepniak, G. H. Kroll, J. H. Weaver, J. Fure, R. E. Smalley, *Phys. Rev. B* **1992**, *45*, 6899–6913.
- [159] R. Mitsumoto, T. Araki, E. Ito, Y. Ouchi, K. Seki, K. Kikuchi, Y. Achiba, H. Kurosaki, T. Sonoda, H. Kobayashi, O. V. Boltalina, V. K. Pavlovich, L. N. Sidorov, Y. Hattori, N. Liu, S. Yajima, S. Kawasaki, F. Okino, H. Touhara, *J. Phys. Chem. A* **1998**, *102*, 552–560.
- [160] M. Lenes, G. J. A. H. Wetzelaer, F. B. Kooistra, S. C. Veenstra, J. C. Hummelen, P. W. M. Blom, *Adv. Mater.* **2008**, *20*, 2116–2119.
- [161] Y. He, H.-Y. Chen, J. Hou, Y. Li, *J. Am. Chem. Soc.* **2010**, *132*, 1377–1382.
- [162] V. D. Mihailetschi, P. W. M. Blom, J. C. Hummelen, M. T. Rispens, *J. Appl. Phys.* **2003**, *94*, 6849–6854.
- [163] J. C. Blakesley, D. Neher, *Phys. Rev. B - Condens. Matter Mater. Phys.* **2011**, *84*, DOI 10.1103/PhysRevB.84.075210.
- [164] J. Kong, I.-W. Hwang, K. Lee, *Adv. Mater.* **2014**, *26*, 6275–6283.
- [165] H. Ago, T. Kugler, F. Cacialli, K. Petritsch, R. H. Friend, W. R. Salaneck, Y. Ono, T. Yamabe, K. Tanaka, *Synth. Met.* **1999**, *103*, 2494–2495.
- [166] S. Gärtner, M. Christmann, S. Sankaran, H. Röhm, E.-M. Prinz, F. Pentz, A. Pütz, A. E. Türel, B. Pentz, B. Baumstümmler, A. Colmann, *Adv. Mater.* **2014**, *26*, 6653–7.

# A | Appendix

## A.1. IUPAC-notation and chemical structure of used optoelectronic materials

**Table A.1.** Used optoelectronic materials.

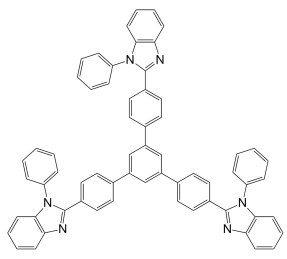
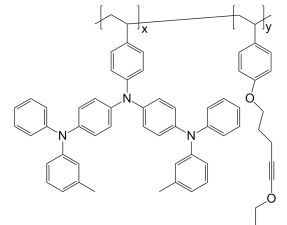
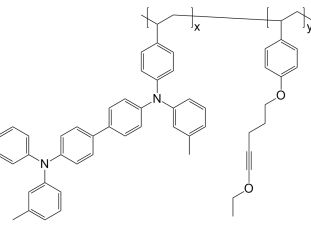
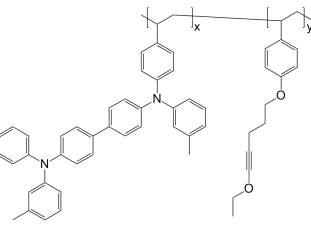
Abbreviation	IUPAC-notation or trivial name	Chemical structure
Bis-PCBM	bis-phenyl-C <sub>61</sub> butyric acid methyl ester	
BPhen	4,7-diphenyl-1,10-phenanthroline	
CBP	4,4'-bis( <i>N</i> -carbazolyl)-1,1'-biphenyl	
F <sub>4</sub> TCNQ	2,3,5,6-tetrafluoro-7,7,8,8-tetracyanoquinodimethane	
HATCN <sub>6</sub>	1,4,5,8,9,12-hexaazatriphenylene	
Ir(ppy) <sub>3</sub>	tris[2-phenylpyridinato-C <sup>2</sup> , <i>N</i> ]iridium(III)	
ICBA	indene-C <sub>60</sub> bisadduct	

**Table A.1.** Used optoelectronic materials

Abbreviation	IUPAC-notation or trivial name	Chemical structure
MTDATA	4,4',4''-tris[phenyl( <i>m</i> -tolyl)amino]triphenylamine	
P3HT	poly-3-hexylthiophene	
PCBM	phenyl-C <sub>61</sub> butyric acid methyl ester	
PEDOT:PSS	poly(3,4-ethylenedioxythiophene):polystyrene sulfonate	
PMTDATA	poly-[4- <i>N,N</i> -bis[4-( <i>N,N</i> -phenyl( <i>m</i> -tolyl)amino)phenylamino]vinylphenyl]	
PTB7-Th	poly[[2,6'-4,8-di(5-ethylhexylthienyl)benzo[1,2-b;3,3'-b']dithiophene][3-fluoro-2[(2-ethylhexyl)carbonyl]thieno[3,4-b]thiophenediyl]]	
PTPD	poly-[ <i>N</i> -phenyl- <i>N,N'</i> -di( <i>m</i> -tolyl- <i>N'</i> -(4-vinylphenyl))biphenyl-4,4'-diamine]	
RhB	rhodamine B	



**Table A.1.** Used optoelectronic materials

Abbreviation	IUPAC-notation or trivial name	Chemical structure
TPBi	1,3,5-tris(1-phenyl-1 <i>H</i> -benzimidazol-2-yl)benzene	
TPD	<i>N,N</i> -bis(3-methylphenyl)- <i>N,N</i> -diphenylbenzidine	
XMTDATA	poly-[4- <i>N,N</i> -bis[4-( <i>N,N</i> -phenyl( <i>m</i> -tolyl)amino]phenylamino)vinylphenyl]-stat-1-((5-ethoxypent-4-yn-1-yl)oxy)-4-vinylbenzene	
XTPD	poly-[ <i>N</i> -phenyl- <i>N,N'</i> -di( <i>m</i> -tolyl- <i>N'</i> -(4-vinylphenyl))biphenyl-4,4'-diamine]-stat-1-((5-ethoxypent-4-yn-1-yl)oxy)-4-vinylbenzene	

## A.2. Materials, suppliers and purities

**Table A.2.** Used chemicals.

Chemicals	Purchased from	Purity (%)
Toluene (anhydrous)	Sigma-Aldrich	99.8
THF (anhydrous)	Sigma-Aldrich	>99.9
EtOH (Rotipuran)	Carl Roth	>99.8
<i>o</i> -xylene	Sigma-Aldrich	97
<i>o</i> -dichlorobenzene	Sigma-Aldrich	99
MTDATA	Sensient Imaging Technologies GmbH	
TPD	Sigma-Aldrich	99
F <sub>4</sub> TCNQ	Sigma Aldrich	97
HATCN <sub>6</sub>	Luminescence Technology Corporation	>99
BPhen	Luminescence Technology Corporation	99
TPBi	Syntec-Sensient	99.95
PC <sub>61</sub> BM	Solenne	99
Bis-PC <sub>61</sub> BM	Solenne	99.5
IC <sub>61</sub> BA	Luminescence Technology Corporation	>99
RhB	Acros	>99
Ir(ppy) <sub>3</sub>	Sensient Imaging Technologies GmbH	99.9
LiF	Chempur	>99.9
MoO <sub>3</sub>	Sigma-Aldrich	99.99
Na (in oil)	Chempur	99.95
Al	Chempur	99.999
Ag	Chempur	99.9

### A.3. Solvent resistance of undoped and doped fullerene layers against Ethanol

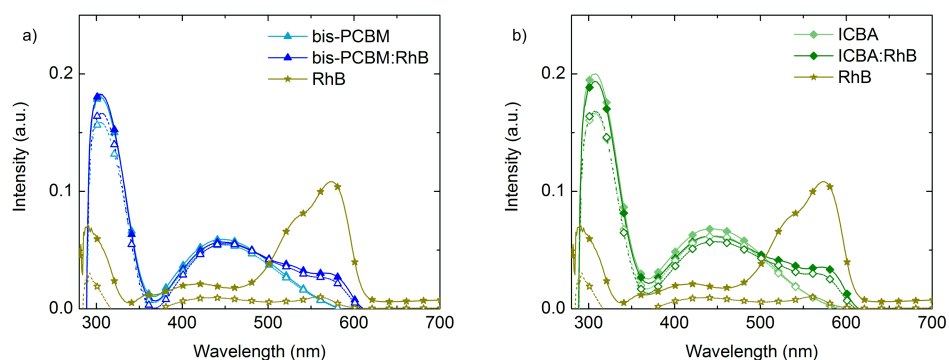


**Figure A.1.** UV-Vis absorption spectra of 20 nm thin-films of undoped and doped (a) bis-PCBM and (b) ICBA (20 mol%) on glass before (closed symbols) and after (open symbols) rinsing with EtOH, and the absorption spectrum of RhB for reference. Upon rinsing with EtOH, the absorption spectrum of the fullerenes and hence the layer thickness do not change. Although RhB is highly soluble in EtOH, rinsing hardly effects the fullerene:RhB layer, indicating that the fullerene matrix affixes the RhB dopant.

#### A.4. Measurements of the organic solar cells directly after fabrication

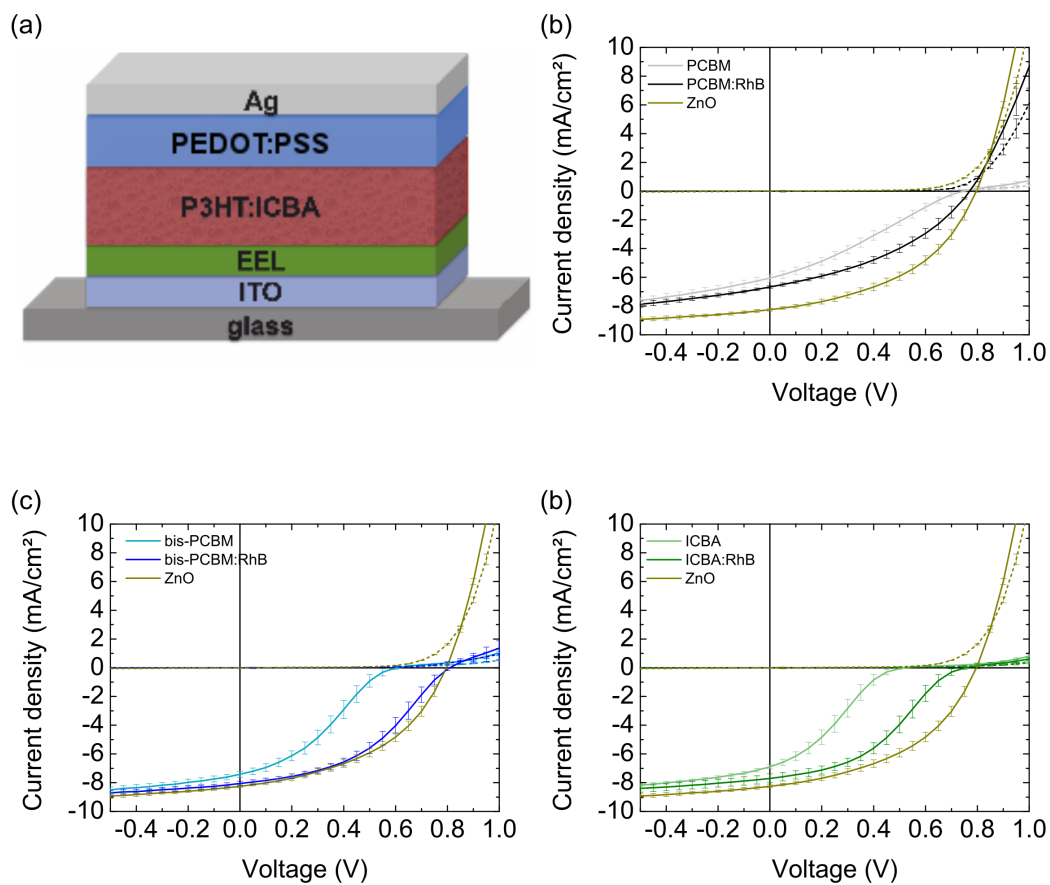


**Figure A.2.** (a) Device architecture and (b)-(d) typical J-V curves of glass/ITO/EEL/P3HT:ICBA/PEDOT:PSS/Ag solar cells under AM1.5 illumination, comprising RhB doped EELs (20 mol%) versus non-doped EELs PCBM:RhB, bis-PCBM:RhB, ICBA:RhB, as measured directly after fabrication. Solar cells comprising state-of-the-art EELs from nanoparticulate ZnO are depicted for reference.

**Table A.3.** Averaged key-performance data of organic solar cells measured directly after fabrication. The PCE in parentheses represent hero devices.

	$V_{OC}$ (mV)	$J_{SC}$ (mA/cm <sup>2</sup> )	FF (%)	PCE (%)
PCBM	740±20	6.1±0.3	28±1.0	1.3±0.11 (1.5)
PCBM:RhB	770±3	6.7±0.09	39±2	2.0±0.2 (2.2)
bis-PCBM	600±20	7.4±0.2	33±1.1	1.5±0.15 (1.8)
bis-PCBM:RhB	807±9	8.1±0.15	43±2	2.8±0.17 (3.2)
ICBA	518±20	6.9±0.15	28±1.8	1.0±0.12 (1.3)
ICBA:RhB	750±30	7.7±0.3	39±0.2	2.3±0.15 (2.6)
ZnO	797±6	8.3±0.10	46±2	3.0±0.16 (3.2)



# Abbreviations

$\alpha$ -NPD	<i>N,N</i> -di(1-naphthyl)- <i>N,N</i> -diphenyl-(1,1'-biphenyl)-4,4'-diamine
AFM	Atomic force microscopy
AIBN	azobisisobutyronitrile
Alq <sub>3</sub>	aluminiumtris(8-hydroxyquinolin)
AM-KPFM	amplitude modulated kelvin probe force microscopy
AOB	acridine orange base
ASTM	American Society for Testing and Materials Standards
ATRP	Atom Transfer Radical Polymerization
Bis-PCBM	bis-phenyl-C <sub>60</sub> butyric acid methyl ester
BPhen	4,7-diphenyl-1,10-phenanthroline
CBP	4,4'-bis( <i>N</i> -carbazolyl)-1,1'-biphenyl
CELIV	charge extraction by linear increasing voltage
CIGS	copper indium gallium selenide
CPD	contact potential difference
CV	crystal violet
$D_M$	polydispersity
DCB	1,2-dichlorobenzene
$E_g$	band gap
$E_I$	ionization potential
EEL	electron extraction layer
EPR	electron paramagnetic spin resonance
ETL	electron transport layer
EtOH	ethanol
F <sub>3</sub> TCNQ-adl	2-(3-(adamantan-1-yl)propyl)-3,5,6-trifluorotetracyanoquinodimethane
F <sub>4</sub> TCNQ	2,3,5,6-tetrafluoro-7,7,8,8-tetracyanoquinodimethane
FF	fill factor
Firpic	iridium(III)bis[(4,6-fluorophenyl)-pyridinato- <i>N,C</i> <sup>2</sup> ]picolate
FM-KPFM	frequency modulated kelvin probe force microscopy
HATCN <sub>6</sub>	1,4,5,8,9,12-hexaazatriphenylene
HEL	hole extraction layer
HIL	hole injection layer
HOMO	highest occupied molecular orbital

HOPG	highly oriented pyrolytic graphite
HTL	hole transport layer
I	current
IAM	Institute of Applied Materials
IAP	Institute of Applied Polymer Research
ICBA	indene-C <sub>60</sub> bisadduct
Ir(ppy) <sub>3</sub>	tris[2-phenylpyridinato-C <sup>2</sup> ,N]iridium(III)
ITO	indium doped tin oxide
J	current-density
J <sub>SC</sub>	short-circuit current
KPFM	Kelvin probe force microscopy
LCD	liquid crystal display
LCV	leuco crystal violet
LED	light emitting diode
LUMO	lowest unoccupied orbital
MEH-PPV	poly[2-methoxy-5-(2-ethylhexyloxy)-1,4-phenylenevinylene]
MIS-CELIV	metal-insulator-semiconductor charge extraction by linear increasing voltage
MO	molecular orbital
MPP	maximum power point
MTDATA	4,4',4''-tris[phenyl( <i>m</i> -tolyl)amino]triphenylamine
NMR	nuclear magnetic resonance
OLED	organic light emitting diode
OSC	organic solar cell
P3HT	poly-3-hexylthiophene
PA	polyacetylen
PC <sub>71</sub> BM	[6,6]-phenyl C <sub>71</sub> -butyric acid methyl ester
PCBM	phenyl-C <sub>61</sub> butyric acid methyl ester
PCDTBT	poly[ <i>N</i> -9'-heptadecanyl-2,7-carbazole-alt-5,5-(4',7'-di-2-thienyl-2',1',3'-benzothiadiazole)]
PCE	power conversion efficiency
PEDOT:PSS	poly(3,4-ethylenedioxythiophene):polystyrene sulfonate
PESA	photoelectron yield spectroscopy in air
PF-TUNA	peak-force-TUNA
PMTDATA	poly-[4- <i>N,N</i> -bis[4-( <i>N,N</i> -phenyl( <i>m</i> -tolyl)amino]-phenylamino)vinylphenyl]
PPP	poly- <i>para</i> -phenylene
PPy	polypyridine



PT	polythiophene
PTB7	poly[[4,8-di(5-ethylhexyloxy)benzo[1,2-b;4,5-b]dithiophene][3-fluoro-2[(2-ethylhexyl)carbonyl]thieno[3,4-b]thiophenediy]]
PTB7-Th	poly[[2,6'-4,8-di(5-ethylhexylthienyl)benzo[1,2-b;3,3-b]dithiophene][3-fluoro-2[(2-ethyl-hexyl)carbonyl]thieno[3,4-b]thiophenediy]]
PTCTA	poly-[ <i>N,N</i> -bis[4-(carbazolyl)phenyl]-4-vinylaniline
PTDATA	poly-[4- <i>N,N</i> -bis[4-( <i>N,N</i> -diphenylamino)phenyl]aminovinylphenyl
PTPD	poly-[ <i>N</i> -phenyl- <i>N,N'</i> -di( <i>m</i> -tolyl- <i>N'</i> -(4-vinylphenyl))biphenyl-4,4'-diamine]
PVK	poly(9-vinylcarbazole)
PyB	pyronine B
$R_p$	parallel resistance
$R_q$	surface roughness
$R_s$	serial resistance
RAFT	Reversible Addition-Fragmentation Chain Transfer Polymerization
RhB	rhodamine B
TCTA	4,4',4''-tris(carbazol-9-yl)-triphenylamine
TEMPO	2,2,6,6-tetramethylpiperidin- <i>N</i> -oxyl
ToF-SIMS	time of flight-secondary ion mass spectroscopy
TPBi	1,3,5-tris(1-phenyl-1 <i>H</i> -benzimidazol-2-yl)benzene
TPD	<i>N,N</i> -bis(3-methylphenyl)- <i>N,N</i> -diphenylbenzidine
UPS	ultraviolet photoelectron spectroscopy
UV-vis-NIR	ultraviolet-visible-near infrared
V	voltage
$V(\lambda)$	luminous efficiency function
$V_{OC}$	open-circuit voltage
XMTDATA	poly-[4- <i>N,N</i> -bis[4-( <i>N,N</i> -phenyl( <i>m</i> -tolyl)amino]phenylamino)vinylphenyl]-stat-1-((5-ethoxypent-4-yn-1-yl)oxy)-4-vinylbenzene
XTPD	poly-[ <i>N</i> -phenyl- <i>N,N'</i> -di( <i>m</i> -tolyl- <i>N'</i> -(4-vinylphenyl))biphenyl-4,4'-diamine]-stat-1-((5-ethoxypent-4-yn-1-yl)oxy)-4-vinylbenzene
ZnPc	zinc phthalocyanine



# List of Figures

3.1. Some examples of the first conductive polymers. . . . .	9
3.2. Frost-Musulin-diagram to estimate relative energies of the orbitals and overlapping $p_z$ -orbitals in benzol. . . . .	10
3.3. Splitting into orbitals with higher and lower energy, caused by interaction between molecular orbitals. . . . .	11
3.4. Stabilization of charges in a conjugated system, formation of quinoid structures in conjugated aromatics which interrupt the delocalized system. . .	11
3.5. Typical low-molecular weight materials for organic electronics. . . . .	12
3.6. Typical polymers for organic electronics. . . . .	13
3.7. Polymerization degree against fractional monomer conversion for different polymerization techniques. . . . .	14
3.8. Thermally and light induced activation of initiators. . . . .	15
3.9. Chain growth of polystyrene by radical polymerization. . . . .	15
3.10. Chain transfer reaction between two polymers. . . . .	15
3.11. Termination by disproportion reaction of two radicals. . . . .	15
3.12. Termination by combination reaction of two radicals . . . . .	16
3.13. Device architecture and energy diagram of a typical organic solar cell. . .	18
3.14. Characteristic J-V curve of a solar cell measured without (dashed line) or under illumination (solid line) including all characteristic key performance parameters. . . . .	19
3.15. AM1.5 reference spectrum of solar irradiation under an angle of $37^\circ$ . . . .	20
3.16. Device architecture and energy diagram of a typical OLED. . . . .	21
3.17. Alignment of the work function of a metal with the Fermi-level of a semiconductor. . . . .	24
3.18. Different doping mechanisms. . . . .	25
3.19. Hole transport material 4,4',4''-tris[phenyl( <i>m</i> -tolyl)amino]triphenylamine (MTDATA) and organic acceptor 2,3,5,6-tetrafluoro-7,7,8,8-tetracyanoquinodimethane ( $F_4$ TCNQ). . . . .	26
3.20. Electron transport material 4,7-diphenyl-1,10-phenanthroline (BPhen.) . .	26
3.21. Doping reaction of $C_{60}$ with leuco crystal violet (LCV). . . . .	27
4.1. Working principle of photoelectron yields spectroscopy in air. . . . .	33
4.2. Device architecture and typical J-V curve of a monopolar device. . . . .	34
4.3. Device architecture and typical J-t curve of a CELIV device. . . . .	36
4.4. Real and imaginary part of the dielectric constant plotted against frequency.	38
5.1. Chemical structures of the investigated hole transport materials. . . . .	40
5.2. Energy levels of the matrices and dopants. . . . .	42
5.3. Dielectric loss measurements of undoped and doped (10 mol%) MTDATA and PMTDATA. . . . .	43

5.4. UV-vis-NIR spectra of MTDATA and PMTDATA doped with different amounts of F <sub>4</sub> TCNQ. . . . .	45
5.5. PESA measurements of MTDATA and PMTDATA doped with different amounts of F <sub>4</sub> TCNQ. . . . .	45
5.6. Photoelectron yield of undoped and doped (20 mol%) MTDATA and PMTDATA, measured by PESA. . . . .	46
5.7. Photoelectron yield of undoped and doped (20 mol%) TPD and PTPD, measured by PESA. . . . .	47
5.8. UV-vis-NIR absorption spectra of the undoped and doped (20 mol%) matrices MTDATA and PMTDATA. . . . .	48
5.9. Near-infrared (NIR) absorption spectra of the undoped and doped (20 mol%) matrices TPD and PTPD. . . . .	48
5.10. EPR spectra obtained from undoped and doped (20 mol%) MTDATA and PMTDATA. . . . .	49
5.11. EPR spectra obtained from undoped and doped (20 mol%) TPD and PTPD. . . . .	51
5.12. Conductivities of undoped and doped films as measured by MIS-CELIV and on hole-only devices. . . . .	54
5.13. Conductivities of undoped and doped films as measured by MIS-CELIV and on hole-only devices. . . . .	55
5.14. Mobilities of undoped and doped films as measured by MIS-CELIV and hole-only devices. . . . .	57
5.15. Film topography and current pictures of undoped and doped (10 mol%) MTDATA films. . . . .	58
5.16. Topography and current pictures of undoped and doped (10 mol%) PMTDATA films. . . . .	59
5.17. Topography and current pictures of undoped and doped (10 mol%) TPD films. . . . .	60
5.18. Detailed view of agglomerates in TPD:HATCN <sub>6</sub> recorded in different scan directions. . . . .	61
5.19. Topography and current pictures of undoped and doped (10 mol%) PTPD films. . . . .	61
5.20. Device architecture and energy levels of the employed materials. . . . .	63
5.21. J-V-L and power efficiency curves of OLEDs comprising undoped and F <sub>4</sub> TCNQ doped (10 mol%) MTDATA or PMTDATA . . . . .	64
5.22. J-V-L and power efficiency curves of OLEDs comprising undoped and HATCN <sub>6</sub> doped (10 mol%) MTDATA or PMTDATA . . . . .	65
5.23. J-V-L and power efficiency curves of OLEDs comprising undoped and F <sub>4</sub> TCNQ doped (10 mol%) TPD or PTPD . . . . .	66
5.24. J-V-L and power efficiency curves of OLEDs comprising undoped and HATCN <sub>6</sub> doped (10 mol%) TPD or PTPD . . . . .	67
5.25. Photoelectron yield of undoped and doped (20 mol%) XMTDATA and XTPD before annealing, measured by PESA. . . . .	68
5.26. UV-vis-NIR absorption spectra of non-annealed undoped and doped (20 mol%) matrices XMTDATA and XTPD without annealing (20 mol%). . . . .	69
5.27. EPR spectra obtained from undoped and doped (20 mol%) XMTDATA and XTPD. . . . .	70

5.28. UV-vis-NIR spectra of undoped and doped (20 mol%) matrices XMTDATA before and after annealing. . . . .	71
5.29. UV-vis-NIR spectra of doped (20 mol%) and undoped XTPD before and after annealing. . . . .	72
5.30. Topography of undoped and doped XMTDATA films before and after crosslinking. . . . .	72
5.31. Topography of undoped and doped XTPD films before and after crosslinking.	73
5.32. PF-TUNA-AFM micrographs of the crystals in the HATCN <sub>6</sub> doped crosslinked polymer films. . . . .	74
5.33. Device architecture and energy levels of the employed materials. . . . .	75
5.34. J-V-L and power efficiency curves of OLEDs comprising annealed and non-annealed PMTDATA or XMTDATA as hole transport layers. . . . .	75
5.35. J-V-L and power efficiency curves of OLEDs comprising annealed and non-annealed PTPD or XTPD as hole transport layers. . . . .	76
5.36. Topography of undoped and doped (10 mol%) MTDATA and PMTDATA films after annealing. . . . .	77
5.37. Topography of undoped and doped (10 mol%) TPD and PTPD films after annealing. . . . .	78
5.38. PF-TUNA-AFM micrographs of HATCN <sub>6</sub> doped PMTDATA and PTPD after annealing. . . . .	78
5.39. Vis-NIR spectra of MTDATA:F <sub>4</sub> TCNQ solution in toluene (20 mol%) at different temperatures. . . . .	79
5.40. Vis-NIR spectra of MTDATA:F <sub>4</sub> TCNQ (20 mol%) films at different temperatures. . . . .	80
6.1. Chemical structures of all investigated electron transport materials and the dopant RhB in its active leuco form. . . . .	87
6.2. Normalized UV-vis absorbance spectra of neat TPBi/toluene and TPBi <sup>-</sup> /Na <sup>+</sup> /toluene solutions. . . . .	88
6.3. NMR spectra of neat TPBi and TPBi <sup>-</sup> :Na <sup>+</sup> solutions in toluene-D <sub>8</sub> . . . . .	89
6.4. EPR spectra of neat TPBi and TPBi:Na films. . . . .	90
6.5. Device architecture of solar cells. . . . .	91
6.6. ToF-SIMS measurements on a typical solar cell comprising a TPBi or a TPBi:Na layer. . . . .	92
6.7. Typical J-V curves of glass/ITO/EEL/PTB7-Th:PC <sub>61</sub> BM/MoO <sub>x</sub> /Ag solar cells under AM1.5 illumination. . . . .	93
6.8. EPR spectra of doped fullerene layers (20 mol%), measured without and under illumination. . . . .	98
6.9. UV-Vis absorption spectra of 20 nm thin-films of undoped and doped bis-PCBM (20 mol%) on glass before and after rinsing with EtOH. . . . .	100
6.10. Device architecture and typical J-V curves of glass/ITO/EEL/P3HT:ICBA/PEDOT:PSS/Ag solar cells under AM1.5 illumination. . . . .	101
A.1. UV-Vis absorption spectra of thin-films of undoped and doped bis-PCBM and ICBA (20 mol%) on glass before and after rinsing with EtOH . . . . .	121
A.2. Device architecture and typical J-V curves of glass/ITO/EEL/P3HT:ICBA/PEDOT:PSS/Ag solar cells under AM1.5 illumination. . . . .	122



# List of Tables

3.1. Key performance parameters of OLEDs. . . . .	23
5.1. Number of spins per volume and doping efficiency of the matrix-dopant (20 mol%) combinations as calculated from the EPR measurements. . . . .	50
5.2. Number of spins per volume and doping efficiencies of the matrix-dopant (20 mol%) combinations as calculated from EPR measurements. . . . .	52
5.3. Measured ionization potentials of all undoped and doped (20 mol%) matrix:dopant systems. . . . .	69
5.4. Number of spins per volume and doping efficiency of the non-annealed matrix-dopant (20 mol%) combinations as calculated from the EPR measurements. . . . .	70
6.1. Averaged key-performance data of organic solar cells comprising undoped and sodium doped EELs. . . . .	93
6.2. Number of spins per volume and doping efficiency of the matrix-dopant combinations (20 mol%) as calculated from the EPR measurements. . . . .	99
6.3. Averaged key-performance data of organic solar cells comprising undoped and RhB doped (20 mol%) EELs remeasured after 10 days. . . . .	101
A.1. Used optoelectronic materials. . . . .	117
A.2. Used chemicals. . . . .	120
A.3. Averaged key performance data of organic solar cells measured directly after fabrication. . . . .	123





# List of Publications and Conference Contributions

## Submitted publications arising from the present thesis

- *p-Doping of polystyrene polymers with attached functional side-groups from solution* T. Schneider, F. Limberg, K. Yao, A. Armin, N. Jürgensen, J. Czolk, P. Friederich, W. Wenzel J. Behrends, H. Krüger, A. Colsmann, submitted to *J. Chem. Mat. C* **2016**.
- *n-Doping of organic semiconductors for enhanced electron extraction from solution processed solar cells using alkali metals* T. Schneider, J. Czolk, D. Landerer, S. Gärtner, A. Pütz, M. Bruns, J. Behrends, A. Colsmann, submitted to *J. Chem. Mat. A* **2016**.
- *Enhanced electron extraction from solution processed organic solar cells, employing Rhodamine B doped fullerene layers* T. Schneider, S. Gärtner, B. Ebenhoch, J. Behrends, A. Colsmann, submitted to *Synth. Met.* **2016**.

## Publications in preparation arising from the present thesis

- *Solution processed p-doped hole injection layers for highly efficient organic light emitting diodes* T. Schneider, F. Limberg, K. Yao, A. Armin, N. Jürgensen, J. Czolk, P. Friederich, W. Wenzel, M. Bruns, J. Behrends, H. Krüger, A. Colsmann, in preparation.

## Other submitted publications

- *A fast and easy-to-incorporate thermally crosslinkable building block for solution processable OLED materials* F. R. P. Limberg, T. Schneider, S. Hoeffle, F. Reisbeck, S. Janietz, A. Colsmann, H. Krüger, submitted to *Adv. Energy Mater.* **2016**.

## Additional publications

- *$\pi$ -Conjugated Polymer-Fullerene Covalent Hybrids via Ambient Conditions Diels-Alder Ligation* B. Yameen, T. Puerckhauer, J. Ludwig, I. Ahmed, O. Altintas, L. Fruk, A. Colsmann, C. Barner-Kowollik, *Small* **2014**, *10*, 3091-3098.
- *Probing the Diameter Limit of Single Walled Carbon Nanotubes in SWCNT:Fullerene Solar Cells* M. Pfohl, K. Glaser, A. Graf, A. Mertens, D. D. Tune, T. Puerckhauer, A. Alam, L. Wei, Y. Chen, J. Zaumseil, A. Colsmann, R. Krupke, B. S. Flavel, *Adv. Energy Mat.* **2016**, accepted.

## Conference Contributions

- *Electrical and spectroscopic characterisation of molecular p-doped side-chain polymers with small molecule moieties processed from solution* (Oral presentation) T. Pürckhauer, N. Jürgensen, F. Limberg, H. Krüger, J. Behrends, A. Colsmann, **8th International Symposium on Flexible Organic Electronics (ISFOE15)**, July 6-9, **2015**, Thessaloniki, **Greece**.
- *Electrical and spectroscopic characterisation of molecular p-doped side-chain polymers with small molecule moieties processed from solution* (Poster presentation) T. Pürckhauer, N. Jürgensen, F. Limberg, H. Krüger, J. Behrends, A. Colsmann, **7th International Conference on Molecular Electronics (ElecMol14)**, August 24-29, **2014**, Strasbourg, **France**.
- *p-Doping of Hole Transport Layers for Organic Electronic Devices from Solution* (Poster presentation) T. Pürckhauer, T. H. Do, J. Behrends, U. Lemmer, A. Colsmann, **SPP 1355 Spring School**, August 24-29, **2013**, Dresden, **Germany**.

# Acknowledgements

Als erstes möchte ich mich bei meinem Betreuer Dr. Alexander Colsmann bedanken, der den Schritt gewagt hat, mich als erste Chemikerin in seine Arbeitskreis auf zu nehmen und mir somit diese Arbeit ermöglicht hat. Besonders bedanken möchte ich mich für seine Unterstützung sowohl fachlich, bei vielen Gesprächen und Diskussionen, als auch organisatorisch, z.B. bei der Suche nach einem Doktorvater. Vielen Dank für die Unterstützung.

Als nächstes danke ich Prof. Dr. Christopher Barner-Kowollik dafür, dass er die Stelle meines Doktorvaters und den damit verbundenen Aufwand übernommen hat. Die Zusammenarbeit verlief immer problemlos und durch die Vermittlung von Kontakten in seiner Arbeitsgruppe konnten auch einige Projekte realisiert werden, die ansonsten nicht möglich gewesen wären. Außerdem danke ich ihm für die Bereitstellung eines Arbeitsplatzes in der Chemie, an dem ich mit Unterstützung von Dr. Eva Blasco Polymere herstellen konnte.

Prof. Dr. Uli Lemmer möchte ich danken, dass er spontan des Korreferat übernommen hat.

Da diese Arbeit ohne die Hilfe vieler anderer nicht möglich gewesen wäre, möchte ich mich an dieser Stelle bei all denen bedanken, die zu dem Gelingen dieser Arbeit beigetragen haben.

Der Arbeitsgruppe von Dr. Hartmut Krüger vom Fraunhofer IAP, allen voran Felix Limberg möchte ich für die Synthese der verwendeten Polymere danken. Prof. Dr. Jan Behrends möchte ich für die Möglichkeit zur Untersuchung meiner Proben mittels EPR-Messungen und für viele Diskussionen danken. Kelvin Yao danke ich für die Unterstützung bei den EPR-Messungen. Dr. Michael Bruns danke ich für die ToF-SIMS- und Austrittsarbeitsmessungen, die mir einige Paper vervollständigt haben. Ich danke PhD Ardalan Armin für die Bereitstellung seines Wissens über Ladungstransport und für seine Hilfe beim Aufbau eines CELIV-Messplatzes.

Auch innerhalb der Arbeitsgruppe durfte ich viel Unterstützung erfahren.

Daniel Bahro danke ich für die Impedanzmessungen und für seine Geduld mit der er all meine Fragen beantwortet hat. Stefan Gärtner danke ich für seine Hilfe bei der Nanopartikelsynthese und für die vielen verschiedenen AFM-Messungen. Danke natürlich auch dafür, dass er den Chemiker-Anteil in der Arbeitsgruppe verstärkt hat. Joshua Fragoso und Mahsa Bagheri danke ich für das Korrekturlesen meiner Arbeit und für die vielen Kommas. Jetzt beherrsche ich endlich die Kommaregeln der englischen Sprache. Allen anderen Kollegen, Stefan Höfle, Jens Czolk, Adrian Mertens, Manuel Koppitz, Min Zhang, Christian Sprau, Konstantin Glaser, Dominik Landerer und Holger Röhm danke ich dafür, dass sie meine Promotion zu so einer tollen Zeit gemacht haben, sowohl während als auch außerhalb der Arbeitszeit. Ein besseres Team kann ich mir nicht vorstellen.

Für die Unterstützung bei vielen organisatorischen, technischen und bürokratischen Dingen, die ich ansonsten nicht so reibungslos in den Griff bekommen hätte, möchte ich mich bei den Sekretärinnen des LTI, Astid Henne und Claudia Holeisen, sowie bei Dr. Anja Goldmann, Christian Kayser, Vincent Schüler, Felix Geislhöringer, Mario Sütsch und dem Team der Werkstatt des LTI bedanken.

Großer Dank gebührt natürlich auch meinen Studenten, allen voran Nils Jürgensen, Benjamin Peter und Dominik Theobald, die mich mit ihrer Zuarbeit sehr unterstützt haben.

Der Karlsruhe School of Optics and Photonics (KSOP), allen voran Denica Angelova-Jackstadt und Stefanie Peer, danke ich für die finanzielle Unterstützung und für viele interessante Module, die mir interdisziplinäres und interkulturelles Arbeiten auch außerhalb meiner Arbeitsgruppe ermöglicht haben. Desweiteren danke ich auch dem Bundesministerium für Bildung und Forschung (BMBF) für die finanzielle Unterstützung durch das Projekt TAURUS, das diese Doktorarbeit erst ermöglicht hat.

Besonderer Dank gilt natürlich meiner Familie, allen voran meiner Mama, die mich tapfer ertragen haben, wenn mal wieder etwas nicht funktioniert hat. Meinem Mann danke ich für das Korrekturlesen meiner Arbeit und die große Unterstützung, während der ganzen Zeit.

# Declaration

Ich erkläre hiermit, dass ich die vorliegende Arbeit im Rahmen der Betreuung durch Prof. Dr. Christopher Barner-Kowollik selbstständig verfasst und keine anderen als die angegebenen Quellen und Hilfsmittel verwendet habe. Wörtlich oder inhaltlich übernommenen Stellen sind als solche kenntlich gemacht und die Satzung des Karlsruher Instituts für Technologie (KIT) zur Sicherung guter wissenschaftlicher Praxis wurde beachtet. Des Weiteren erkläre ich, dass ich mich derzeit in keinem weiteren laufenden Promotionsverfahren befinde und auch keine vorausgegangenen Promotionsversuche unternommen habe.

---

Karlsruhe, 22.07.2016